

ISOLATOR-FREE DFB LASER
FOR ANALOG CATV APPLICATIONS

By
Ayman Mokhtar, B.Sc., M.Sc.,

A Thesis Submitted to
The Faculty of Graduate Studies and Research
in partial fulfillment of the requirements for the degree of

Doctor of Philosophy

Ottawa-Carleton Institute for Electrical and Computer Engineering
Faculty of Engineering
Department of Systems and Computer Engineering
Carleton University
Ottawa, Ontario, Canada

January, 2007

© 2007 Ayman Mokhtar



Library and
Archives Canada

Bibliothèque et
Archives Canada

Published Heritage
Branch

Direction du
Patrimoine de l'édition

395 Wellington Street
Ottawa ON K1A 0N4
Canada

395, rue Wellington
Ottawa ON K1A 0N4
Canada

Your file *Votre référence*
ISBN: 978-0-494-23295-8
Our file *Notre référence*
ISBN: 978-0-494-23295-8

NOTICE:

The author has granted a non-exclusive license allowing Library and Archives Canada to reproduce, publish, archive, preserve, conserve, communicate to the public by telecommunication or on the Internet, loan, distribute and sell theses worldwide, for commercial or non-commercial purposes, in microform, paper, electronic and/or any other formats.

The author retains copyright ownership and moral rights in this thesis. Neither the thesis nor substantial extracts from it may be printed or otherwise reproduced without the author's permission.

AVIS:

L'auteur a accordé une licence non exclusive permettant à la Bibliothèque et Archives Canada de reproduire, publier, archiver, sauvegarder, conserver, transmettre au public par télécommunication ou par l'Internet, prêter, distribuer et vendre des thèses partout dans le monde, à des fins commerciales ou autres, sur support microforme, papier, électronique et/ou autres formats.

L'auteur conserve la propriété du droit d'auteur et des droits moraux qui protègent cette thèse. Ni la thèse ni des extraits substantiels de celle-ci ne doivent être imprimés ou autrement reproduits sans son autorisation.

In compliance with the Canadian Privacy Act some supporting forms may have been removed from this thesis.

Conformément à la loi canadienne sur la protection de la vie privée, quelques formulaires secondaires ont été enlevés de cette thèse.

While these forms may be included in the document page count, their removal does not represent any loss of content from the thesis.

Bien que ces formulaires aient inclus dans la pagination, il n'y aura aucun contenu manquant.


Canada

Abstract

Fiber-pigtailed Distributed Feedback (DFB) laser diode modules often employ isolators to reduce the optical feedback induced intensity noise and distortion, and to meet the requirements imposed on the DFB lasers in analog optical transmission systems such as Cable Television (CATV). For some situations however, isolators could be avoided to reduce cost and simplify laser module manufacture while maintaining the desired DFB laser's performance.

In this thesis, Fabry Perot (FP) and DFB laser diode rate equations were augmented to include the effect of optical back-reflections. The proposed laser model was implemented in software and used as the basis for linearity and noise simulations in which the effect of the reflected optical power on the laser diode performance was studied. The model's results were verified experimentally using an tunable induced back-reflection setup.

Results suggest that it is beneficial to operate unisolated DFB laser diodes in feedback Regime V. This was achieved by attaching appropriate FBG to DFB laser. Two telecommunications wavelengths, 1310 nm and 1550 nm, were used to examine the performance of a DFB laser coupled to an Fiber Bragg Grating (FBG). A stable spectrum was showed and low Relative Intensity Noise (RIN) comparable to that of the isolated DFB laser was achieved for both wavelengths.

A pre-distorter model including optical back-reflection effects was derived, implemented in software, and cascaded to the laser model to compensate for the laser nonlinearity. Simulation results showed that at 0.10 modulation index, average improvements of 45 dB in second order harmonic distortion, 55 dB in third order harmonic distortion, and 40 dB in different intermodulation distortions can be achieved using the proposed pre-distortion technique. Furthermore, at a modulation index of 0.04, the predistorter was found to

reduce the second order harmonic distortion and two-tone third order intermodulation distortion levels to less than -75 dB and -100 dB respectively. This hence renders the laser suitable for CATV applications.

Our proposed pre-distorter constitutes a contribution to the state-of-the-art as it enhances the precision of currently used models by adding the effect of the optical feedback.

Acknowledgements

I would like to express my deep appreciation and gratitude to Professor Samy Mahmoud, my supervisor and President of Carleton University, for his guidance and encouragement. I am greatly indebted to Professor Mahmoud for his dedication, talent, and generosity.

I would also like to express my gratitude to Prof Leonard MacEachern, co-supervisor of this thesis, for his excellent advice and guidance during my doctoral research. His promptness and continual advice were highly appreciated.

I would like to express my thanks to Dr. Samy Ghoniemy for his assistance and support. I am grateful to the Department of Systems and Computer Engineering for providing a suitable research environment, and for their kind support. I would also like to recognize Prof Jacques Albert and all members of Carleton Laboratory for Induced Photonic Structures for their kind assistance. I would like to express my appreciation to Mr. Nagui Mikhail for his highly qualified assistance. I deeply thank my best friend in Ottawa, Mohamed Abou El Saoud, for his efforts.

I am grateful to my beloved country Egypt; this research would have not been possible without the financial support of the Egyptian Ministry of Defense.

I would also like to express my deep thanks to my dearest mother, her prayers and encouragement facilitate my life. I deeply thank my brothers and sisters, especially my eldest brother Wael, for all the support and encouragement.

I am indeed indebted to my dearest wife for all the sacrifices she made in order to facilitate a suitable environment for my doctoral work. I thank my daughters, MenatAllah, Yasmine, and Nour; completion of my doctorate would not have been possible without their love.

Last but never the least, thanks to my great father who passed away before I could realize this dream.

Table of Contents

Abstract	iv
Acknowledgements	vi
Table of Contents	vii
List of Tables	xii
List of Figures	xiii
1 Introduction	1
1.1 Introduction	1
1.2 Thesis Motivation	2
1.3 Objectives	3
1.4 Contributions	3
1.5 Organization	4
2 Background and Motivation	5
2.1 Laser Principles and Rate Equations	5
2.1.1 Laser Principles	5
2.1.2 Laser Diode Rate Equations Concept	6
2.1.3 FP vs DFB Laser Diode Rate Equations	7
2.2 Conventional Laser Diode Rate Equations	8
2.3 Modified Laser Diode Rate Equations	8
2.4 Feedback Regimes	10
2.5 Conventional Laser Diode Rate Equations Including Optical Feedback effect	14
2.6 Analysis of Feedback Phenomenon	16
2.7 Changes to Laser Performance due to External Cavity	22
2.7.1 Emission Frequency Shift due to Feedback	22
2.7.2 Single External Cavity Mode Condition	23
2.7.3 Spectral Linewidth Change due to Optical Feedback	23

2.7.4	Phase and Frequency Noise of Laser with Optical Back-reflections	23
2.7.5	Laser Intensity Noise due to Optical Feedback	24
2.7.6	Dynamic Properties of Laser with External Cavity	25
2.8	CATV Systems	25
2.8.1	CATV Transmitter Performance	28
	CATV Transmitter Noise	28
	CATV Transmitter Linearity	29
	Typical CATV Transmitter Performance	30
2.8.2	Limiting Factors to CATV System Performance	31
2.9	Motivation	32
3	Proposed Model and Simulation Results	34
3.1	Introduction	34
3.2	The Proposed Rate Equations	34
3.2.1	Derivation of the Feedback Terms	35
3.2.2	Feedback Term Normalization and the Proposed Rate Equations	38
3.3	Model Implementation	39
3.3.1	Symbolically Defined Laser Diode Models Including Feedback Term	39
3.3.2	Parameters Extraction	41
3.4	Simulation Results	41
3.4.1	Simulation of Laser Performance changes due to Feedback	41
	Possible emission frequencies	43
	Maximum oscillation frequency shift due to feedback	43
	Spectral linewidth change due to feedback	45
3.4.2	DC Simulation	47
3.4.3	DFB Laser Diode Frequency Response	47
3.4.4	DFB Laser Diode Distortion	50
3.5	Laser Model Including Feedback and Noise terms	55
3.5.1	Relative Intensity Noise Calculation	58
3.5.2	Laser output	58
3.5.3	Modulation Frequency Response Simulation	58
3.5.4	RIN Simulation	58
	RIN versus bias current for fixed unintended optical back-reflection	60
	RIN versus external reflectivity	60
3.6	Summary	63
4	Experimental Work and Model Verification	64
4.1	Introduction	64
4.2	DC Measurements	64
4.2.1	Threshold Current Measurements Setup	64
4.2.2	Threshold Current Results and Model Verification	65

4.2.3	DFB Laser Diode Spectra Measurement Setup and Results	66
4.3	Noise and Linearity Measurements	70
4.3.1	RIN Measurements Experimental Setup	72
4.3.2	RIN Measurement Results and Model Verification	72
	RIN versus bias current	72
	RIN versus external reflectivity	76
4.3.3	Modulation Frequency Response Measurements	82
4.3.4	Distortion Measurements Setup and Results	83
4.4	Summary	88
5	FBG Design and Implementation	89
5.1	Introduction	89
5.2	FBG Introduction and Basic Calculations	89
5.2.1	FBG Principles	89
5.2.2	FBG Parameter Calculations	91
	Laser output parameters	91
	FBG parameters	91
5.3	OptiGrating Design Software	91
5.4	FBG Implementation	93
5.4.1	FBG Implementation Procedures	93
	Optical fiber preparation	93
	Phase mask	93
	Interferometric (Holographic) technique	94
	Post processing of Bragg grating	94
5.4.2	The Implemented FBG Characteristics	94
5.5	Summary	98
6	DFB Laser Diode with External FBG	99
6.1	Spectrum Stability	100
6.1.1	1550 nm wavelength range	100
6.1.2	1310 nm wavelength range	102
6.2	Relative Intensity Noise Measurements	103
6.2.1	1550 nm wavelength range	103
6.2.2	1310 nm wavelength range	107
6.3	Distortion Measurements	108
6.3.1	1550 nm wavelength range	108
6.3.2	1310 nm wavelength range	109
6.4	Summary	113

7	Inverse Laser Model Including Feedback Derivation and Modeling	114
7.1	Introduction	114
7.2	Inverse Laser Model Including Feedback Derivation	115
7.2.1	Volterra Series	120
7.2.2	Extraction of Volterra Transfer Functions	120
	Harmonic-input method	120
	Direct expansion method	121
7.3	Inverse Laser Model Including Feedback Implementation	124
7.4	Typical CATV system	132
7.5	Summary	137
8	Conclusions and Future Work	138
8.1	Conclusions	138
8.2	Future Work	140
	Appendix A Measurements Equipments and Results	143
A.1	Different Equipments Used in The Measurements	143
A.1.1	DFB laser diodes, laser mount and laser controller	143
A.1.2	Fiber optic beam splitter	143
A.1.3	Fiber optic reflector	144
A.1.4	Variable attenuator	144
A.1.5	Optical multimeter	145
A.1.6	Optical Spectrum Analyzer	145
A.1.7	Polarization controller	147
A.2	RIN Measurements Results	147
	Appendices	143
	Appendix B DFB Laser Diode with External FBG	151
B.1	FBG Design Steps	151
B.1.1	Step 1	151
B.1.2	Step 2	152
B.1.3	Step 3	152
B.1.4	Step 4	154
B.1.5	Step 5	154
B.1.6	Step 6	154
B.2	FBG Transmission and Reflection Characteristics	156
B.3	Spectrum Stability of DFB Laser with FBG	163
B.4	RIN Measurements of DFB Laser with FBG	166
B.5	Distortion Measurements of DFB Laser with FBG	168

List of Tables

2.1	Typical CATV transmitter specifications	31
3.1	Laser parameters	42
4.1	Measured average RIN at 1 GHz frequency offset for different bias levels .	76
4.2	Measured average RIN at 1 GHz frequency offset for 15 mA bias current and different feedback levels	81
6.1	Various components used in the measurements	99
6.2	Measured average RIN for various DFB5 configurations	106
6.3	Measured distortion for various DFB5 configurations	111
7.1	Various distortion components improvement	133

List of Figures

2.1	Laser principle operation	6
2.2	Cavity loss and related effective reflectivity for DFB lasers	9
2.3	FeedBack regimes	12
2.4	DFB laser diode spectra under different feedback levels	13
2.5	Laser cavity with external feedback	17
2.6	Round trip phase change	21
2.7	Calculated frequency noise spectrum	24
2.8	Calculated RIN for different external cavity lengths	26
2.9	Measured RIN for different feedback levels	27
2.10	Basic structure of a Hybrid Fiber/Coax CATV system	28
3.1	4-port SDD laser model with external feedback	41
3.2	Round trip phase change versus the optical frequency	44
3.3	Maximum oscillation frequency shift versus laser cavity length	44
3.4	Maximum oscillation frequency shift versus laser exit facet reflectivity	45
3.5	Maximum oscillation frequency shift versus external reflectivity	46
3.6	Spectral linewidth with feedback	46
3.7	Swept-parameter DC simulation setup	48
3.8	Simulation results for threshold current change due to feedback	49
3.9	Simulated threshold current levels at different external reflectivity	49
3.10	Harmonic balance simulation setup for the laser model with external feedback	50
3.11	Modulation frequency response for the the laser diode with and without external feedback	51

3.12	Distortion simulation setup for laser diode with and without feedback . . .	52
3.13	Simulated second harmonic distortion vs. external reflectivity for different bias current levels	53
3.14	Simulated third harmonic distortion vs. external reflectivity for different bias current levels	54
3.15	Simulated second harmonic distortion vs. bias current for different external reflectivity levels	54
3.16	Simulated third harmonic distortion vs. bias current for different external reflectivity levels	55
3.17	ADS laser model including feedback terms and noise operators	57
3.18	Time domain laser model's output	59
3.19	Simulated modulation frequency response	60
3.20	Simulated RIN	61
3.21	Simulated RIN versus bias current	61
3.22	Simulated RIN versus external reflectivity	62
4.1	DC measurements experiment setup block diagram	65
4.2	Experiment setup schematic diagram for DC measurements	66
4.3	The P-I curve for 1550 nm DFB laser diode under -14 dB feedback ratio	67
4.4	Threshold current change for 1550 nm DFB laser diode under -14 dB feedback ratio	67
4.5	Threshold current change for 1310 nm DFB laser diode under -14 dB feedback ratio	68
4.6	Measured and simulated threshold current change due to optical back-reflection	68
4.7	DFB laser diode spectra experiment setup block diagram	69
4.8	1310 nm DFB laser diode spectra under different feedback powers	70
4.9	Agilent lightwave signal analyzer	71
4.10	Relative intensity noise measurement setup	73
4.11	Measured relative intensity noise at 25 mA bias current	73
4.12	Measured relative intensity noise at 30 mA bias current	74
4.13	Measured relative intensity noise at 35 mA bias current	74

4.14	Measured relative intensity noise at 40 mA bias current	75
4.15	Measured relative intensity noise at 60 mA bias current	75
4.16	Measured and simulated relative intensity noise	77
4.17	measured relative intensity noise for bias current level of 15 mA and external reflectivity of -45 dB	77
4.18	Measured relative intensity noise for bias current level of 15 mA and external reflectivity of -40 dB	78
4.19	Measured relative intensity noise for bias current level of 15 mA and external reflectivity of -27 dB	78
4.20	measured relative intensity noise for bias current level of 15 mA and external reflectivity of -20 dB	79
4.21	Measured relative intensity noise for bias current level of 15 mA and external reflectivity of -10 dB	79
4.22	Simulated and measured RIN for different feedback powers	81
4.23	Modulation frequency response measurement setup	83
4.24	DFB relaxation oscillation frequency with -45 dB feedback level	84
4.25	DFB relaxation oscillation frequency with -40 dB feedback level	84
4.26	DFB relaxation oscillation frequency with -15 dB feedback level	85
4.27	DFB relaxation oscillation frequency with -10 dB feedback level	85
4.28	Distortion measurement setup	86
4.29	Measured second order harmonic distortion of DFB laser at different feedback levels	87
4.30	Measured third order harmonic distortion of DFB laser at different feedback levels	88
5.1	FBG structure	90
5.2	DFB laser diode spectrum at different bias current levels	92
5.3	Phase mask	93
5.4	Interferometric technique	94
5.5	FBG setup	95
5.6	Writing FBG	95

5.7	The phase mask used in FBG implementation	96
5.8	FBG1 reflection and transmission characteristics	97
6.1	Spectrum of DFB5 attached to FBG1	101
6.2	Spectrum of DFB5 attached to FBG2	101
6.3	Spectrum of DFB2 attached to FBG12	102
6.4	Spectrum of DFB2 attached to FBG12	103
6.5	Measured average RIN of DFB5	104
6.6	Measured average RIN of DFB5 attached to a 30 dB optical isolator	104
6.7	Measured average RIN of DFB5 attached to FBG10	105
6.8	Measured RIN of DFB5 attached to FBG11	106
6.9	Measured RIN of DFB2 laser diode attached to FBG12	107
6.10	Measured RIN of DFB1	108
6.11	Measured second order harmonic distortion of DFB5 attached to FBG1 . . .	109
6.12	Measured third order harmonic distortion of DFB5 attached to FBG1 . . .	110
6.13	Measured second order harmonic distortion of DFB5 attached to FBG2 . . .	110
6.14	Measured third order harmonic distortion of DFB5 attached to FBG2 . . .	111
6.15	Measured second order harmonic distortion of DFB2 attached to FBG12 . .	112
6.16	Measured third order harmonic distortion of DFB2 attached to FBG12 . . .	113
7.1	Block diagram of the laser inverse model	123
7.2	ADS implementation of the laser inverse model	125
7.3	ADS setup of the laser inverse model cascaded to the laser model	126
7.4	Simulated second order harmonic with and without PD	127
7.5	Simulated third order harmonic with and without PD	127
7.6	Simulated second intermodulation distortion with and without PD	128
7.7	Simulated third intermodulation distortion ($2f_1 + f_2$) with and without PD	129
7.8	Simulated third intermodulation distortion ($2f_1 - f_2$) with and without PD	130
7.9	Simulated third intermodulation distortion ($2f_2 + f_1$) with and without PD	131
7.10	Simulated third intermodulation distortion ($2f_2 - f_1$) with and without PD	132
7.11	Simulated second order harmonic with and without PD for 0.04 modulation	
	index	134

7.12 Simulated third order harmonic with and without PD for 0.04 modulation index	135
7.13 Simulated third intermodulation distortion ($2f_1 + f_2$) with and without PD	135
7.14 Simulated third intermodulation distortion ($2f_1 - f_2$) with and without PD	136
7.15 Simulated third intermodulation distortion ($2f_2 + f_1$) with and without PD	136
7.16 Simulated third intermodulation distortion ($2f_2 - f_1$) with and without PD	137
8.1 Block diagram of the suggested adaptive pre-distorter	141
A.1 OZ Optics fiber optic beam splitter	144
A.2 OZ Optics fiber optic reflector	145
A.3 OZ Optics variable attenuator	145
A.4 Optical multimeter and laser controller	146
A.5 Agilent 86140B optical spectrum analyzer	146
A.6 OZ Optics polarization controller	147
A.7 Measured average relative intensity noise for bias current level of 15 mA and external reflectivity of -42 dB	148
A.8 Measured average relative intensity noise for bias current level of 15 mA and external reflectivity of -36 dB	148
A.9 Measured average relative intensity noise for bias current level of 15 mA and external reflectivity of -33 dB	149
A.10 Measured average relative intensity noise for bias current level of 15 mA and external reflectivity of -29 dB	149
A.11 Measured average relative intensity noise for bias current level of 15 mA and external reflectivity of -24 dB	150
A.12 Measured average relative intensity noise for bias current level of 15 mA and external reflectivity of -15 dB	150
B.1 FBG design step 1	151
B.2 FBG design step 2	152
B.3 FBG design step 3	153
B.4 FBG design step 4	154

B.5	FBG design step 5	155
B.6	FBG design step 6	155
B.7	FBG2 reflection and transmission characteristics	157
B.8	FBG4 reflection and transmission characteristics	158
B.9	FBG7 reflection and transmission characteristics	159
B.10	FBG10 reflection and transmission characteristics	160
B.11	FBG11 reflection and transmission characteristics	161
B.12	FBG12 transmission spectrum	162
B.13	Spectrum of DFB5 attached to FBG4	163
B.14	Spectrum of DFB5 attached to FBG7	164
B.15	Spectrum of DFB5 attached to FBG7	164
B.16	Spectrum of DFB5 attached to FBG10	165
B.17	Spectrum of DFB5 attached to FBG11 operating at bias level of 15 mA . .	165
B.18	Spectrum of DFB5 attached to FBG11 operating at bias level of 20 mA . .	166
B.19	Measured RIN of DFB5 attached to FBG10	167
B.20	Measured RIN of DFB5 attached to FBG2	167
B.21	Measured second order harmonic distortion of DFB5 attached to FBG4 . .	168
B.22	Measured third order harmonic distortion of DFB5 attached to FBG4 . . .	169
B.23	Measured second order harmonic distortion of DFB5 attached to FBG7 . .	169
B.24	Measured third order harmonic distortion of DFB5 attached to FBG7 . . .	170
B.25	Measured second order harmonic distortion of DFB5 attached to FBG10 .	170
B.26	Measured third order harmonic distortion of DFB5 attached to FBG10 . .	171
B.27	Measured second order harmonic distortion of DFB5 attached to FBG11 .	171
B.28	Measured third order harmonic distortion of DFB5 attached to FBG11 . .	172

Chapter 1

Introduction

1.1 Introduction

Fiber optic cables have many advantages over copper cables in terms of data transmission. Some of these advantages include: high bandwidth, light weight, immunity from electromagnetic radiation, and low cost [1]. Fiber optics can be used in analog optical transmission applications such as Cable Television (CATV) systems to distribute CATV signals over large geographic areas with high quality. Semiconductor laser nonlinearity and intensity noise are of concern in CATV systems. In order to provide high quality video to subscribers, CATV systems require a Carrier to Noise Ratio (CNR) of 50 dB, Composite Second Order distortion (CSO), and Composite Triple Beat (CTB) of -60 dBc [2–4]. CSO and CTB are mainly related to the different harmonic and intermodulation distortion mechanisms in the laser diode; CNR is limited by the laser's Relative Intensity Noise (RIN). One major factor increasing the RIN and distortion is optical back-reflections which can modify the static and dynamic characteristics of the laser. These reflections originate from the laser facet, laser/fiber interface, and fiber connectors.

There can be benefits to operating laser diodes with optical feedback: (i) selection of a distinct longitudinal mode of a Fabry Perot (FP) laser [5,6]; (ii) tuning of Distributed Feedback (DFB) laser emission frequency [7]; (iii) considerable linewidth narrowing [8,9]. However, optical feedback is typically expected to be detrimental to laser diode performance. For example, at some optical feedback levels laser spectral linewidth has been found to broaden by several tens of gigahertz (20 GHz is equivalent to 0.16 nm at $\lambda = 1550$ nm) [10]; an increase in RIN has been also observed. This large variety of both positive and negative

effects suggests that optical feedback phenomena should be studied in detail.

Laser diode rate equations describe the interaction between the injected electrons and the generated phonons in the laser cavity. Rate equations typically neglect optical back-reflections for simplicity, thereby making them ill-suited for analysis of laser diode performance with consideration of optical back-reflection effects. This work addresses the need for a comprehensive laser model with the ability to evaluate the performance changes due to optical back-reflections.

The phenomena arising in laser diodes subject to optical back reflection can be classified based on the feedback magnitude in five regimes, identified as Regimes I, II, III, IV, and V (ordered from least to greatest magnitude of feedback) [11]. In Regime I, the feedback level is weak and the narrowing or broadening of the laser spectral linewidth depends on the phase of the feedback. In Regime II, rapid mode hopping causes a splitting of the laser spectrum. The laser spectrum returns to a single narrow line again in Regime III. Regime IV is reached if further increase of the feedback strength is applied, the linewidth is dramatically broadened as a result. This regime is also known as coherence collapse regime. When the feedback level is increased further, the laser returns to narrow-linewidth single-mode operation and operate in Regime V [12].

1.2 Thesis Motivation

A need for a comprehensive laser model which has the ability to predict the laser diode performance due to the reflected waves (RIN, distortion, etc.) is vital. The model should also suggest the operating point based on the laser diode parameters so that transition to the coherence collapse regime can be avoided. The laser spectrum is narrowed for all feedback phases only in Regime V; the laser exhibits low RIN level and becomes insensitive to further reflections. In general this regime cannot be achieved for uncoated lasers without intentional external reflections. The challenge is to force the laser to operate in Regime V. FBG provides a good solution: including a suitable external FBG in the fiber pigtail can drive the laser diode to operate in Regime V and make it suitable for CATV applications. CATV systems require low distortion levels for the laser. This necessitates an effective linearization technique to compensate for laser nonlinearity. A suitable laser

model that contains major causes of laser distortions can be a good building block for such distortion compensation technique. Further elaboration is found in the Motivation section of Chapter 2.

1.3 Objectives

The main objective of this thesis is to enhance the performance of the DFB laser diode for analog CATV applications and to avoid the costly isolator, thereby simplifying the laser module fabrication process while still maintaining the required laser performance. This can be achieved in the following key steps:

- Review and analyze the available semiconductor laser rate equations that include the optical back-reflections terms.
- Advance the state of the art in the area of modeling signal transmission over optical fiber links by introducing the proposed model based on the laser diode rate equations that contain the optical back-reflections terms.
- Evaluate the laser performance under optical back-reflections using the proposed models.
- Analyze the different feedback regimes.
- Avoid using the isolator needed for DFB laser diode.
- Develop a suitable technique to enhance the DFB laser diode performance in the existence of the reflected power by using an external FBG.
- Design and implement the proposed FBG.
- Evaluate laser diode performance with and without the FBG.
- Develop a suitable technique to improve the laser linearity.

1.4 Contributions

The main contributions in this thesis are summarized below:

- Enhancing the mathematical modeling of DFB laser diodes by including the feedback terms in the rate equations.
- Using Agilent ADS software to implement the laser model with feedback effect.

- Prediction of the the coherence collapse regime and other feedback regimes of the DFB laser diode.
- Prediction of the DFB laser diode DC behavior, distortion, RIN, and modulation response with different back-reflection powers.
- Model verification.
- Identification of the the DFB laser diode spectrum under different feedback powers through experimentation.
- Design and implementation of the FBG needed to force the DFB laser diode to operate in Regime V.
- Performance analysis for the DFB laser diode with the FBG compared to the isolated DFB laser diode.
- Derivation and modeling of the inverse laser model including feedback to compensate for the laser diode distortion.

1.5 Organization

Chapter 1 introduced this work. Background and motivation to this work are presented in Chapter 2. Chapter 3 presents the model implementation and simulation results. Chapter 4 presents the experimental work and model verification. FBG design and implementation are presented in Chapter 5. In Chapter 6, the performance evaluation of DFB laser diode with an external FBG is presented and compared to that of the isolated DFB laser diode. The derivation, software implementation, and testing of the inverse laser model including optical back-reflections effect is demonstrated in Chapter 7. Finally, Chapter 8 summarizes the results obtained from this work, gives the overall conclusions, and poses recommendations for future work.

Chapter 2

Background and Motivation

This chapter provides an explanation for the laser diode principles and the rate equation concept. The conventional laser diode rate equations and the modified gain laser diode rate equations are reviewed. The feedback phenomenon and its different regimes are analyzed, previous work that investigated feedback effects is also surveyed. Changes to laser diode performance due to optical back-reflections are discussed. Challenges to CATV systems performance are presented at the end of this chapter.

2.1 Laser Principles and Rate Equations

2.1.1 Laser Principles

LASER is an acronym for **L**ight **A**mplification by the **S**timulated **E**mission of **R**adiation. Ideal laser light is of a single wavelength, formed in parallel beams and it is coherent, that is, in a single phase. Laser operation involves three key light-matter interaction processes [13]:

- **Photon absorption:** when a photon of energy $h\nu$ impinges on the system, an electron in state E_1 can absorb the photon energy and be excited to state E_2 as shown in Figure 2.1.a.
- **Spontaneous emission:** the electron at state E_2 will shortly return to the ground state without external stimulation as shown in Figure 2.1.b.
- **Stimulated emission:** if a photon of energy $h\nu$ impinges on the system while the electron is still in its excited state, the electron is immediately stimulated to drop to the ground state and give off a photon of energy $h\nu$ in phase with the incident

photon as shown in Figure 2.1.c.

As shown in Figure 2.1 there are two energy states, ground state E_1 and the excited-state energy E_2 . The transition between these two states involves the absorption or emission of photon of energy $E_2 - E_1$. In thermal equilibrium the density of excited electrons is very small. Most photons incident on the system will therefore be absorbed, so that stimulated emission is essentially negligible. Stimulated emission will exceed absorption only if the population of the excited states is greater than that of the ground state. This condition is known as *population inversion*. It is achieved by various pumping techniques. In semiconductor lasers, this is accomplished by the injection of electrons into the material at the device contacts to fill the lower energy states of the conduction band.

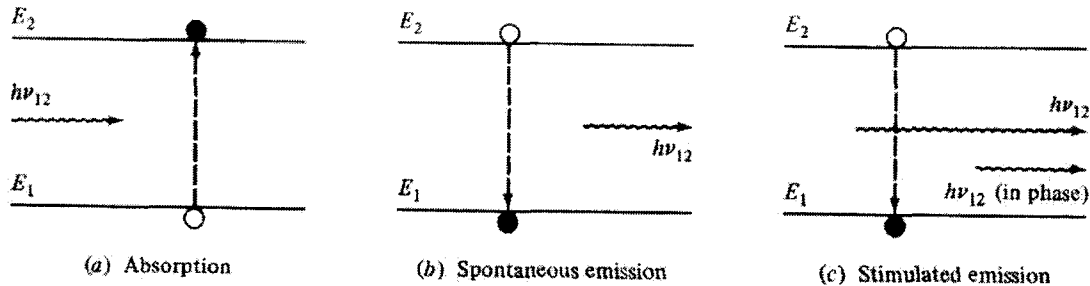


Figure 2.1: The three key processes in laser operation: absorption, spontaneous emission, and stimulated emission process, reproduced from [13].

2.1.2 Laser Diode Rate Equations Concept

The semiconductor laser diode rate equations describe the interaction between the injected carriers and the generated photons in the laser diode active region. The total carrier population is determined by carrier injection, spontaneous recombination, and stimulated emission. For a PN junction with carrier-confinement region of depth d , the rate equations are given by: $\frac{dP}{dt} = \text{Stimulated emission} + \text{Spontaneous emission} + \text{Photon loss}$; which governs the number of photons P , and $\frac{dC}{dt} = \text{Injection} + \text{Stimulated emission} + \text{Spontaneous emission}$; which governs the number of electrons C . Under steady state condition $\frac{dP}{dt} = 0$, $\frac{dC}{dt} = 0$, the steady state photon density P_s is given by: $P_s = \text{Number of photons resulting}$

from stimulated emission + Spontaneously generated photons [13].

2.1.3 FP vs DFB Laser Diode Rate Equations

A FP laser diode uses two end mirrors to produce multiple reflections; the lasing threshold is attained when the roundtrip gain reaches unity. The FP laser diode cavity loss α_m and the photon lifetime, τ_{ph} , are given by:

$$\alpha_m = \frac{1}{2L} \ln \left(\frac{1}{R_1 R_2} \right) \quad (2.1.1)$$

$$\frac{1}{\tau_{ph}} = \nu_g (\alpha_m + \alpha_{int}) \quad (2.1.2)$$

where L is the laser cavity length, R_1 and R_2 are the two mirrors reflectivities, α_{int} is the internal losses, and ν_g is the group velocity.

A DFB laser uses a Bragg grating in the active region in order to suppress multiple longitudinal modes and enhance a single longitudinal mode, similar to the FP laser, the lasing threshold is obtained when the roundtrip gain reaches unity. The coupling coefficient κ for a DFB laser represents the coupling between the forward and backward traveling waves due to the active region refractive index periodic change (i.e, it determines the amount of feedback due to the grating structure).

Laser diode rate equations can be used to describe DFB lasers in the same way they are used to describe FP lasers. In order to apply the photon rate equation, the photon life time α_m is required. The threshold gain of DFB depends on the coupling strength κL . For a typical coupling strength $\kappa L = 2$, Figure 2.2 on page 9 yields [10]:

$$\alpha_m L \simeq 1.95 \quad (2.1.3)$$

for non-phase shifted DFB laser and

$$\alpha_m L \simeq 1.4 \quad (2.1.4)$$

for $\pi/2$ -phase shifted DFB laser

The DFB cavity loss α_m can be related to an effective reflectivity R ($R = R_1 = R_2$) for a given coupling strength κL [10]. As shown in Figure 2.2 on page 9, for a coupling

strength of $\kappa L = 2$, a DFB laser exhibits the same threshold gain as FP laser with facet reflectivities of $R = 0.25$ with $\pi/2$ phase shift, or of $R = 0.14$ without phase shift.

2.2 Conventional Laser Diode Rate Equations

Simplified single mode rate equations were expressed in many references as follows [14–18],

$$\frac{dP(t)}{dt} = \Gamma GP(t) + \Gamma \beta_{sp} \frac{C(t)}{\tau_e} - \frac{P(t)}{\tau_{ph}} \quad (2.2.1)$$

$$\frac{dC(t)}{dt} = \frac{I(t)}{qV_c} - GP(t) - \frac{C(t)}{\tau_e} \quad (2.2.2)$$

where $P(t)$ represents the intracavity photon density, C is the active region carrier density, Γ is the mode confinement factor, β_{sp} is the spontaneous emission factor, τ_e is the electron life time, τ_{ph} is the photon life time, $I(t)$ is the injected current, q is the electronic charge and V_c is the volume of the active region.

2.3 Modified Laser Diode Rate Equations

Many works have been done by Ghoniemy et al [19] in modifying the rate equations governing the dynamics of the laser diode theory. These include, semiconductor laser gain modifications [20], the effects of device heating [21], current leakage [22] and noise [23]. Results from these work concluded the following normalized laser rate equations:

$$\begin{aligned} \frac{dP_n(T, t)}{dt} = & \frac{(C_n(T, t) - C_{tr}^n(T))}{\tau_{ph}(T)(1 - C_{tr}^n(T))} \frac{P_n(T, t)}{\sqrt{1 + P_r^n(T, t)}} - \frac{P_n(T, t)}{\tau_{ph}(T)} \\ & + (\beta_{sp} B_o \tau_e(T) C_{tho} \exp(\frac{T - T_r}{T_o} - \frac{E_1 q}{K_B T})) C_n^2(T, t) + F_{P_n}(t) \end{aligned} \quad (2.3.1)$$

$$\frac{dC_n(T, t)}{dt} = \frac{I_{eff}(t)}{qV_c C_{th}(T)} - \frac{(C_n(T, t) - C_{tr}^n(T))}{\tau_e(T) \tau_{ph}(T) (1 - C_{tr}^n(T))} \frac{P_n(T, t)}{\sqrt{1 + P_r^n(T, t)}} - \frac{C_n(T, t)}{\tau_e(T)} + F_{C_n}(t) \quad (2.3.2)$$

$$\frac{d\Phi_n(t)}{dt} = \frac{\beta}{2} G_n (C_n(T, t) - \bar{C}_n) + F_{\Phi_n}(t) \quad (2.3.3)$$

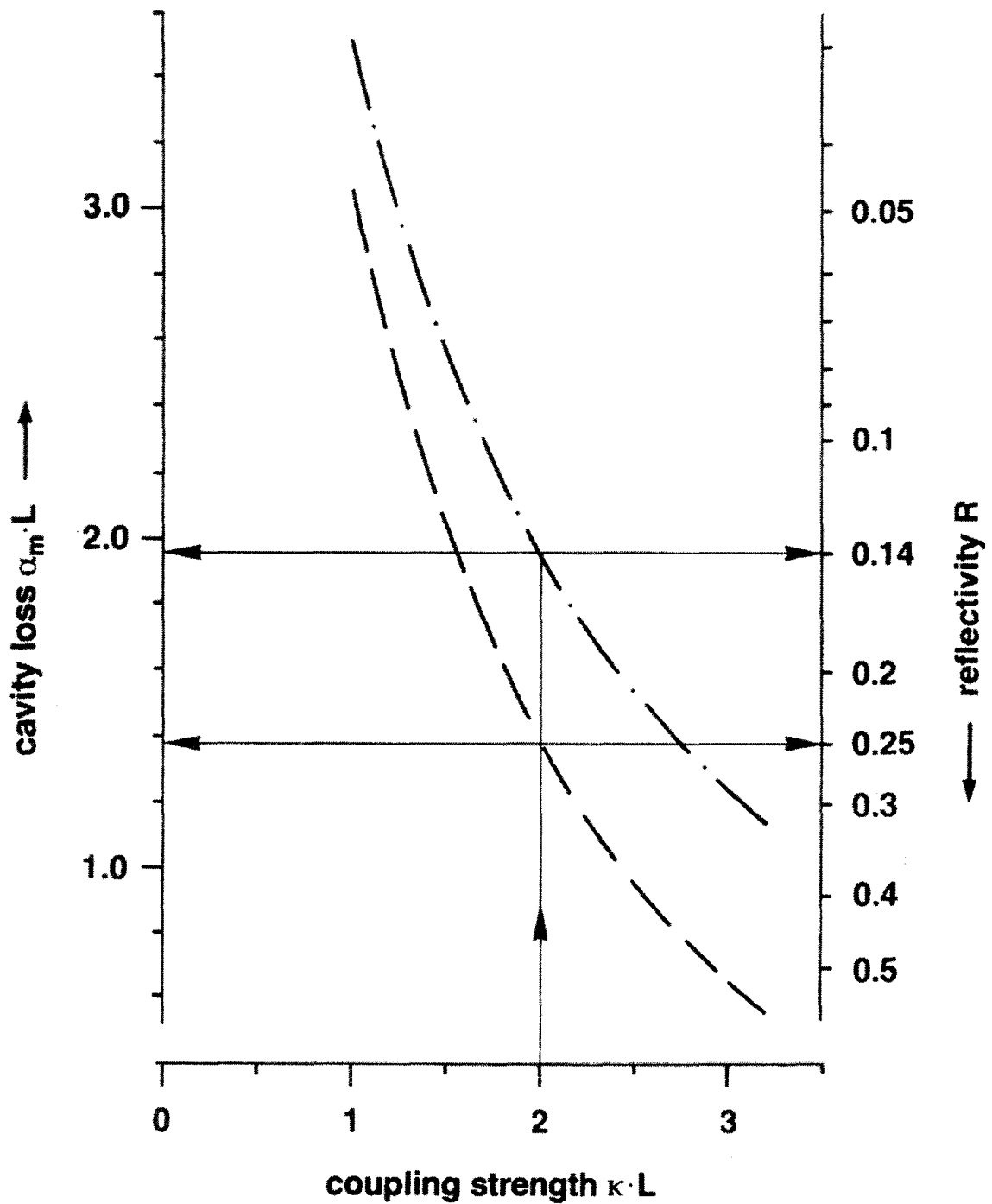


Figure 2.2: Cavity loss and related effective reflectivity for DFB lasers without phase adjustment (— · — · — · —) and with a $\pi/2$ -phase shift (— — — — —), reproduced from [10].

where $P_n(T, t)$ is the normalized photon density, $C_n(T, t)$ is the normalized carrier density, C_{tr} is the threshold carrier density, τ_{ph} is the photon life time, τ_e is the electron life time, β_{sp} is the spontaneous emission factor, T is the average active region temperature, T_o is the characteristic temperature of the active region, E_1 is the activation energy of the radiative recombination, T_r is the equilibrium temperature without injection, K_B is the Boltzman's Constant, B_o is the radiative recombination coefficient, $F_{P_n}(t)$ is the normalized photon Langevin noise sources, $I_{eff}(t)$ is the part of the external current that passes through the active region, q is the electronic charge, v_c is the volume of the active region, C_{th} is the threshold carrier density, $F_{C_n}(t)$ is the normalized carrier Langevin noise sources, $\Phi_n(t)$ is the normalized phase, β is the linewidth enhancement factor, \bar{C} is the mean of the carrier number, and $F_{\Phi_n}(t)$ is the normalized phase Langevin noise sources.

2.4 Feedback Regimes

Due to the need for coherent optical communication systems that require stable narrow linewidth sources, the effect of the optical back-reflections should be studied carefully. In [11] the laser operation in the presence of optical feedback was categorized into five regimes as follows:

- Regime I: At low feedback levels, narrowing or broadening of the laser spectrum is observed, depending on the phase of the reflected power. This was observed in [11] at a feedback level of -80 dB with an external reflector at a distance of 40 cm from the laser facet. It is difficult to remain in this regime for long external cavity lengths. Assuming τ_{ext} of 10 ns the effective external reflectivity must be lower than 10^{-8} which is very difficult to achieve practically and the laser quite unlikely remains in Regime I.
- Regime II: Rapid mode-hopping causes a splitting in the laser emission; this splitting magnitude depends on the feedback level and the reflector location. This allows for multiple cavity modes.
- Regime III: At higher levels of feedback (approximately -45 dB), independent of the reflector distance from the laser facet, the laser is observed to operate on a single narrow line again. The range of feedback level in this region is very small, and the

laser becomes sensitive to further reflections.

- Regime IV: Independent of the reflector distance and the feedback phase, and at a higher feedback level (approximately -40 dB), the laser linewidth broadens to as much as 50 GHz. This regime is also called coherence collapse regime. The coherence length of the laser is vastly reduced and the relative intensity noise increases to very high levels.
- Regime V: At high feedback levels (greater than -10 dB), the laser is driven to operate in the extended cavity operation with a narrow linewidth, the linewidth reduction is attributed to the low phase noise associated with this feedback regime. A long cavity is formed by the external reflector with only a short active region. The laser operates on a single longitudinal mode with narrow linewidth for all phases of the feedback. At this regime the feedback dominates the field in the laser, the laser becomes immune to any additional external optical reflections from the fiber transmission line because of the large round trip delay in these compound cavity lasers [10]. The phase of the feedback light suppress the intensity noise of the laser and the intensity noise decreases in this regime.

Figure 2.3 on the next page shows the aforementioned feedback regimes.

The spectra of a DFB laser diode with different feedback levels are shown in Figure 2.4 on page 13. Figure 2.4(a) shows the spectrum of the solitary laser diode operating in a single longitudinal mode. The influence of weak optical feedback is shown in Figure 2.4(b) under which the spectrum shows no change from that of the solitary laser. Multimode operation is reached when the feedback ratio is increased to a level that can drive the laser diode to the coherence collapse regime as shown in Figure 2.4(c). Further increase of the feedback ratio makes the laser again operate in a single mode, Regime V, as shown in Figure 2.4(d). The output power of the laser diode in this regime is higher than that of the solitary laser, this is because the threshold of the laser with feedback is reduced relative to the solitary value.

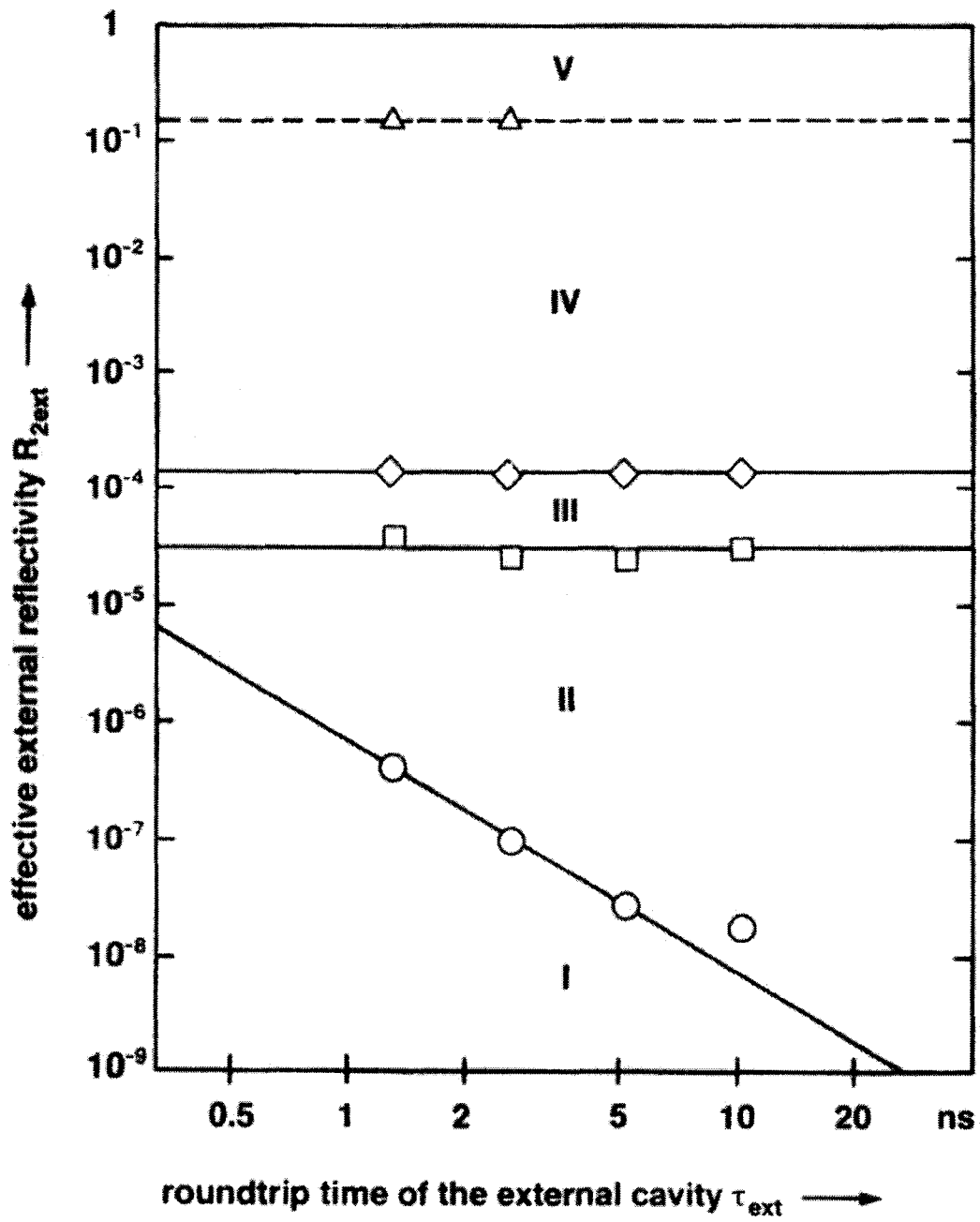


Figure 2.3: Different feedback regimes (Regime I - Regime V) for a DFB laser diode, reproduced from [11].

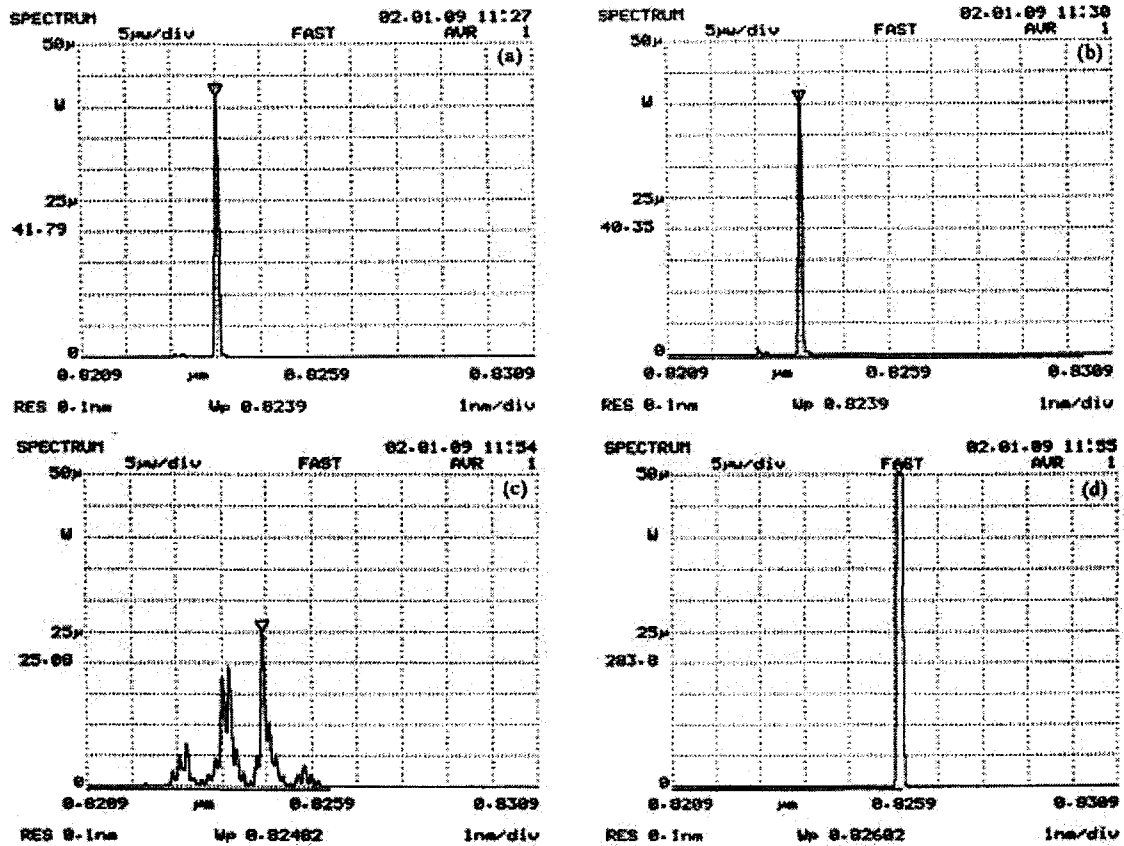


Figure 2.4: DFB laser diode spectra under different feedback levels: (a) the spectrum of the solitary laser diode, (b) DFB laser diode with weak feedback, (c) DFB laser diode operating in coherence collapse regime, and (d) DFB laser diode operating in feedback Regime V, reproduced from [12].

2.5 Conventional Laser Diode Rate Equations Including Optical Feedback effect

Optical back-reflections influence semiconductor laser diode nonlinearity and intensity noise, and can modify the static and dynamic characteristics. These reflections originate from the laser facet, laser/fiber interface, and fiber connectors. Rate equations typically neglect optical back-reflections for simplicity, therefore making them ill-suited for analysis of laser diode performance where optical back-reflection is significant. The following is a survey of some of the published work for the conventional laser diode rate equations that include the feedback effect.

Kikushima et al [24] reported an excess harmonic distortion due to the external coherent reflection. They added a term to the laser diode rate equations to describe the back-reflected light into the laser, but did not include the time delay of the reflected waves. It was concluded that in order to reduce feedback induced distortion an optical isolator of 30 dB should be used, this will reduce the reflection coefficient down to -50 dB.

Czylwik's analysis [25] included the time delay of the reflected waves in the feedback term to predict the upper bound on the harmonic distortion due to reflected waves. He showed an excess 2nd, 3rd, and 4th order harmonic distortion for the laser diode under -20 dB and -30 dB back-reflection ratios for distances 1 m and 3 m. However, he did not report on the other feedback regions, nor the laser diode's different behaviors under optical back-reflections.

Helms [26] showed theoretically and experimentally that optical feedback from the fiber enhanced the intermodulation and the harmonic distortion of the laser diode, and this can be achieved if the optical feedback level was kept under -60 dB.

Cohen et al [27] studied the effect of the optical feedback on the laser diode relaxation oscillation, and found that the relaxation oscillation is modified due to optical feedback.

Agrawal [28] studied the linewidth narrowing in a single-mode injection laser due to external optical feedback, and investigated the effect of fiber-far-end (7.5 km) reflections on intensity noise and phase noise in InGaAsP semiconductor lasers [29].

Schunk et al [30] measured the feedback-induced intensity noise for a 1.3 μm DFB laser diode, the RIN was experimentally measured for a wide feedback range from -80 dB

to -20 dB. They showed that the transition to the coherence collapse regime occurs at larger feedback levels if the laser is operated at larger optical powers; additionally, a large coupling strength in a DFB laser is beneficial in improving the stability against optical feedback. They also solved the nonlinear rate equations numerically [31] to estimate the external feedback effect on a single-mode semiconductor laser. They reported that the transition to the coherence-collapse regime occurs at a -40 dB feedback ratios, and this can be shifted to larger feedback ratio by either increasing the laser output power, laser cavity length, or decreasing the laser linewidth enhancement factor α .

Lang and Kobayashi [32] used an external reflector placed a few centimeters apart from the laser diode to investigate the influence of the optical feedback on the semiconductor laser properties. They found that the coherent reflection can either enhance or suppress the relaxation oscillation of the laser depending on interference conditions between returned waves and the field inside the laser diode. They introduced also the so-called Lang/Kobayashi rate equations.

Hirota et al [33] studied the noise properties of the laser diode under direct modulation and influenced by the reflected waves. They estimated the required optical isolation to be 30 dB to reduce the intensity noise of the laser.

Petermann et al [34] discussed the major sources of noise and distortions in optical fiber communication systems, and concluded that an optical isolator should be included between the laser and the fiber to achieve low distortions and low noise. Petermann attributed the mode hopping and the coherence collapse strong excess noise to the optical feedback phenomena [35].

Favre [36] has shown that the laser facet sensitivity to the optical feedback is related to the emitted power from that facet. It was found that DFB lasers are more sensitive to the feedback than FP lasers. Additionally, DFB lasers with larger κL was found to be relatively insensitive to optical feedback.

Way et al [37] controlled the optical feedback from -50 dB to -25 dB at the far end of a 2 m pigtail 1.3 μm DFB laser and a multimode laser and compared the linearity performance for both laser diodes. They found that by using suitable bias level and modulation frequency, both of the two types of lasers give good linearity even under strong feedback.

In [38] Helms et al presented a simple analytic expression describing the maximum feedback level under which the semiconductor laser can operate stably. They also calculated the RIN for several linewidth enhancement factors α .

Petermann [39] gave guidelines for designing semiconductor lasers immune to external optical feedback. The mode hopping, linewidth narrowing and broadening, and the transition to the coherence collapse regime due to the weak external optical feedback were reviewed.

Pan et al [40] investigated experimentally the behavior of a semiconductor laser under moderate to strong optical feedback, and showed that the standard Lang/Kobayashi rate equations [32] accurately predict the transition between feedback Regime IV and Regime V.

Jones et al [41] used Lang/Kobayashi rate equations [32] to study the effect of the external cavity length on the coherence collapse regime.

Hong et al [12] showed experimentally the optical spectra of the semiconductor laser subject to different levels of optical feedback. They also calculated the RIN within Regimes I to V. They found that at a low bias current the laser exhibits low RIN with low feedback ratio. The RIN increased too much in the coherence collapse regime (Regime IV) and decreased in Regime V to a level lower than that of the solitary laser. For higher bias current the transition from Regime IV to V needs higher feedback ratios.

In 2004, Ju et al [42] numerically calculated the RIN of semiconductor lasers under weak and strong feedback levels to identify the various feedback regimes, the modified Lang/Kobayashi model was used in the calculations.

2.6 Analysis of Feedback Phenomenon

The feedback phenomenon in semiconductor lasers can be analyzed based on the model shown in Figure 2.5 on the next page, consisting of laser facet reflection coefficients r_1 and r_{2s} , the external cavity reflection coefficient r_{2ext} , and the laser diode cavity length L . Introducing an effective reflection coefficient r_2 at $Z = L$, we obtain [10]:

$$r_2(v) = r_{2s} + (1 - |r_{2s}|^2)r_{2ext} \exp(-j2\pi\nu\tau_{ext}) \quad (2.6.1)$$

where ν is the optical frequency, and τ_{ext} is the round trip delay back and forth through

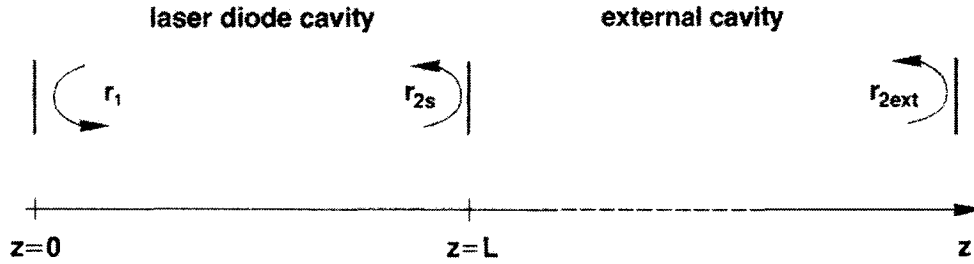


Figure 2.5: Schematic representation of a laser diode cavity with external feedback, reproduced from [10].

the external cavity of length L_{ext} . Also r_2 can be expressed with respect to amplitude and phase as

$$r_2(v) = |r_2|^2 \exp(-j\phi_r) \quad (2.6.2)$$

The laser diode phase condition is obtained by equating the round trip phase within the laser diode cavity to an integer multiple of 2π

$$2\beta L + \phi_r = 2\pi m \quad (2.6.3)$$

where m is integer and β is the propagation constant. For $\phi_r = 0$, this corresponds to the phase condition for the solitary laser. To obtain the the threshold gain $g = g_c$ that satisfies the amplitude condition for the compound cavity laser:

$$r_1 |r_2| \exp([g_c - \alpha_s]L) = 1 \quad (2.6.4)$$

The feedback strength is classified, based on the ratio between r_{2s} and r_{2ext} , into weak feedback $|r_{2ext}| \ll |r_{2s}|$ and strong feedback $|r_{2ext}| \gg |r_{2s}|$. We will analyze the amplitude and phase condition for the weak feedback case. On the other hand, the analysis of the strong feedback and the dynamics of laser diodes requires a numerical analysis for the laser diode rate equations that include the feedback term. The reflection coefficients r_{2s}, r_{2ext} may be considered as real and positive values, so that (2.6.1) yields

$$|r_2| = r_{2s}(1 + \kappa_{ext} \cos(2\pi\nu\tau_{ext})) \quad (2.6.5)$$

where κ_{ext} is the coupling coefficient to the external cavity and is defined as:

$$\kappa_{ext} = \frac{r_{2ext}}{r_{2s}}(1 - |r_{2s}|^2) \quad (2.6.6)$$

and

$$\phi_r = \kappa_{ext} \sin(2\pi\nu\tau_{ext}) \quad (2.6.7)$$

for $\kappa_{ext} \ll 1$. There is another feedback coefficient C that can describe the feedback strength and is defined as:

$$C = X\sqrt{1 + \alpha^2} \quad (2.6.8)$$

with

$$X = \frac{\tau_{ext}}{\tau_L} \kappa_{ext} \quad (2.6.9)$$

where α is the linewidth enhancement factor, τ_{ext} is the round trip delay, back and forth through the external cavity, τ_L is the laser round trip delay. The phase condition in (2.6.3 on the preceding page) may be rewritten in terms of the effective refractive index $\mu_e = c\beta/(2\pi\nu)$ as

$$4\pi\mu_e\nu L/c + \phi_r = 2\pi m \quad (2.6.10)$$

The emission frequency $\nu = \nu_{th}$ is obtained when $\phi_r = 0$ (without feedback).

The emission frequency, the threshold gain, and the refractive index may change due to weak feedback, yielding a change of $\mu_e\nu$ given by,

$$\Delta(\mu_e \nu) = \nu_{th}\Delta\mu_e + (\nu - \nu_{th})\mu_e \quad (2.6.11)$$

Expressing (2.6.11) in the phase condition yields

$$\Delta\phi_L = \Delta(\mu_e \nu)4\pi L/c + \phi_r = (4\pi L/c) [\nu_{th}\Delta\mu_e + \mu_e(\nu - \nu_{th})] + \phi_r \quad (2.6.12)$$

where $\Delta\phi_L$ corresponds to a change in the round trip phase compared to $2\pi m$. As the compound cavity round trip phase must equal to $2\pi m$, the emission frequencies are obtained from (2.6.12) for $\Delta\phi_L=0$ (or 2π multiples). The refractive index change $\Delta\mu_e$ may be given as

$$\Delta\mu_e = \frac{\partial\mu_e}{\partial n}(n - n_{th}) + \frac{\partial\mu_e}{\partial v}(v - v_{th}) \quad (2.6.13)$$

where n_{th} is the threshold carrier density without feedback. Combining (2.6.12) and (2.6.13) yields

$$\Delta\phi_L = \frac{4\pi L}{c} \left[v_{th} \frac{\partial\mu_e}{\partial n}(n - n_{th}) + \bar{\mu}_e(v - v_{th}) \right] + \phi_r \quad (2.6.14)$$

where $\bar{\mu}_e$ is the effective group refractive index.

The linewidth enhancement factor α links the variation of the refractive index with varying carrier density $\frac{\partial\mu_e}{\partial n}$ and the gain variations $\frac{\partial g}{\partial n}$ through the following relation [10]:

$$\frac{\partial\mu_e}{\partial n} = \alpha \frac{\partial\mu_e''}{\partial n} = -\alpha \frac{\partial g}{\partial n} \frac{c}{4\pi v_{th}} \quad (2.6.15)$$

with the complex effective refractive index $\mu_e = \mu_e' - j\mu_e''$, and $\alpha = \delta\mu_e'/\delta\mu_e''$. Hence

$$\frac{\partial\mu_e}{\partial n}(n - n_{th}) = -\frac{\alpha c}{4\pi v_{th}}(g - g_{th}) \quad (2.6.16)$$

As the amplitude condition must be satisfied with g equal to the threshold gain for the compound cavity g_c , (2.6.16) implies

$$\Delta\phi_L = -\alpha(g_c - g_{th})L + \frac{4\pi\bar{\mu}_e L}{c}(v - v_{th}) + \phi_r \quad (2.6.17)$$

where g_{th} is the threshold gain without feedback and is given by,

$$g_{th} = \alpha_s + L^{-1} \ln(1/r_1 r_{2s}) \quad (2.6.18)$$

The threshold gain difference ($g_c - g_{th}$) due to feedback obtained from (2.6.4) and (2.6.5), for $\kappa_{ext} \ll 1$ is given by,

$$(g_c - g_{th}) = -\frac{\kappa_{ext}}{L} \cos(2\pi\nu\tau_{ext}). \quad (2.6.19)$$

The round trip phase change $\Delta\phi_L$ is obtained from (2.6.7), (2.6.17), and (2.6.19) as,

$$\Delta\phi_L = \frac{4\pi\bar{\mu}_e L}{c}(\nu - \nu_{th}) + \kappa_{ext}[\sin(2\pi\nu\tau_{ext}) + \alpha \cos(2\pi\nu\tau_{ext})]. \quad (2.6.20)$$

Introducing the round trip delay of the solitary laser cavity $\tau_L = 2\bar{\mu}_e L/c$, the round trip phase change $\Delta\phi_L$ can be rewritten as [10],

$$\Delta\phi_L = 2\pi\tau_L(\nu - \nu_{th}) + \kappa_{ext}\sqrt{1 + \alpha^2} \sin(2\pi\nu\tau_{ext} + \arctan \alpha). \quad (2.6.21)$$

The laser diode threshold gain is either reduced or increased depending on the phase of the reflected light $\phi_{ext} = 2\pi\nu\tau_{ext}$. The maximum reduction occurs when ϕ_{ext} is an integer multiple of 2π (in phase feedback).

Figure 2.6 on the next page shows a plot for the round trip phase change $\Delta\phi_L$ versus the frequency $\nu - \nu_{th}$. The phase condition is satisfied when $\Delta\phi_L = 0$, at which the possible emission frequencies are expected. Without feedback, the round trip phase change $\Delta\phi_L$ varies linearly with frequency ν , yielding a single zero at $\nu = \nu_{th}$. For very small feedback level $C < 1$, the round trip phase change $\Delta\phi_L$ monotonically increases with ν , again yielding a single zero at $\nu = \nu_{th}$, i.e., single emission frequency. For high feedback level $C > 1$, the round trip phase change $\Delta\phi_L$ undergoes strong oscillations yielding multiple zeros for $\Delta\phi_L$, at which several external cavity modes around the emission frequency ν_{th} of the solitary laser may oscillate.

The above analysis is carried out for FP lasers, it uses the reflectivity $R_{2s} = r_{2s}^2$ of the laser mirror. To be able to apply the same analysis to DFB lasers, the FP laser mirror reflectivity should be related to the DFB coupling, κL , as in Figure 2.2 on page 9.

Equations (2.6.6), (2.6.8), and (2.6.9) govern the feedback sensitivity of laser diodes. For a given external cavity with a given R_{2ext} and τ_{ext} the feedback sensitivity depends on R_{2s} and τ_L . Larger values for R_{2s} and τ_L make the laser less sensitive for the feedback due to the low values of C and X. Given that κL is usually small for DFB lasers, the related effective reflectivity is also small. Additionally, the effective round trip delay for DFB lasers is smaller when compared to that of FP lasers of the same cavity length. DFB lasers are therefore more sensitive to feedback than FP lasers.

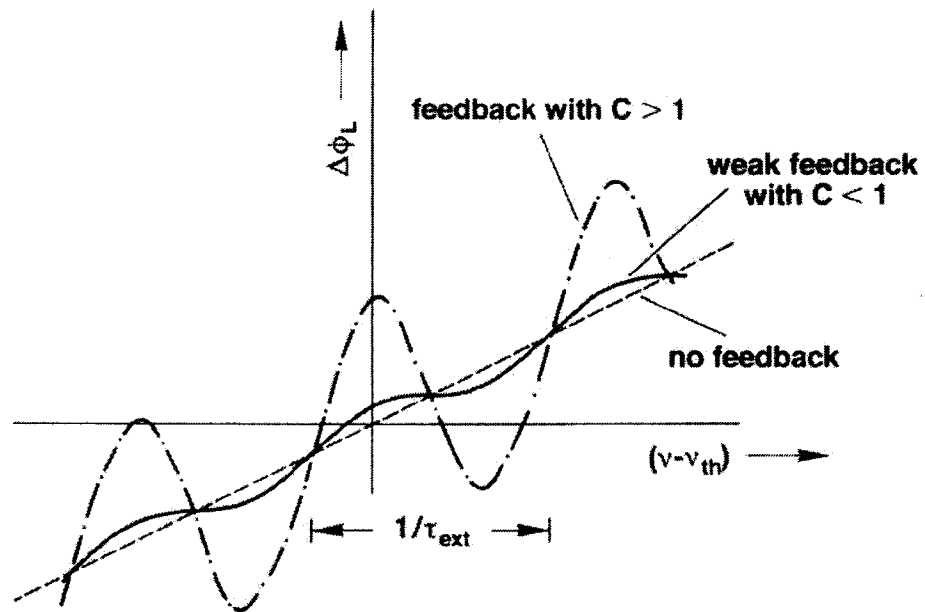


Figure 2.6: Round trip phase change $\Delta\phi_L$ versus the optical frequency $\nu - \nu_{th}$ with no feedback, weak feedback with $C < 1$, and feedback with $C > 1$, reproduced from [13].

DFB laser feedback sensitivity may be reduced for large grating coupling coefficient κ , but for large κ , the DFB laser diode external quantum efficiency is reduced. Thus, κL should be chosen carefully.

2.7 Changes to Laser Performance due to External Cavity

When coupling the light of the laser diode to an optical fiber, the optical fiber front face represents a reflector, creating an unwanted short external cavity. A tapped fiber end with a hemispherical end face is used to achieve high coupling efficiency and low feedback level. The optimum hemispherical end radius is of the order of $15 \mu\text{m}$, yielding coupling distance of $L_{ext} \simeq 30 \mu\text{m}$, and external reflectivity of the order of 10^{-5} to 10^{-4} [43], which is large enough to change the laser diode spectral characteristics.

2.7.1 Emission Frequency Shift due to Feedback

The laser diode emission frequency is affected by optical feedback. For short external cavities, the parameter C according to (2.6.9 on page 18) is small ($C < 1$) and $\Delta\phi_L$ versus ν is still a monotonic function. This means that no additional modes due to optical feedback will be of concern. The phase equation (2.6.21 on page 20) is satisfied for $\Delta\phi_L = 0$ yielding,

$$\nu - \nu_{th} = \Delta\nu_{\max} \sin(2\pi\nu\tau_{ext} + \arctan \alpha) \quad (2.7.1)$$

and then the maximum frequency shift due to feedback is given by,

$$\Delta\nu_{\max} = \frac{\kappa_{ext}\sqrt{1 + \alpha^2}}{2\pi\tau_L}. \quad (2.7.2)$$

The above equation shows that even with the feedback level as low as 10^{-4} , facet reflectivity $R_{2s} = 0.32$, $\kappa_{ext} = 1.2 \times 10^{-2}$, $\alpha = 6$, and $\tau_L = 10$ ps, the maximum frequency shift is $\Delta\nu_{\max} \simeq 1.2$ GHz, which has been observed experimentally in [44]. Even using optical isolators, we cannot guarantee complete removal of the optical back-reflections, and we must still consider the feedback from the isolator's front face.

2.7.2 Single External Cavity Mode Condition

For low external feedback level, the single mode condition (for an arbitrary feedback phase) is satisfied when $C < 1$. Larger feedback coefficients may result in a single oscillating frequency if restrictions on ϕ_{ext} are applied. The feedback coefficient C may be tolerated up to $3\pi/2$ if the feedback phase is carefully adjusted [10]. For high feedback level, it is still possible for the laser to emit in a single frequency within certain feedback regime.

2.7.3 Spectral Linewidth Change due to Optical Feedback

The laser diode spectral linewidth may be influenced considerably due to optical feedback. The spectral linewidth $\Delta\nu$ can be derived from (2.6.21) as [39],

$$\Delta\nu \sim [d(\Delta\phi_L)/d\nu]^{-2} \quad \text{at} \quad \Delta\phi_L = 0 \quad (2.7.3)$$

yielding,

$$\Delta\nu = \frac{\Delta\nu_0}{[1 + C \cos(\phi_{ext} + \arctan\alpha)]^2} \quad (2.7.4)$$

where $\Delta\nu_0$ is the linewidth of the solitary laser without feedback, and $\phi_{ext} = 2\pi\nu\tau_{ext}$. For $C \approx 1$, no additional external cavity modes are introduced. Depending on the feedback phase ϕ_{ext} the linewidth varies between minimum linewidth

$$\Delta\nu_{\min} = \frac{\Delta\nu_0}{(1 + C)^2} \quad (2.7.5)$$

and maximum linewidth

$$\Delta\nu_{\max} = \frac{\Delta\nu_0}{(1 - C)^2}. \quad (2.7.6)$$

2.7.4 Phase and Frequency Noise of Laser with Optical Back-reflections

For low feedback levels, the frequency noise spectrum can be evaluated analytically as described in [45]. For high levels of feedback, a numerical analysis for the laser diode rate equations is required to evaluate the frequency noise. Figure 2.7 on the next page

shows the calculated frequency noise spectrum for a 1 m long external cavity at a feedback ratio of 2.5×10^{-5} , this amount of feedback corresponds to Regime III. The frequency noise is suppressed and its spectrum shows a white noise behavior for frequencies lower than the inverse external round trip time $1/\tau_{ext}$, yielding the strong linewidth narrowing. The frequency noise spectrum exhibits peaks at frequencies corresponding to multiples of $1/\tau_{ext}$.

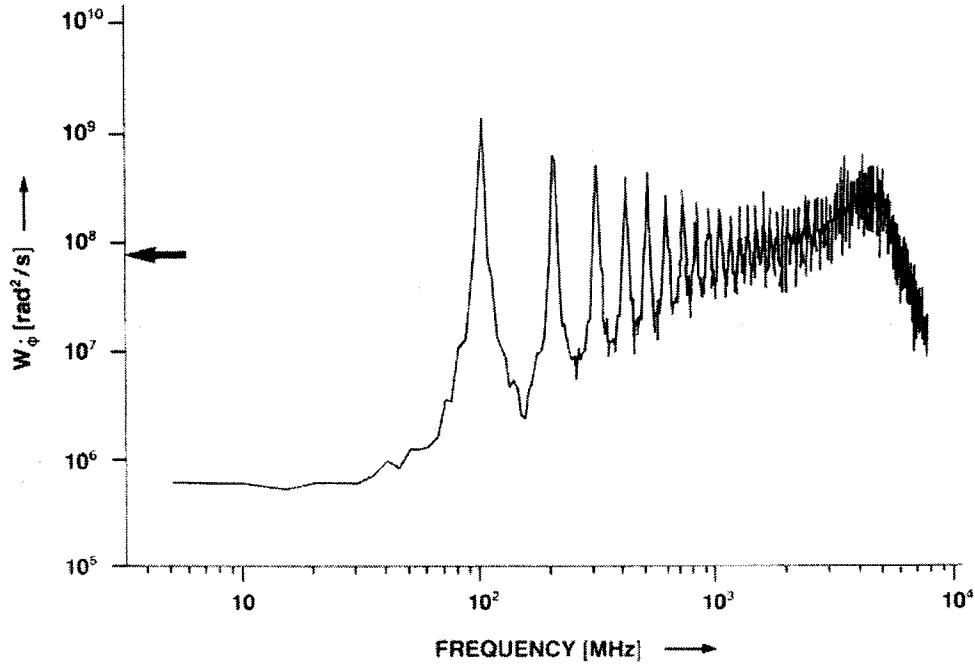


Figure 2.7: Calculated frequency noise spectrum for 1 m long external cavity at a feedback fraction of 2.5×10^{-5} for the solitary laser diode, reproduced from [46].

2.7.5 Laser Intensity Noise due to Optical Feedback

Considering a single mode DFB laser diode with optical feedback, a numerical analysis for the laser diode rate equations yields the RIN shown in Figure 2.8 on page 26. RIN remains relatively low for $R_{2ext} < 10^{-4}$, and it drastically increases for $R_{2ext} > 10^{-4}$. The sharp increase in the RIN is due to the transition between Regimes III and IV. Any further increase in the feedback level drives the laser to feedback Regime V, at which the RIN is decreased to a value lower than that of the solitary laser, as shown in Figure 2.9 for the

measured RIN at different feedback levels [12].

2.7.6 Dynamic Properties of Laser with External Cavity

The modulation characteristics of external cavity lasers can be described by the laser diode rate equations that include the optical back-reflections term. The modulation characteristics of the external cavity laser with very short external cavity lengths (a few hundred microns) are similar to those of solitary lasers, almost no change due to the optical back-reflections. For external cavity length ranges from few millimeters up to 2 *cm*, and depending on the reflected light phase, an enhancement or damping of the relaxation oscillations may occur due to the optical back-reflections.

2.8 CATV Systems

Cable Television (CATV) system uses bi-directional signal transmission in order to enable the distribution of TV signals and a range of various other services such as radio and satellite signals. The bi-directional communication nature of CATV makes it possible to receive signals (TV, radio program, etc) passively as well as enable users to select the type and content of the offered services.

Today's CATV networks use a Hybrid Fiber/Coax (HFC) configuration to reduce cost while increasing performance and transmission range. This is achieved by exploiting the large bandwidth and low loss offered by optical fibers. An HFC network uses coaxial cable for shorter transmission lengths often between video equipment and the transmitter, or the receiver. On the other hand, the transmitter and the receiver are connected using single-mode optical fiber in order to extend the transmission distances by orders of magnitude, thereby reducing the number of RF amplifiers (spaced every 300-600 m) often associated with coaxial cables. This combination of coaxial cables and optical fibers allows system designers to employ the lowest cost solution for each portion of the network. CATV systems can carry more than 100 analog channels spaced at 6 MHz intervals.

A typical CATV system comprises a CATV transmitter and receiver. Figure 2.10 on page 28 illustrates the basic structure of a HFC CATV system. A CATV receiver contains a PIN detector which is considered one of the most linear optical components. A CATV

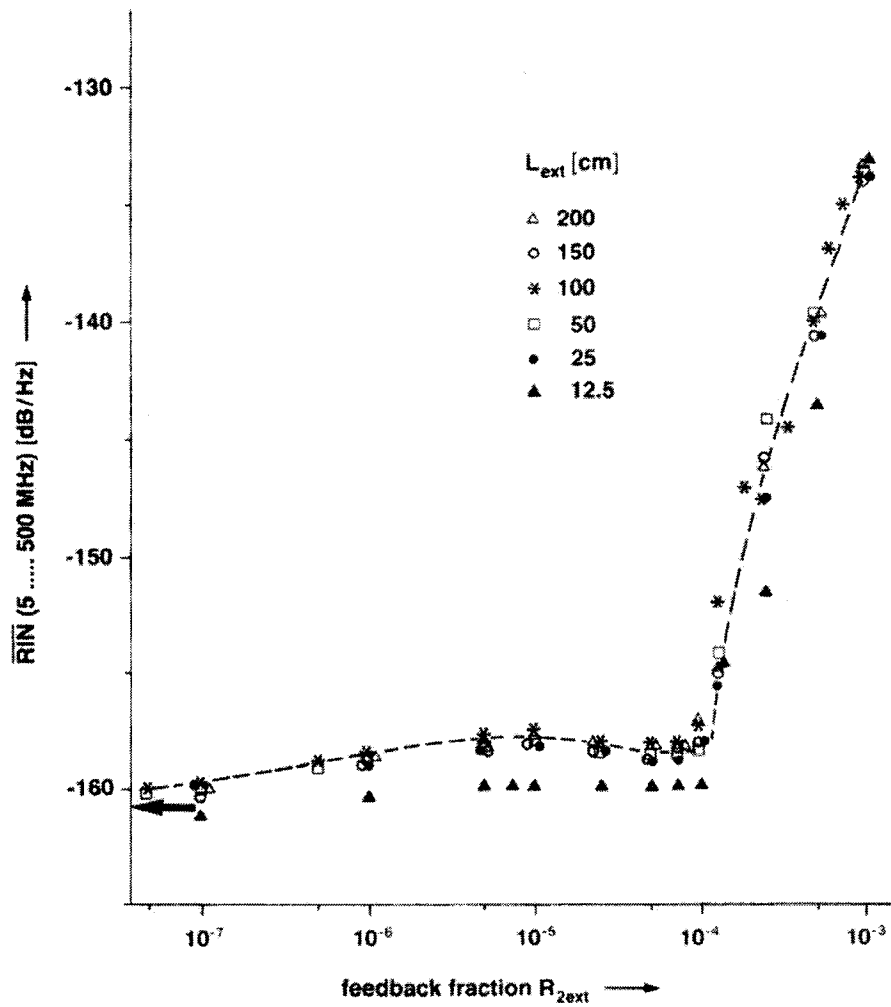


Figure 2.8: Calculated relative intensity noise averaged over the frequency range 5 ··· 500 MHz versus the feedback fraction for various external cavity lengths at an output power (5 mW), reproduced from [31].

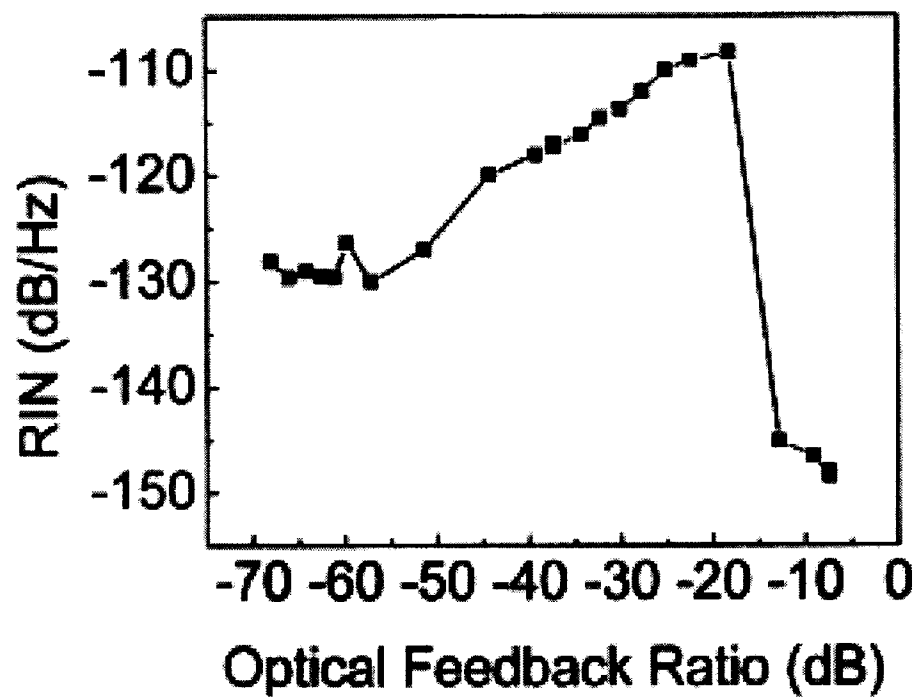


Figure 2.9: Measured relative intensity noise as a function of feedback ratio with 29.3 mA laser bias current, reproduced from [12].

transmitter employs a laser diode; the biggest challenge usually lies within the nonlinear nature of the laser. 1310 nm DFB lasers dominated CATV transmission for many years. Many enhancements to improve the lasers' linearity as well as to lower their Relative Intensity Noise (RIN) were implemented. Recently, the popularity of 1550 nm wavelength allows transmission distance to increase from 20-30 km to 60-70 km [1]. Nonetheless, nonlinear distortions and intensity noise introduced by lasers can degrade the system performance as well as limit the maximum transmission distance.

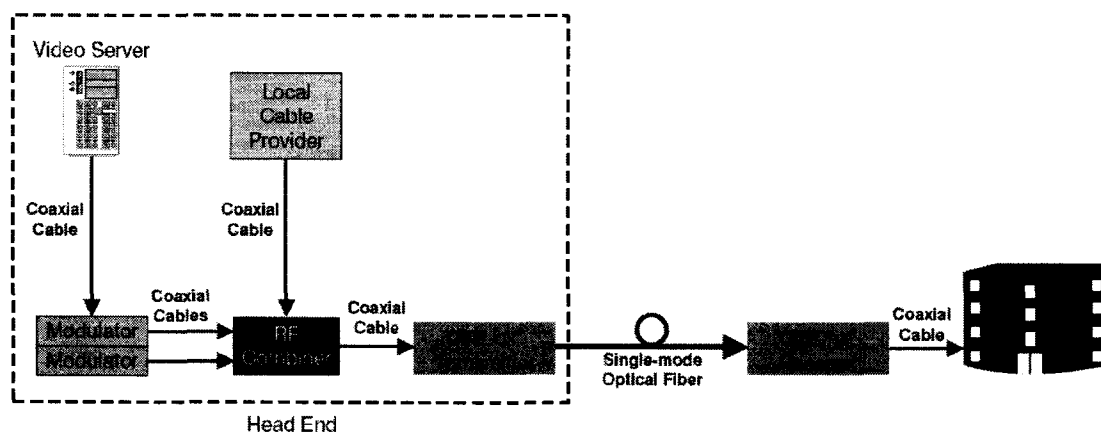


Figure 2.10: Basic structure of a Hybrid Fiber/Coax 1310/1550 nm CATV system. Reproduced from Force Incorporated (www.forceinc.com).

2.8.1 CATV Transmitter Performance

In this section we will discuss the performance of CATV transmitter. We will start with the laser noise and then discuss how the laser linearity affect the CATV performance. A typical CATV transmitter specifications is given at the end of the section.

CATV Transmitter Noise

Carrier-to-Noise Ratio (CNR) is defined as the ratio of the carrier to the total noise power in a 4 MHz bandwidth. Analog CATV signals require a CNR around 50 dB for acceptable picture quality. RIN from the laser is one of the major factors that limit the CNR. Low RIN is highly recommended for the DFB lasers in order to achieve the desired CRN for

analog CATV systems [4].

CATV Transmitter Linearity

Composite Triple Beat (CTB) and Composite Second Order (CSO) are two important measures of linearity in wideband systems handling many signals simultaneously such as CATV systems. To characterize CATV system linearity, N signals of equal power level are applied to the system spaced 6 MHz apart [47].

Considering three signals of equal amplitude, x_1 , x_2 , and x_3 , the third order nonlinearity results in:

$$\begin{aligned} (x_1 + x_2 + x_3)^3 &= x_1^3 + x_2^3 + x_3^3 \\ &+ 3x_1^2x_2 + 3x_1^2x_3 + 3x_2^2x_1 + 3x_2^2x_3 + 3x_3^2x_1 + 3x_3^2x_2 \\ &+ 6x_1x_2x_3 \end{aligned} \quad (2.8.1)$$

The first line of (2.8.1) causes third order harmonics (HD3), second line causes third order intermodulation (IM3), and last line causes CTB in that it creates terms at frequencies $(f_1 \pm f_2 \pm f_3)$. Except for the case where all three frequencies are added ($f_1 + f_2 + f_3$), these tones can fill into any of the channels being used and many will fall into the same channel.

Similar to CTB, CSO is used to measure CATV system linearity. For N signals of same power, consider the second order distortion products of each pair of signals falling at frequencies $(f_1 \pm f_2)$. If the carriers are not some even multiple of the channel spacing, the signals fall at frequencies either above or below the carriers instead of falling right on top of them as in the case of the triple-beat terms.

The Intercept Point is a common distortion specification for nonlinear systems. If the output versus input of a device is displayed graphically on a logarithmic versus logarithmic scale, the slope of the linear portion will be "1". If second and third order distortion products are displayed on the same scale, they will have a slope of "2" and "3" respectively. The third order intercept point, $IP3$, is a theoretical point where the amplitudes of the intermodulation tones at $2f_1 - f_2$ and $2f_2 - f_1$ are equal to the amplitudes of the fundamental tones at f_1 and f_2 . The power at this point, P_{IP3} , is given by,

$$P_{IP3} = P_i + \frac{1}{2}[P_1 - P_3] \quad (2.8.2)$$

where, P_i is the input signal power, P_1 is the output power at the fundamental frequency, and P_3 is the output power at the IM3 frequency.

Similar to $IP3$, the second order intercept point, $IP2$, can be defined in a similar way. The power at this point, P_{IP2} , is given by,

$$P_{IP2} = P_i + \frac{1}{2}[P_1 - P_2] \quad (2.8.3)$$

where P_2 is the output power at the second order intermodulation frequency, $IM2$.

The power of the Triple Beat (TB) and the Second Order beat (SO) tones are given by (2.8.4) and (2.8.5) respectively [47].

$$TB(dBm) = P_{IP3} - 3(P_{IP3} - P_s) + 6 \quad (2.8.4)$$

$$SO(dBm) = P_{IP2} - 2(P_{IP2} - P_s) \quad (2.8.5)$$

where P_s is the fundamental tone signal power. It is highly desirable to decrease the level of the TB and SO tones in order to get CTB and CSO distortions to a minimum. This can be achieved by decreasing second and third order intermodulation distortions, P_2 and P_3 , consequently increasing P_{IP2} and P_{IP3} . This will decrease the TB and SO levels. To meet CSO and CTB requirements for CATV systems, the laser's second order harmonic distortion and third order intermodulation distortion of types ($2f_1 \pm f_2$ and $2f_2 \pm f_1$) must be in the vicinity of -75 dBc and -100 dBc respectively, for a modulation index of 0.04 [4].

Typical CATV Transmitter Performance

Table 2.1 on the following page lists the typical CATV transmitter related specifications. Carrier-to-Noise Ratio (CNR) is determined both by the number of transmitted channels, as well as the received optical power at the input of the receiver. CNR is highly affected by the laser RIN; increasing the RIN decreases the CNR. Composite Second Order (CSO) and Composite Triple Beat (CTB) are measures of CATV transmitter linearity. Both attributes are affected by various types of laser distortions; increasing a laser's second order harmonic

distortion, third order harmonic distortion, or intermodulation distortions, increases CSO and CTB.

Specification	Minimum	Typical	Maximum	Units
Channel Loading			110	Channels
Operating Wavelength	1290	1310	1330	nm
Optical Output Power	+6		+13	dBm
Required Fiber Bandwidth	1,000			MHz
CNR		50		dB
CSO		-64	-62	dB
CTB		-69	-67	dB
Side Mode Suppression Ratio		30		dB
Back-reflection Tolerance			-50	dB
Operating Temperature Range	0		45	°C

Table 2.1: Typical CATV transmitter specifications, reproduced after [1].

2.8.2 Limiting Factors to CATV System Performance

Many factors limit the performance of CATV systems. Most important of these factors include:

- Laser nonlinearity.
- Optical back-reflections in the fiber plant.
- Fiber nonlinearities.
- Stimulated Brillouin scattering.
- Fiber-induced relative intensity noise.

In this section we will discuss the first two factors. Over the years, laser manufacturers have developed chip designs that have improved linearity [1]. Today one can find 10 dBm lasers that can carry 77 or more analog channels and deliver CSO and CTB better than -55 dB. However, there is a price to pay for this performance; high linearity lasers require extensive screening that results in low yields.

Several linearization techniques were reviewed in [19] to compensate for distortions these included: optical feedback and optical feed-forward, post-distortion, and pre-distortion. The analysis made in [19] supported the use of pre-distortion techniques. The laser linearity

can be improved using predistortion circuits. Complex predistortion circuits have a wide room for adjustments. Hence, each laser has its own custom-tuned predistortion board.

The CNR of a CATV system is limited by the laser's RIN. One major factor increasing the RIN and distortion is optical back-reflections which can modify the static and dynamic characteristics of the laser. These reflections originate from the laser facet, laser/fiber interface, and fiber connectors. Optical isolators were used to reduced the level of the reflected optical power. The use of optical isolators cannot completely remove the optical feedback effect since the built-in isolators typically allow for an isolation level of around 30 dB, which is insufficient in some applications.

2.9 Motivation

Most current DFB laser modules contain a built-in optical isolator to reduce the noise and distortion induced by optical back-reflections. The optical isolator increases costs and complicates the construction of multi-function integrated devices. Extra time is required to optically align the isolator. An uncooled, isolator free laser module is desirable for low cost lasers. A significant amount of previous research aimed at removing the isolator [48–52].

Hence, a need for a comprehensive laser model which has the ability to predict the laser diode performance due to the reflected waves is required.

The laser spectrum is narrowed for all feedback phases only in Regime V; it becomes insensitive to further reflections. In general this regime cannot be achieved for uncoated lasers without intentional external reflections. Otherwise the laser will suffer a degradation due to unintended reflections from splices and connectors (typically -30 to -40 dB). The 30 dB isolators will not be enough to prevent the broadening of the spectral linewidth [11].

The challenge is to force the laser to operate in Regime V. FBG provides a good solution: including a suitable external FBG in the fiber pigtail can drive the laser diode to operate in Regime V. The FBG can be implemented using a simple and cheap technique. The laser output power reduction due to the presence of the grating is self-compensated as the optical feedback from the grating reduces the laser threshold as will be shown in Section 4.2.1.

To meet linearity requirements for CATV systems, an effective linearization technique

is required to compensate for the laser's nonlinearity. This linearization technique should take into account major causes for the laser nonlinearity.

In this work, two major objectives were accomplished. Firstly, improve laser RIN and hence achieve the desired CNR required for CATV systems. Secondly, achieve lower levels of CTB and CSO by decreasing the various laser harmonic and intermodulation distortions. The first objective was achieved by a feedback topology that favorably applies optical feedback to the DFB laser in order to overcome the feedback induced RIN and get rid of the optical isolator. Since existing laser models do not enable designers to properly simulate laser with optical back-reflection, laser rate equations that include the optical feedback effect were implemented. This enabled us to build a laser model that has the ability to analyze various laser performance parameters taking into account optical feedback. Furthermore, based on the proposed rate equations, we developed a laser predistorter model. Simulation results shows that a considerable improvement in the laser's linearity was achieved when the laser model was cascaded to the predistorter. This improvement makes the laser suitable for CATV applications, hence fulfilling our second set objective.

Chapter 3

Proposed Model and Simulation Results

3.1 Introduction

Introducing the effects of optical back-reflections to the laser diode rate equations came with the challenge of solving the resulting complicated rate equations. Attempts to find numerical solutions met convergence difficulty. Such convergence problems can be avoided with a suitable normalization technique that can enhance the convergence of numerical solvers. In this chapter the proposed rate equations which include the optical back-reflection effects are introduced. The introduced feedback terms are derived and normalized. An Agilent-ADS model for system level simulation will be implemented based on the new proposed rate equations. DC, transient, and harmonic balance simulation results will be demonstrated.

3.2 The Proposed Rate Equations

The analysis of a laser diode with optical back-reflections involves comprehensive rate equations that have the ability to describe linearity and noise characteristics. Ghoniemy et al [19] introduced a comprehensive laser model that included semiconductor laser gain modifications and the effects of device heating, current leakage, and noise. This model has been augmented to include feedback terms that account for optical back-reflections phenomenon. Two different feedback terms have been added to the photon rate equation and phase rate equation; the electron rate equation remains unchanged.

3.2.1 Derivation of the Feedback Terms

Consider the model shown in Figure 2.5 on page 17. Starting from the first principles and using the technique presented in [10], the laser oscillation occurs when:

$$r_1 r_2 \exp(-2j\beta L + (g - \alpha_s)L) = 1 \quad (3.2.1)$$

with:

$$r_2 = |r_2| \exp(-j\phi_r) = r_{2s} + (1 - |r_{2s}|^2) r_{2ext} \exp(-j2\pi\nu\tau_{ext}) \quad (3.2.2)$$

where r_1 and r_{2s} are the laser facet reflection coefficients, r_2 is the effective reflection coefficient at $Z = L$, g in this equation accounts for the compound cavity stimulated emission gain, α_s is the optical loss (scattering loss), L is the laser cavity length, ϕ_r is the reflected power phase, and β is the optical wave phase constant. The $(1 - |r_{2s}|^2)$ term represents the light transmission through the exit facet of the laser diode.

The required gain condition is obtained from the absolute value of (3.2.1), while the phase condition is obtained from the phase of (3.2.1). With real values for $r_1 = \sqrt{R_1}$ and $r_2 = \sqrt{R_2}$, where R_1 and R_2 are the laser facets' power reflectivities, the phase and amplitude conditions of the compound cavity are given by (2.6.3 on page 17) and (2.6.4 on page 17) respectively.

Considering the case of a solitary laser diode for the moment, the phase constant, β , depends on the optical frequency ν and the possible emission frequencies are obtained from (2.6.3) (with $\phi_r = 0$). Introducing the effective refractive index μ_e for the lasing mode as:

$$\mu_e = c \frac{\beta}{2\pi\nu} \quad (3.2.3)$$

and the possible frequencies are:

$$\nu = \frac{mc}{2L\mu_e} \quad (3.2.4)$$

The effective group refractive index $\bar{\mu}_e$ is given by

$$\bar{\mu}_e = \mu_e + \frac{d\mu_e}{d\nu} \quad (3.2.5)$$

The spacing between two adjacent emission frequencies $\delta\nu$ is defined by

$$\delta\nu = \frac{c}{2L\bar{\mu}_e} \quad (3.2.6)$$

The round trip time delay τ_L corresponds to the inverse of the spacing between adjacent emission frequencies $1/\delta\nu$, therefore,

$$\tau_L = \frac{2L\bar{\mu}_e}{c}. \quad (3.2.7)$$

Introducing the carrier density at the lasing threshold, n_{th} , $g(n_{th}) = g_{th}$, and because of the dependance of the effective refractive index, μ_e , on the optical frequency and the carrier density, the resonance frequency, ν_{th} , at $n = n_{th}$ is obtained from:

$$\nu_{th} = \frac{mc}{2L\mu_e(\nu_{th}, n_{th})}. \quad (3.2.8)$$

If the carrier density deviates slightly from n_{th} , the effective refractive index μ_e can be expanded in terms of ν_{th} and n_{th} , yielding:

$$\mu_e = \mu_e(\nu_{th}, n_{th}) + \frac{\partial\mu_e}{\partial\nu}(\nu - \nu_{th}) + \frac{\partial\mu_e}{\partial n}(n - n_{th}). \quad (3.2.9)$$

Combining (3.2.4), (3.2.8), and (3.2.9) gives:

$$(\nu - \nu_{th}) = \frac{\nu_{th}}{\bar{\mu}_e} \frac{\partial\mu_e}{\partial n}(n - n_{th}) \quad (3.2.10)$$

The round trip gain, G , is given by:

$$G = r_1 r_2 \exp(-2j\beta L + (g - \alpha_s)L). \quad (3.2.11)$$

Expanding $\beta = \frac{\omega}{c}\mu_e$ in terms of ω_{th} and n_{th} , and in a fashion similar to (3.2.9) yields:

$$\beta = \frac{\omega_{th}}{c} \left(\mu_e(\nu_{th}, n_{th}) + \frac{\partial\mu_e}{\partial n}(n - n_{th}) + \frac{\bar{\mu}_e}{\omega_{th}}(\omega - \omega_{th}) \right) \quad (3.2.12)$$

The parameters: g , α_s , r_1 , and r_2 are frequency independent parameters. Substituting with (3.2.12) in (3.2.11), the round trip gain, G , can be written in terms of two different

terms: Firstly, frequency independent term G_1 :

$$G_1 = \sqrt{R_1 R_2} \exp([g - \alpha_s]L) \exp\left(-j \left[(2\omega_{th}L/c) \frac{\partial \mu_e}{\partial n} (n - n_{th}) \right]\right) \quad (3.2.13)$$

and secondly frequency dependent term G_2 :

$$G_2 = \exp\left(-\frac{2j\omega_{th}L}{c} \left[\mu_e(\nu_{th}, n_{th}) + \frac{\bar{\mu}_e}{\omega_{th}} (\omega - \omega_{th}) \right]\right). \quad (3.2.14)$$

The electric field within the laser cavity is characterized by the complex amplitude $E(t)$:

$$E(t) = \sqrt{P(t)} \exp(j\phi(t)) \quad (3.2.15)$$

and the actual electrical field is given by $Re(E(t) \exp(j\omega_{th}t))$, where $P(t)$ is the photon number, and $\phi(t)$ is the phase of the slowly varying amplitude of the forward traveling wave in the laser cavity. Neglecting the spontaneous emission term, the time evolution of electric field, $E(t)$, can be written as:

$$E(t) = G_1 E(t - \tau_L). \quad (3.2.16)$$

As $E(t)$ is a slowly varying field amplitude, then the variations during the round trip delay, τ_L , will be small, yielding:

$$E(t - \tau_L) = E(t) - \tau_L \frac{dE(t)}{dt} \quad (3.2.17)$$

and then

$$\frac{dE(t)}{dt} = \frac{1}{\tau_L} (1 - 1/G_1) E(t). \quad (3.2.18)$$

To achieve the lasing condition the round trip gain should be close to unity, so that the exponential expression in (3.2.13) gives:

$$\frac{1}{G_1} \approx 1 + \frac{1}{2} \ln(1/R_1 R_2) - gL + \alpha_s L + j[(2\omega_{th}L/c) \frac{\partial \mu_e}{\partial n} (n - n_{th})]. \quad (3.2.19)$$

Substituting with (3.2.19) in (3.2.18) gives:

$$\frac{dE(t)}{dt} = \left(j \frac{(2\omega_{th}L/c) \frac{\partial \mu_e}{\partial n} (n - n_{th})}{\tau_L} + \frac{gL}{\tau_L} - \frac{\alpha_s L + (1/2) \ln(1/R_1 R_2)}{\tau_L} \right) E(t). \quad (3.2.20)$$

The group velocity of an optical wave is given by $v_g = c/\bar{\mu}_e = 2L/\tau_L$, and using (3.2.10) yields $(2\omega_{th}L/c)\frac{\partial\bar{\mu}_e}{\partial n}(n - n_{th})/\tau_L = 2\pi(\nu - \nu_{th}) = \omega - \omega_{th}$, with ω representing the actual resonance frequency of the laser cavity. Including the feedback term yields:

$$\frac{dE(t)}{dt} = \left(j(\omega - \omega_{th}) + \frac{1}{2} \left[g\left(\frac{c}{\bar{\mu}_e}\right) - \frac{1}{\tau_{ph}} \right] \right) E(t) + \frac{1}{\tau_L} \kappa_{ext} E(t - \tau_{ext}) \exp(-j\omega_{th}\tau_{ext}). \quad (3.2.21)$$

where τ_{ph} is the photon lifetime of the solitary laser and is defined by:

$$\frac{1}{\tau_{ph}} = (c/\bar{\mu}_e) \left(\alpha_s + \frac{1}{2L} \ln\left(\frac{1}{R_1 R_2}\right) \right) \quad (3.2.22)$$

Using (3.2.7) the photon lifetime τ_{ph} can be written as:

$$\tau_{ph} = \frac{\tau_L}{2Lg_{th}}. \quad (3.2.23)$$

For $\frac{dP}{dt} = 2\text{Re}(E^*(t)\frac{dE}{dt})$ and $\frac{d\phi}{dt} = \text{Im}(E^*(t)\frac{dE}{dt})/P(t)$, (3.2.15) yields:

$$\frac{2}{\tau_L} \kappa_{ext} \sqrt{P(t)P(t - \tau_{ext})} \cos(\omega_{th}\tau_{ext} + \phi(t) - \phi(t - \tau_{ext})) \quad (3.2.24)$$

for the photon rate equation feedback term and

$$-\frac{1}{\tau_L} \kappa_{ext} \frac{\sqrt{P(t - \tau_{ext})}}{\sqrt{P(t)}} \cdot \sin(\omega_{th}\tau_{ext} + \phi(t) - \phi(t - \tau_{ext})) \quad (3.2.25)$$

for the phase rate equation feedback term.

3.2.2 Feedback Term Normalization and the Proposed Rate Equations

The normalization techniques enhance the convergence of the numerical solvers and make them suitable for transient, small signal, and large signal analysis. Applying the normalization methodology introduced by Ghoniemy et al [19] on the unnormalized photon rate equation feedback term given by (3.2.24) yields:

$$\frac{2}{\tau_L} \kappa_{ext} \sqrt{P(t)P(t - \tau_{ext})} \cos(\omega_{th}\tau_{ext} + \phi(t) - \phi(t - \tau_{ext})) \cdot \frac{\tau_e}{\Gamma C_{th}}. \quad (3.2.26)$$

For simplification, we will neglect the time delay of the reflected waves in the feedback term for the moment. Including the above normalized feedback term in the normalized photon rate equations (which include gain saturation, spectral hole burning, carrier transport, and gain nonlinearities effects) yields:

$$\frac{dP_n(t)}{dt} = \frac{(C_n(t) - C_{tr}^n)}{\tau_{ph}(1 - C_{tr}^n)} \frac{P_n(t)}{\sqrt{1 + P_r^n}} - \frac{P_n(t)}{\tau_{ph}} + \beta_{sp}C_n(t) + \frac{2}{\tau_L}\kappa_{ext}P_n(t)\cos(\omega_{th}\tau_{ext}) \quad (3.2.27)$$

and

$$\frac{dC_n(t)}{dt} = \frac{I(t)}{qV_cC_{th}} - \frac{(C_n(t) - C_{tr}^n)}{\tau_e\tau_{ph}(1 - C_{tr}^n)} \frac{P_n(t)}{\sqrt{1 + P_r^n}} - \frac{C_n(t)}{\tau_e} \quad (3.2.28)$$

where $P_n(t)$ is the normalized photon density, $C_n(t)$ is the normalized carrier density, τ_{ph} is the photon lifetime, ω_{th} is the angular resonance frequency for $n = n_{th}$, n_{th} is the carrier density at the lasing threshold, C_{tr} is the threshold carrier density, τ_e is the electron lifetime, β_{sp} is the spontaneous emission factor, and q is the electronic charge, and V_c is the volume of the active region.

The above rate equations describe the laser diode's characteristics in coupled cavity. Numerical solution methods are required to solve these equations due to their extensive nonlinearity.

3.3 Model Implementation

3.3.1 Symbolically Defined Laser Diode Models Including Feedback Term

Agilent ADS design software was used to implement the laser model based on the augmented rate equations. DC, transient, and harmonic balance simulation tools were used to analyze the laser performance. The time-domain and frequency domain simulation capabilities of the Agilent ADS software makes it a good candidate for the proposed laser mode implementation. In particular, a "rapid model prototyping" component in ADS referred to as "Symbolically Defined Device" (SDD) makes the software well-suited for exploratory work in laser model development. ADS can cover all aspect of communications system design from circuit level to system level simulation and from analog to digital systems design. Moreover, it is a suitable environment to integrate the laser model with the

other components in the system, these include laser driving circuits and laser pre-distorter models.

A SDD describes a set of equations in terms of port currents and port voltages and automatically generates the derivatives and load information. SDDs automatically determine the relationship between equations. A SDD is represented in the circuit schematic as an n -port device, with up to 10 ports. The equations that specify the voltage and current of a port are defined as functions of other voltages and currents.

The n -port SDD is described by n equations, called constitutive relationships, that relate the n port currents and the n port voltages. The constitutive relationships may be specified in either explicit or implicit representations. For the explicit representation, the current at port k is specified as a function of port voltages, $i_k = f(v_1, v_2, \dots, v_n)$, and is written as I[a,b], where a is the port number, and b indicates the order of the derivatives (e.g. 1 means 1st derivative). The implicit representation uses an implicit relationship between any of the port currents and any of the port voltages, $f_k = f(v_1, v_2, \dots, i_n, i_1, i_2, \dots, i_n)$, and is written as F[a,b].

A 4-port SDD, shown in Figure 3.1 on the following page, was used to implement the augmented rate equations as a combination of implicit and explicit part relationships. The drive current is represented by the current flowing into Port 1 of the SDD and is defined by the explicit function I[1,0]. P_n is represented by the current flowing into Port 2 of the SDD and is defined by the implicit function F[2,0]. Similarly, C_n is represented by the current flowing into Port 3 of the SDD and is defined by the implicit function F[3,0]. The derivative, $P'_n(t)$, is related to the current flowing out of Port 2 of the SDD by the explicit relation F[2,1]. The derivative $C'_n(t)$ is related to the current flowing out of Port 3 of the SDD by the explicit relation F[3,1]. The introduced feedback term is represented by port 4 of the SDD. The current-controlled voltage source shown by the schematic diagram in Figure 3.1 on the next page is used to de-normalize the normalized photon density into the actual intracavity photon density. This is accomplished by dividing the photons number by the normalization factor.

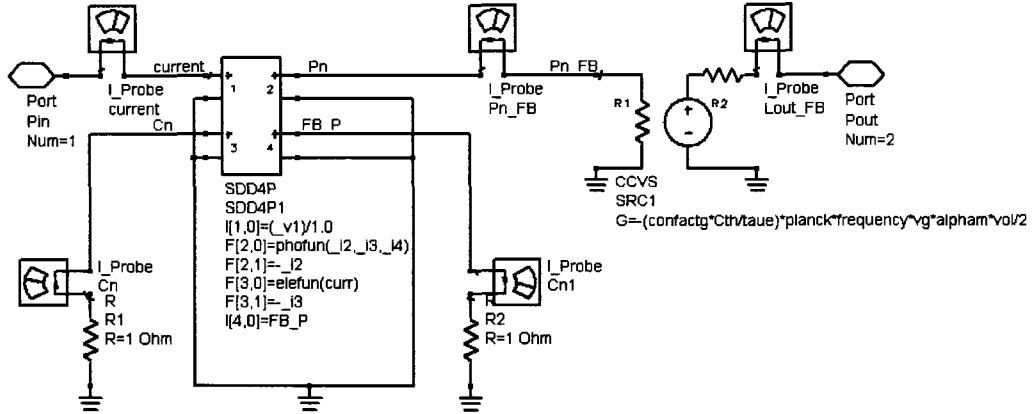


Figure 3.1: 4-port SDD laser model with external feedback. The drive current is represented by the current flowing into Port 1. P_n is represented by the current flowing into Port 2. C_n is represented by the current flowing into Port 3. The introduced feedback term is represented by port 4 of the SDD.

3.3.2 Parameters Extraction

The simulations are carried out with the parameters given in Table 3.1 on the following page. These parameters were obtained using the parameter extraction algorithm presented in [19], in which the DC and frequency response measurements data for a DFB laser diode were acquired from an optical multimeter, an optical spectrum analyzer, and a lightwave signal analyzer. The acquired data together with the laser's data sheet parameters, and the other given parameters for both laser and external cavities were used in the different mathematical relations to extract the laser diode parameters. These parameters are used in the laser rate equations that are represented by the ADS laser model in order to perform the DC, time domain, and frequency domain simulations.

3.4 Simulation Results

3.4.1 Simulation of Laser Performance changes due to Feedback

Due to the optical back-reflections the required threshold gain of the laser is changed, it can be reduced or increased depending on the phase of the reflected light, ϕ_L . Slight changes in ϕ_L or the optical frequency, ν , can result in considerable lasing threshold gain,

Table 3.1: Laser parameters

Symbol	Parameter name	value
L	Laser cavity length	$250 \mu m$
B_o	Radiative recombination coefficient	$1 \times 10^{-16} m^3 s^{-1}$
W	Laser cavity width	$2 \mu m$
C_a	Auger recombination coefficient	$3 \times 10^{-41} m^6 s^{-1}$
d	Laser cavity thickness	$0.2 \mu m$
d_m	Dipole moment	$9 \times 10^{-29} m.C$
n_g	Group refractive index	4
τ_{in}	Dipole relaxation time	$0.1 \times 10^{-12} s$
σ	Medium conductivity	$37.2 \Omega^{-1} m^{-1}$
τ_c	Electrons intraband relaxation time	$0.3 \times 10^{-12} s$
\bar{n}	Effective mode index	3.5
τ_ν	Holes intraband relaxation time	$0.07 \times 10^{-12} s$
Γ	Mode confinement factor	0.3
β_{sp}	Spontaneous emission factor	1×10^{-4}
\wp	Differential gain coefficient	$2.5 \times 10^{-20} m^2$
L_{ext}	External cavity length	$1.5 m$
C_{tro}	Transparency carrier density	$1 \times 10^{24} m^{-3}$
r_{2ext}	External cavity reflectivity	0.20
A_{nr}	Nonradiative recombination coefficient	$1 \times 10^8 s^{-1}$
η	Coupling coefficient	0.75

g_c , changes. FP lasers may suffer from mode hopping noise which can be avoided for single mode DFB lasers. However, for DFB lasers the external cavity may introduce additional external cavity modes, causing possible mode hopping. The optical feedback phenomenon is described by the three parameters K_{ext} , C, and X given by (2.6.6 on page 18) , (2.6.8 on page 18), and (2.6.9 on page 18) respectively. The following results show how the laser diode performance can be affected by those three parameters.

Possible emission frequencies

Possible modes of the laser with feedback are characterized by the threshold gain and phase condition, requiring a round trip phase change $\Delta\phi_L = 0$, or multiples of 2π . Figure 3.2 is simulation results showing the relationship between round trip phase change and optical frequency when there is no feedback ($r_{2ext} = 0$), weak feedback ($r_{2ext} = 0.005$), and relatively strong feedback ($r_{2ext} = 0.025$). The other laser parameters are: 1310 nm wavelength, 250 μm cavity length, 1 m external cavity length, and 0.05 laser exit facet reflectivity. With no feedback, $\Delta\phi_L$ varies linearly with the optical frequency, yielding a single zero at the solitary laser frequency, ν_{th} . For weak feedback, $\Delta\phi_L$ monotonically increase with optical frequency yielding a single zero for $\Delta\phi_L$, hence still resulting in a single emission frequency. For relatively strong feedback, $\Delta\phi_L$ undergoes strong oscillations yielding multiple zeros for $\Delta\phi_L$; several external cavity modes around the solitary laser may also oscillate.

Maximum oscillation frequency shift due to feedback

The maximum feedback induced lasing frequency shift depends on the feedback parameter, C. For small values of C, that is weak feedback, $\Delta\phi_L$ and the optical frequency, ν , are monotonic functions yielding no additional modes due to the optical feedback. Figure 3.3 shows the simulated maximum oscillation frequency shift due to feedback versus laser cavity length for 1310 nm wavelength, 0.025 external reflectivity r_{2ext} , and 0.05 laser exit facet reflectivity r_{2s} . Results show that the maximum frequency shift is a decreasing function of laser cavity length. For a cavity length of 150 μm , the emission frequency shifts by 101.2 GHZ, this is equivalent to 0.5789 nm emission wavelength shift at wavelength of 1310 nm.

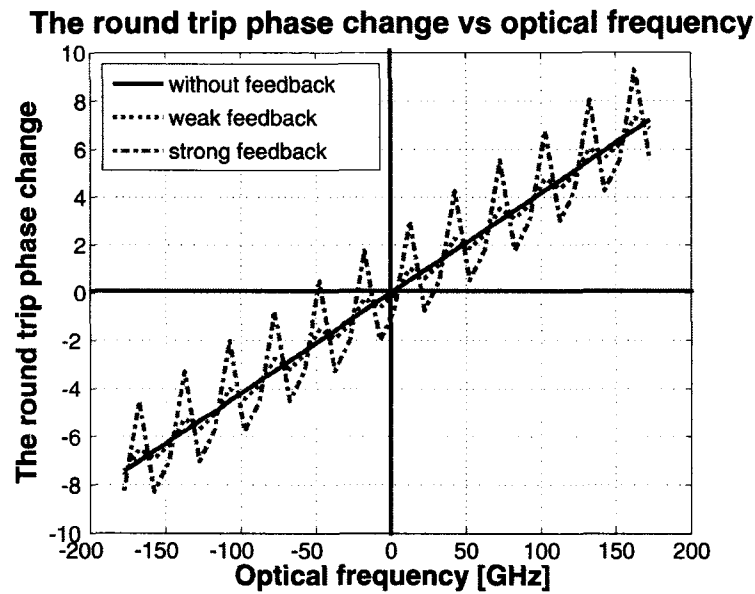


Figure 3.2: Simulated round trip phase change versus the optical frequency with no feedback ($r_{2ext} = 0$), weak feedback ($r_{2ext} = 0.005$), and relatively strong feedback ($r_{2ext} = 0.025$).

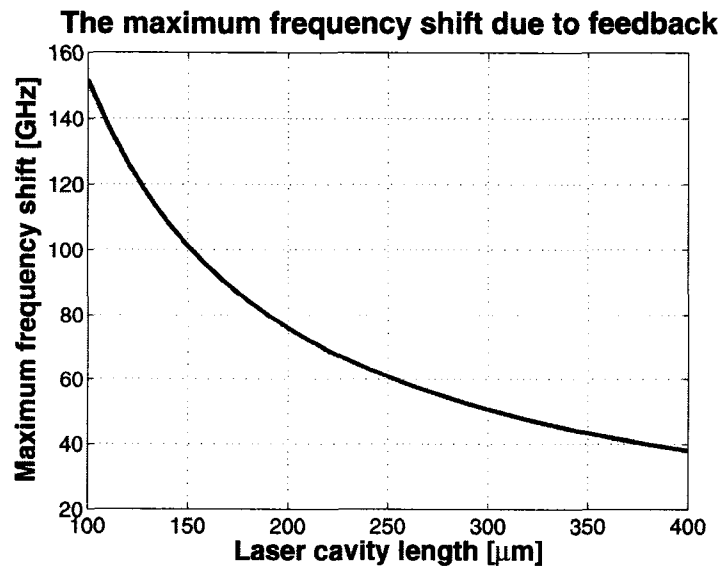


Figure 3.3: Simulated maximum oscillation frequency shift due to feedback versus laser cavity length for 1310 nm wavelength, 0.025 external reflectivity, and 0.05 laser exit facet reflectivity.

Simulation results also show that the emission frequency shift is a decreasing function of the laser exit facet reflectivity, r_{2s} , as depicted in Figure 3.4 for 1310 nm wavelength, 1 m external cavity length, and 0.1 external reflectivity r_{2ext} .

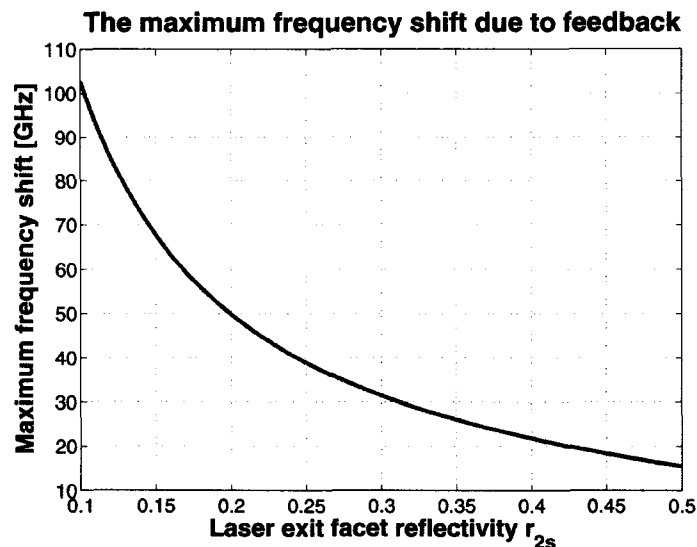


Figure 3.4: Simulated maximum frequency shift versus laser exit facet reflectivity for 1310 nm wavelength, 1 m external cavity length, and 0.1 external reflectivity.

The emission frequency shift is an increasing function of the external reflectivity, r_{2ext} , as shown in Figure 3.5 on the next page for cavity length of $350 \mu m$, laser exit facet reflectivity r_{2s} of 0.32 and the same other mentioned parameters.

Spectral linewidth change due to feedback

As long as the optical back-reflections are limited to weak levels with $C < 1$, the external optical feedback introduces no additional external cavity modes. Moreover depending on the phase of the reflected power, the optical feedback may improve the laser linewidth. Figure 3.6 on the following page shows the ratio of simulated spectral linewidth with feedback, $\Delta\nu$, to the spectral linewidth without feedback, $\Delta\nu_0$, with the feedback phase adjusted for minimum linewidth. The result shows that for a cavity length of $250 \mu m$, wavelength of 1310 nm, external cavity length of 1 m, and laser exit facet reflectivity of 0.05, an improvement of $\Delta\nu/\Delta\nu_0 = 0.51$ can be achieved with $C=0.4$.

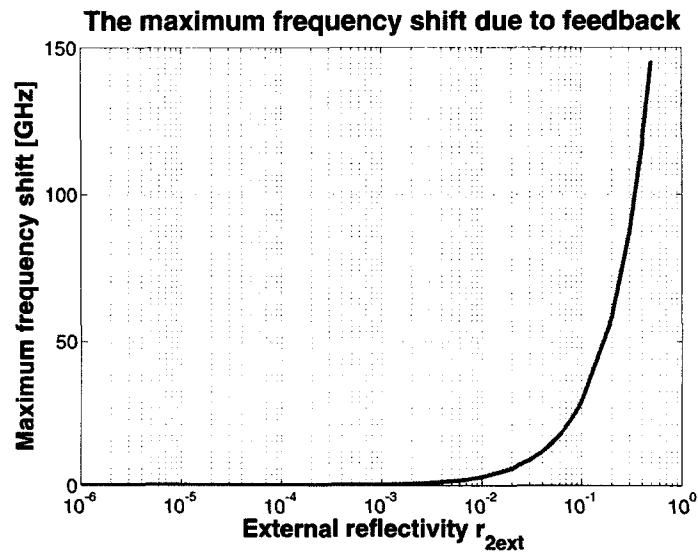


Figure 3.5: Simulated maximum oscillation frequency shift versus external reflectivity for cavity length of $350 \mu m$, 1 m external cavity length, laser exit facet reflectivity of 0.32.

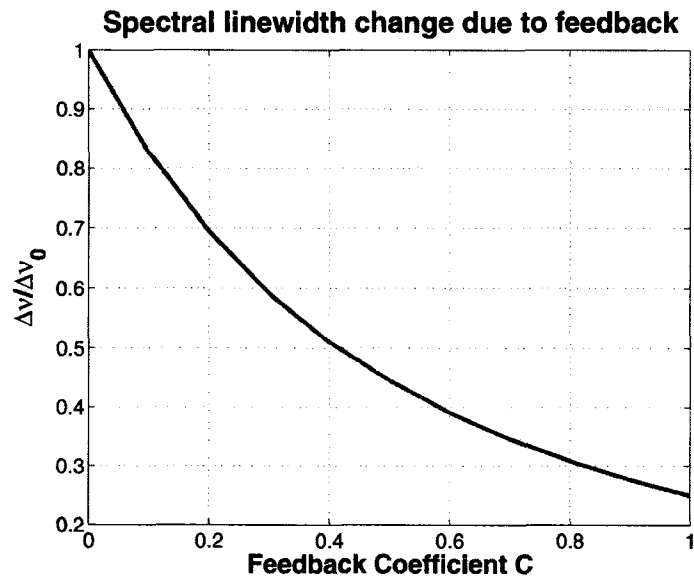


Figure 3.6: Simulated spectral linewidth with weak feedback for 1 m external cavity length, and 0.05 laser exit facet reflectivity; feedback phase is adjusted for minimum linewidth.

3.4.2 DC Simulation

A threshold current value, I_{th} , is required for the laser to build up a threshold gain and to start lasing. Below this threshold point, the laser emits a spontaneous radiation and acts like a light-emitting diode.

In this section the proposed model is used to predict the relationship between optical output power and diode drive current for two cases, that is with and without feedback effect. The model is used also to examine the effect of feedback on the laser diode threshold level.

A swept-parameter DC simulation was used to simulate the DC behavior of the DFB laser diode, both with and without feedback as shown in Figure 3.7 on the next page. The bias current was swept from near DC to 100 mA, and the external reflectivity, r_{2ext} , was swept from 0.1 to 1 in 0.1 step.

The DC simulation results show that as the feedback level increases, the laser threshold current decreases as demonstrated in the optical output power versus current curve given in Figure 3.8 on page 49 [53]. Laser threshold levels at different external reflectivity values were extracted from Figure 3.8 on page 49 and plotted in Figure 3.9 on page 49. These results are confirmed through measurements as will be shown in Chapter 4.

3.4.3 DFB Laser Diode Frequency Response

The proposed model was used to simulate the dynamic behavior of the laser diode and to predict the laser modulation response, modulation bandwidth, and relaxation oscillation frequency. This was performed using the ADS harmonic balance simulation capabilities.

The laser model shown in Figure 3.1 on page 41 and represented by the diode symbol in Figure 3.10 on page 50 was directly modulated with an small input sinusoid signal. The input signal modulation frequency was ranging from 0.1 GHz to 15 GHz. The laser diode behavior was simulated both with and without the feedback effect to determine the impact of the feedback on the laser dynamic behavior. The external reflectivity was swept from 0.1 to 0.6 for a total of four levels and the external cavity length, L_{ext} , was set to 2 m.

Figure 3.11 on page 51 shows the simulated laser modulation response with and without feedback. Simulation results demonstrate that higher relaxation oscillation frequencies are obtained at higher feedback levels. An enhancement of 200 MHz can be achieved with 0.6 external reflectivity located at 2 m apart from the laser exit facet.

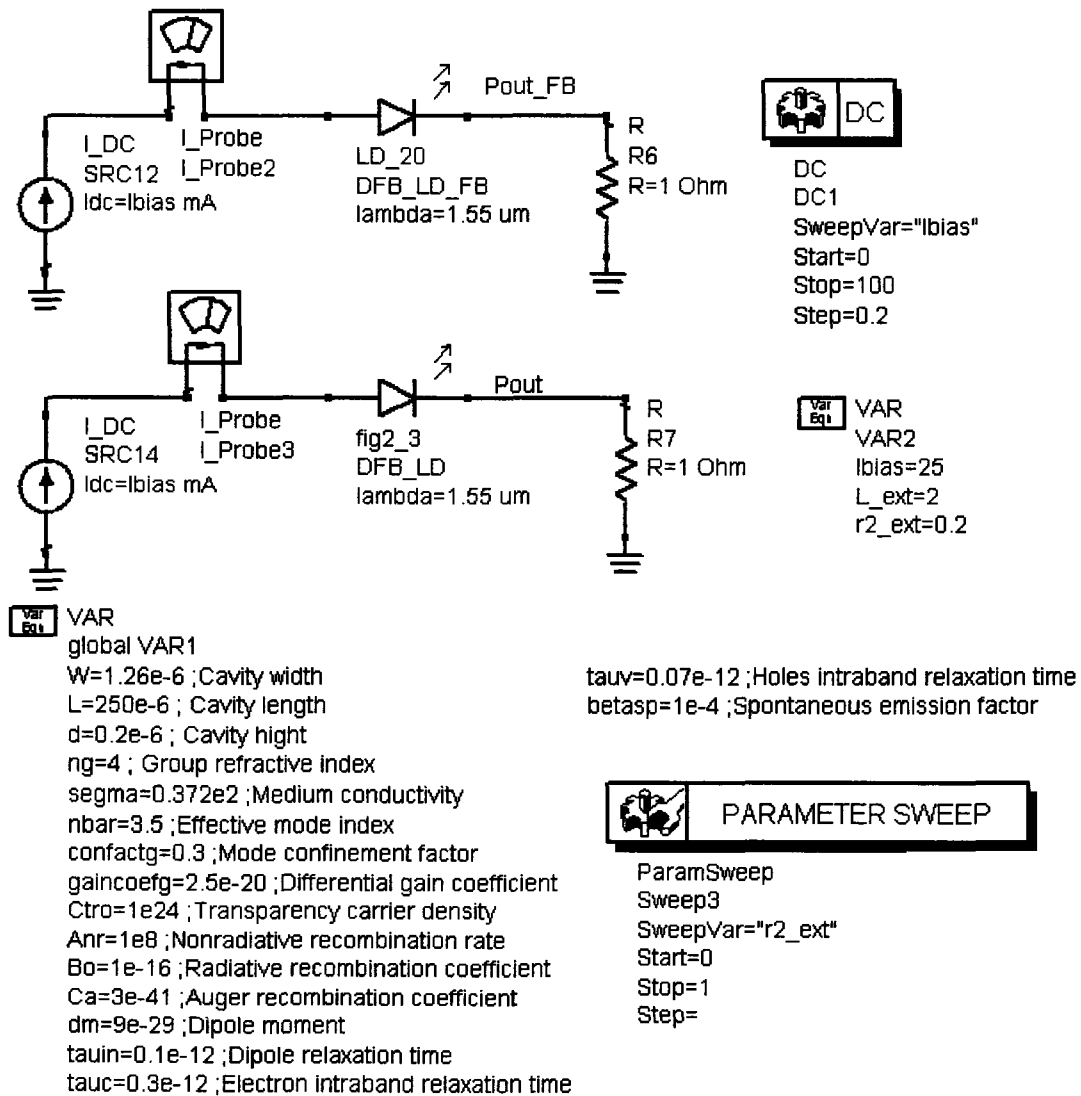


Figure 3.7: Agilent-ADS schematic diagram for the swept-parameter DC simulation setup for laser model with and without feedback.

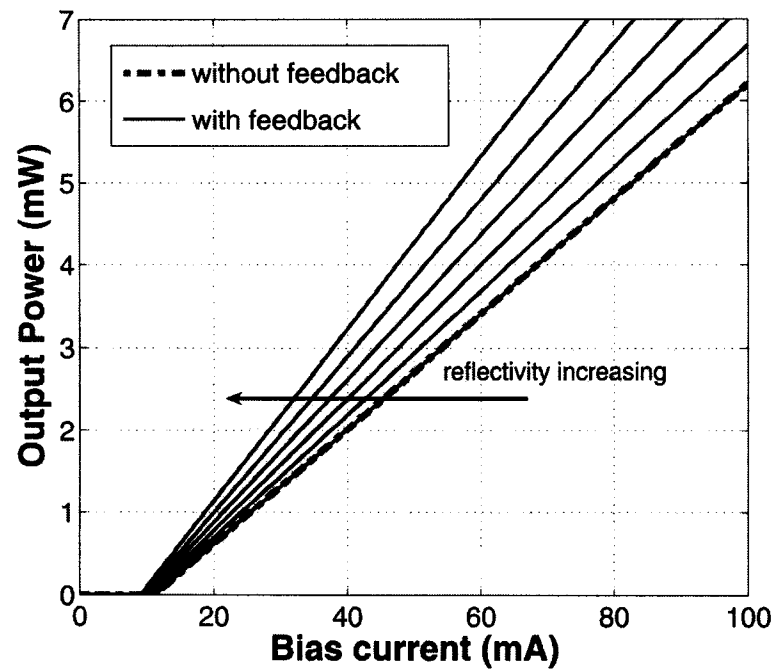


Figure 3.8: Simulated threshold current change due to back-reflection, r_{2ext} ranges from 0.1 to 1 in 0.1 step, and $L_{ext} = 1.5$ m.

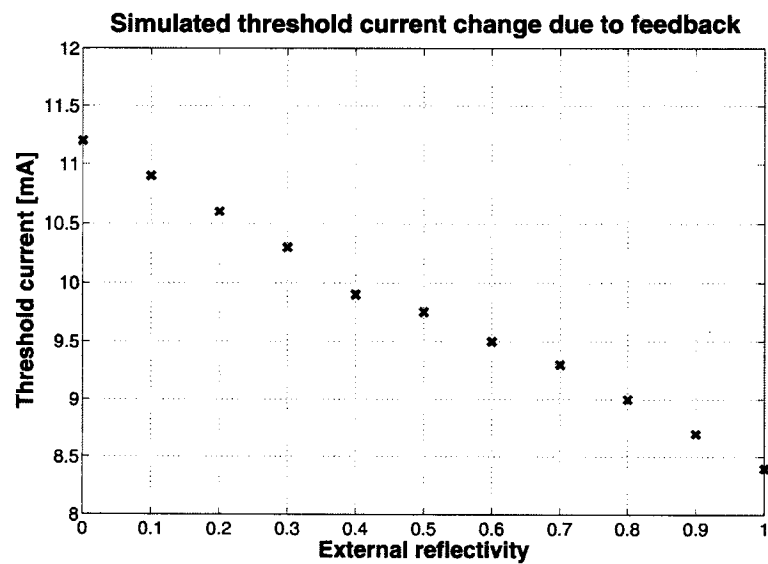


Figure 3.9: Simulated threshold current levels at different external reflectivity r_{2ext} .

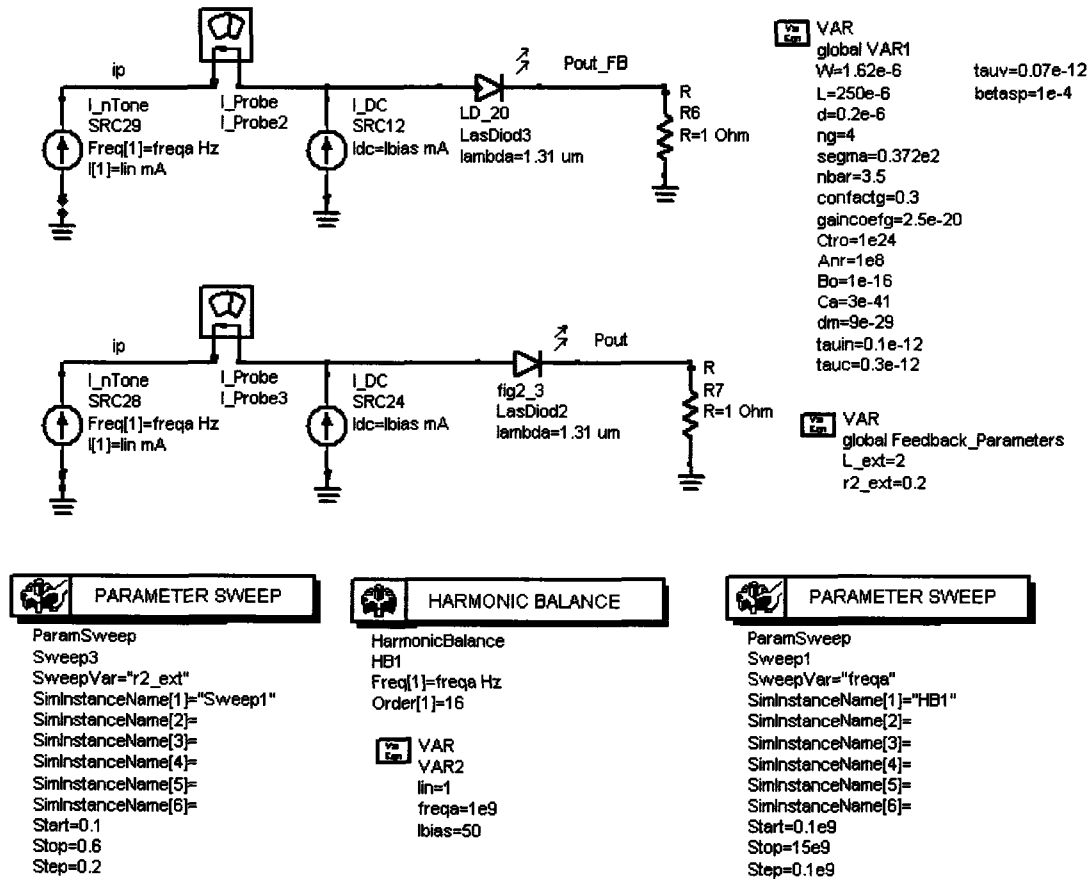


Figure 3.10: Harmonic balance (HB) simulation setup for the laser model with and without external feedback.

3.4.4 DFB Laser Diode Distortion

Due to the importance of the laser linearity in designing optical transmitters for CATV applications, and since the dynamic range of the directly modulated lasers is mainly limited by the laser distortion levels, accurate simulations for the laser nonlinear distortions are required. The proposed model was used in the ADS HB simulation setup shown in Figure 3.12 on page 52 to simulate the laser diode distortion for both cases, that is, with and without feedback.

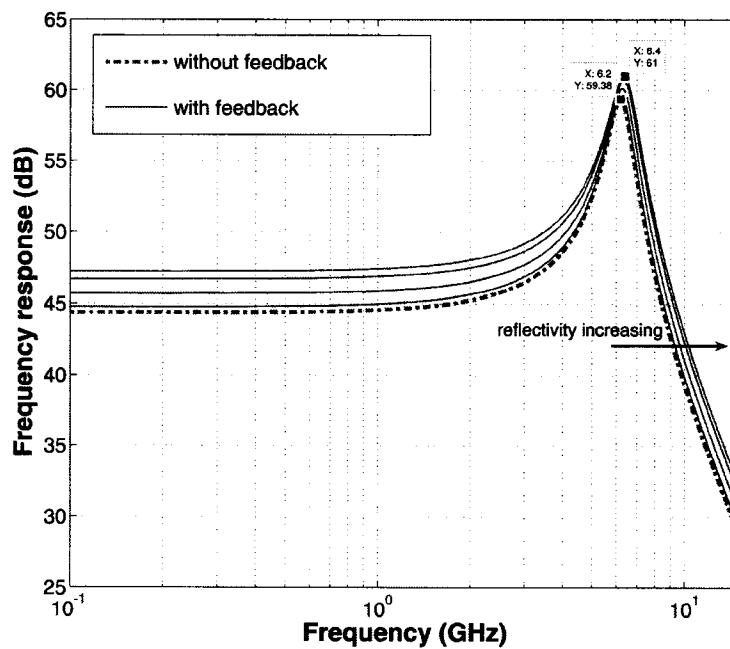


Figure 3.11: Modulation frequency response for the laser diode with and without feedback, r_{2ext} swept from 0.1 to 0.6 for a total of four levels, and $L_{ext} = 2 m$.

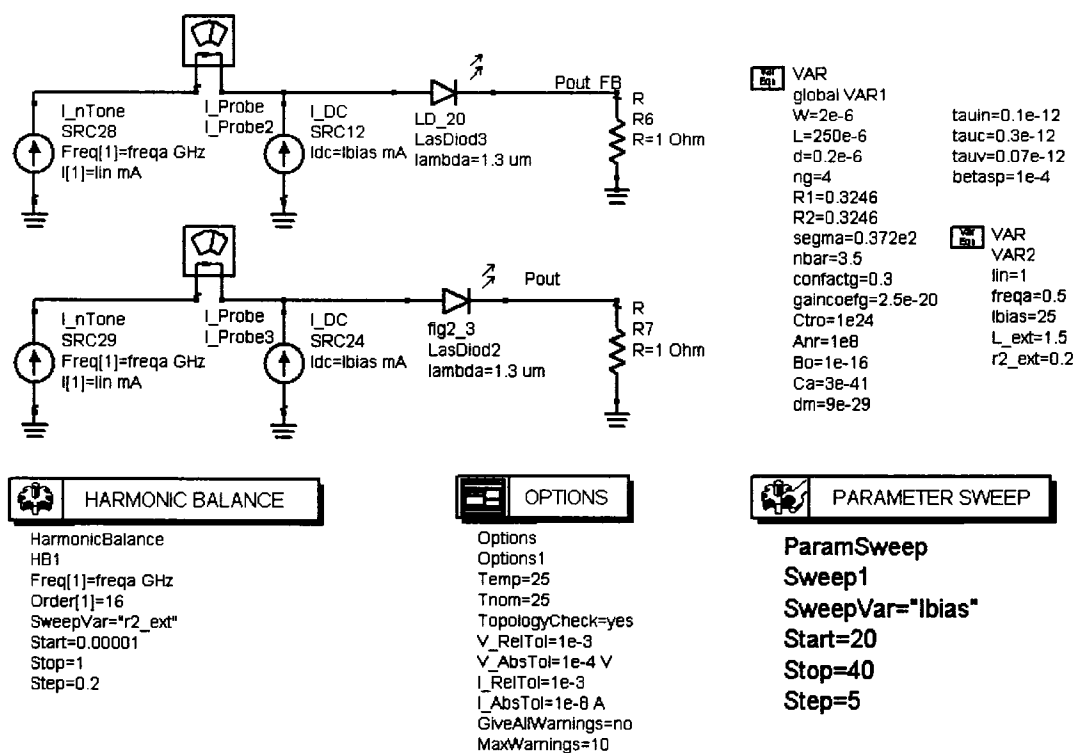


Figure 3.12: Distortion simulation setup for the laser diode with and without feedback.

Figures 3.13 and 3.14 on the following page show the simulated second and third order harmonic distortions ($2^{nd}HD$ and $3^{rd}HD$) normalized to the fundamental power versus external reflectivity, r_{2ext} , for different bias current levels respectively. The bias current was swept from 25 to 35 mA for a total of three levels, and the external reflectivity was swept from 0 to 1. The other simulation parameters were: modulation frequency $f=500$ MHz, modulation signal input current $I_{in} = 1$ mA, and external cavity length $L_{ext} = 1.5$ m.

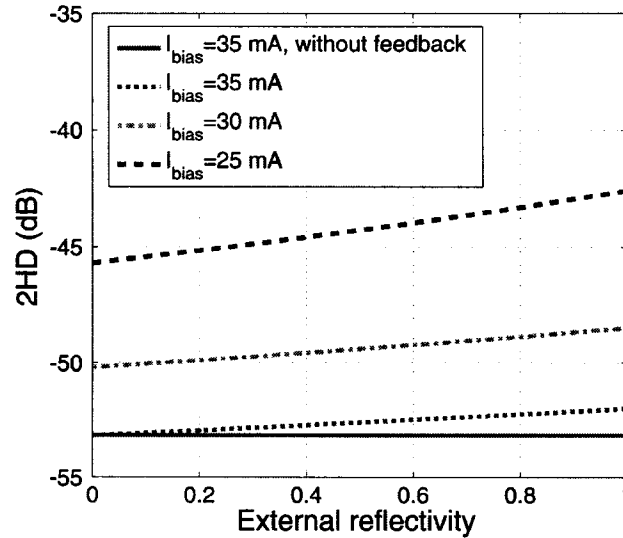


Figure 3.13: Simulated second harmonic distortion vs. external reflectivity for different bias current levels and the following parameters: $f = 500$ MHz, $I_{in} = 1$ mA, and $L_{ext} = 1.5$ m.

AS the results show that the $2^{nd}HD$ and the $3^{rd}HD$ are increasing functions of r_{2ext} and are decreasing functions of I_{bias} . The simulated $2^{nd}HD$ and $3^{rd}HD$ without feedback at I_{bias} of 35 mA were included in the figures for comparison, an increase of less than 3 dB is observed due to feedback at this bias current level for both $2^{nd}HD$ and $3^{rd}HD$.

Figures 3.15 on the next page and 3.16 on page 55 show the simulated $2^{nd}HD$ and $3^{rd}HD$ normalized to the fundamental power versus I_{bias} for different r_{2ext} levels respectively. The bias current was swept from 20 to 40 mA, and the external reflectivity was swept from 10^{-5} to 0.4 for a total of three levels. The other simulation parameters were: modulation frequency $f=500$ MHz, modulation signal input current $I_{in} = 1$ mA, and external cavity length $L_{ext} = 1.5$ m.

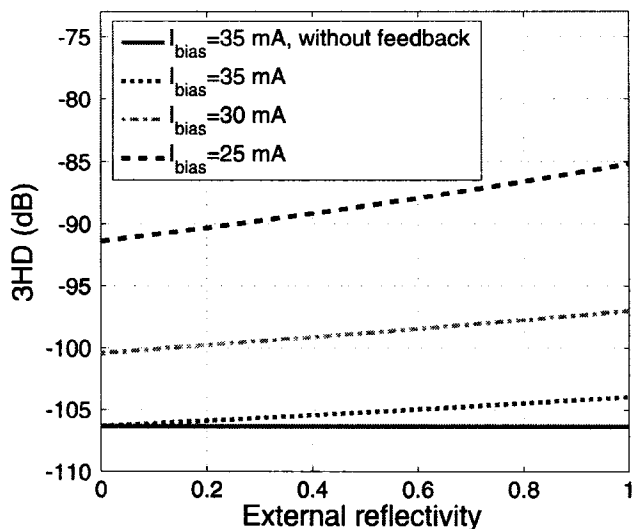


Figure 3.14: Simulated third harmonic distortion vs. external reflectivity for different bias current levels and the following parameters: $f = 500$ MHz, $I_{in} = 1$ mA, and $L_{ext} = 1.5$ m.

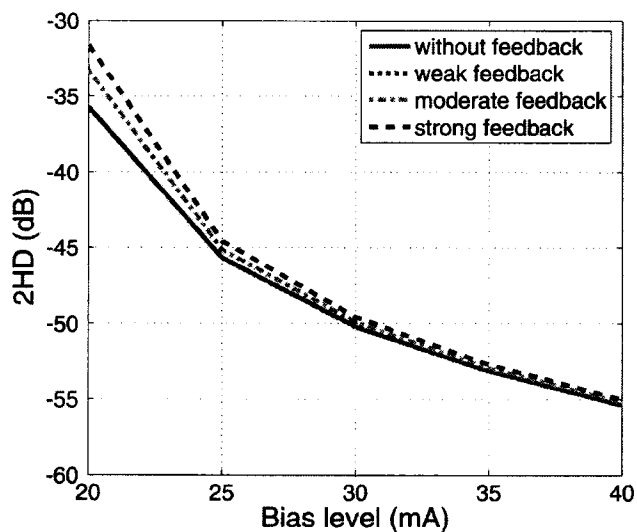


Figure 3.15: Simulated second harmonic distortion vs. bias current for different external reflectivity levels and the following parameters: $f = 500$ MHz, $I_{in} = 1$ mA, and $L_{ext} = 1.5$ m.

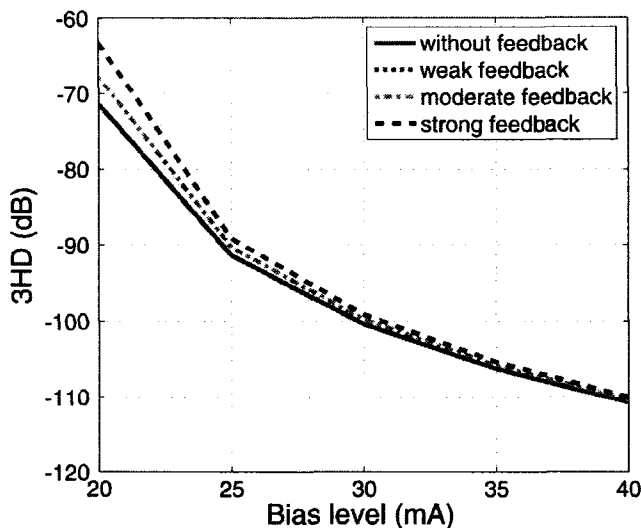


Figure 3.16: Simulated third harmonic distortion vs. bias current for different external reflectivity levels and the following parameters: $f = 500 \text{ MHz}$, $I_{in} = 1 \text{ mA}$, and $L_{ext} = 1.5 \text{ m}$.

The results demonstrate that the $2^{nd}HD$ and the $3^{rd}HD$ are increasing functions of r_{2ext} and are decreasing functions of I_{bias} . The simulated $2^{nd}HD$ and $3^{rd}HD$ without feedback coincide with that of 10^{-5} external reflectivity due to the very weak reflections.

3.5 Laser Model Including Feedback and Noise terms

The model capability is improved by adding the phase rate equation and including the noise terms together with the feedback terms. This will allow the model to simulate the laser diode RIN under different feedback powers.

The stochastic differential equations (3.5.1) - (3.5.3) completely define the laser system. An exact solution to those equations seems impossible; an approximation and/or numerical simulation was implemented instead.

$$\begin{aligned}
\frac{dP_n(T, t)}{dt} = & \frac{(C_n(T, t) - C_{tr}^n(T))}{\tau_{ph}(T)(1 - C_{tr}^n(T))} \frac{P_n(T, t)}{\sqrt{1 + P_r^n(T, t)}} - \frac{P_n(T, t)}{\tau_{ph}(T)} \\
& + (\beta_{sp} B_o \tau_e(T) C_{tho} \exp(\frac{T - T_r}{T_o} - \frac{E_1 q}{K_B T})) C_n^2(T, t) + F_{P_n}(t) \\
& + \frac{2}{\tau_L} \kappa_{ext} \sqrt{P_n(t) P_n(t - \tau_{ext})} \cos(\omega_{th} \tau_{ext} + C_{th} V (\phi_n(t) - \phi_n(t - \tau_{ext}))) \quad (3.5.1)
\end{aligned}$$

$$\begin{aligned}
\frac{dC_n(T, t)}{dt} = & \frac{I(t)}{q V_c C_{th}(T)} - \frac{(C_n(T, t) - C_{tr}^n(T))}{\tau_e(T) \tau_{ph}(T) (1 - C_{tr}^n(T))} \frac{P_n(T, t)}{\sqrt{1 + P_r^n(T, t)}} - \frac{C_n(T, t)}{\tau_e(T)} + F_{C_n}(t) \quad (3.5.2)
\end{aligned}$$

$$\begin{aligned}
\frac{d\Phi_n(t)}{dt} = & \frac{\beta}{2} G_n(C_n(T, t) - \bar{C}_n) + F_{\Phi_n}(t) \\
& - \frac{1}{\tau_L} \kappa_{ext} \frac{1}{C_{th} V} \frac{\sqrt{P_n(t - \tau_{ext})}}{\sqrt{P_n(t)}} \cdot \sin(\omega_{th} \tau_{ext} + C_{th} V \cdot (\phi_n(t) - \phi_n(t - \tau_{ext}))) \quad (3.5.3)
\end{aligned}$$

where $F_{P_n}(t)$, $F_{C_n}(t)$, and $F_{\Phi_n}(t)$, are the normalized photon, carrier, and phase Langevin noise sources respectively.

The external power reflectivity (feedback fraction) f_{ext} is given by

$$f_{ext} = \eta^2 r_{2ext} \quad (3.5.4)$$

where η denotes the coupling efficiency between the laser and the external cavity.

The Langevin noise sources are generated using the technique presented in [17] and [19] as follows:

- Generation of three different Gaussian random variable $X1$, $X2$, and $X3$ with zero mean, $\langle X1 \rangle = \langle X2 \rangle = \langle X3 \rangle = 0$, and unity variances, $\langle X1^2 \rangle = \langle X2^2 \rangle = \langle X3^2 \rangle = 1$.
- Construction of Langevin photons, phase, and carrier operators as [17]:

$$F_P = \sqrt{\frac{V_{PP}}{\Delta t}} X1 \quad (3.5.5)$$

$$F_{\Phi} = \frac{1}{2(P+1)} \sqrt{\frac{V_{PP}}{\Delta t}} X3 \quad (3.5.6)$$

$$F_C = \sqrt{\frac{V_{CC} + 2kV_{PC}}{\Delta t}} X2 - kF_P - mF_{\Phi} \quad (3.5.7)$$

where Δt is the time interval between samples, V_{xy} is the variance (with x and y standing for any of P, C, or ϕ), the parameters k and m are defined as:

$$k = -\frac{V_{PC}}{V_{PP}} \quad (3.5.8)$$

$$m = -\frac{V_{C\Phi}}{V_{\Phi\Phi}} = 2k(P+1) \quad (3.5.9)$$

The new set of rate equations including feedback and noise terms are implemented in ADS as shown in Figure 3.17.

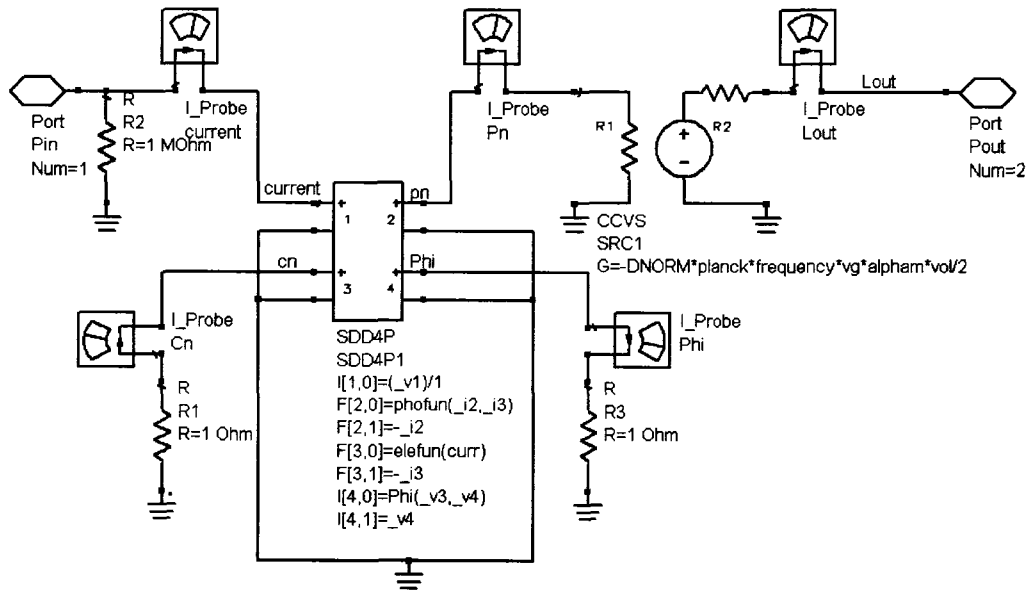


Figure 3.17: ADS laser model including feedback terms and noise operators.

The amplitude of the noise terms were adjusted in order to get the model to converge, our main concern was to examine the laser noise behavior at different feedback powers as well as to identify the noise peak around the relaxation oscillation rather than the accurate noise amplitude itself.

3.5.1 Relative Intensity Noise Calculation

The RIN is defined as the ratio of the mean-square optical intensity noise to the square of the average optical power, it can be calculated using:

$$RIN = \frac{\overline{(P(t) - \overline{P(t)})^2}}{\overline{P(t)}^2} \quad (3.5.10)$$

where $P(t)$ is the laser output power, and $\overline{P(t)}$ is the laser mean power.

3.5.2 Laser output

Figure 3.18 on the following page shows the time domain output, that is optical power versus time with and without the noise operators. The fluctuations of the output power around the steady state value after the transient time are contributed to the Langevin noise sources that have been added to the laser rate equations. The fluctuations are less visible during the transient time due to the relative level of the transient output and the noise.

3.5.3 Modulation Frequency Response Simulation

The laser model was used to predict the modulation frequency response, where the DFB laser model was directly modulated with an input signal frequency ranging from 100 MHz to 20 GHz with 0 dBm input signal power. Figure 3.19 on page 60 shows the simulated relaxation frequency at 6.7 GHz.

3.5.4 RIN Simulation

The RIN was calculated by taking an *FFT* of the steady state time domain data; the effect of the transients on the simulations was avoided by running the simulation beyond

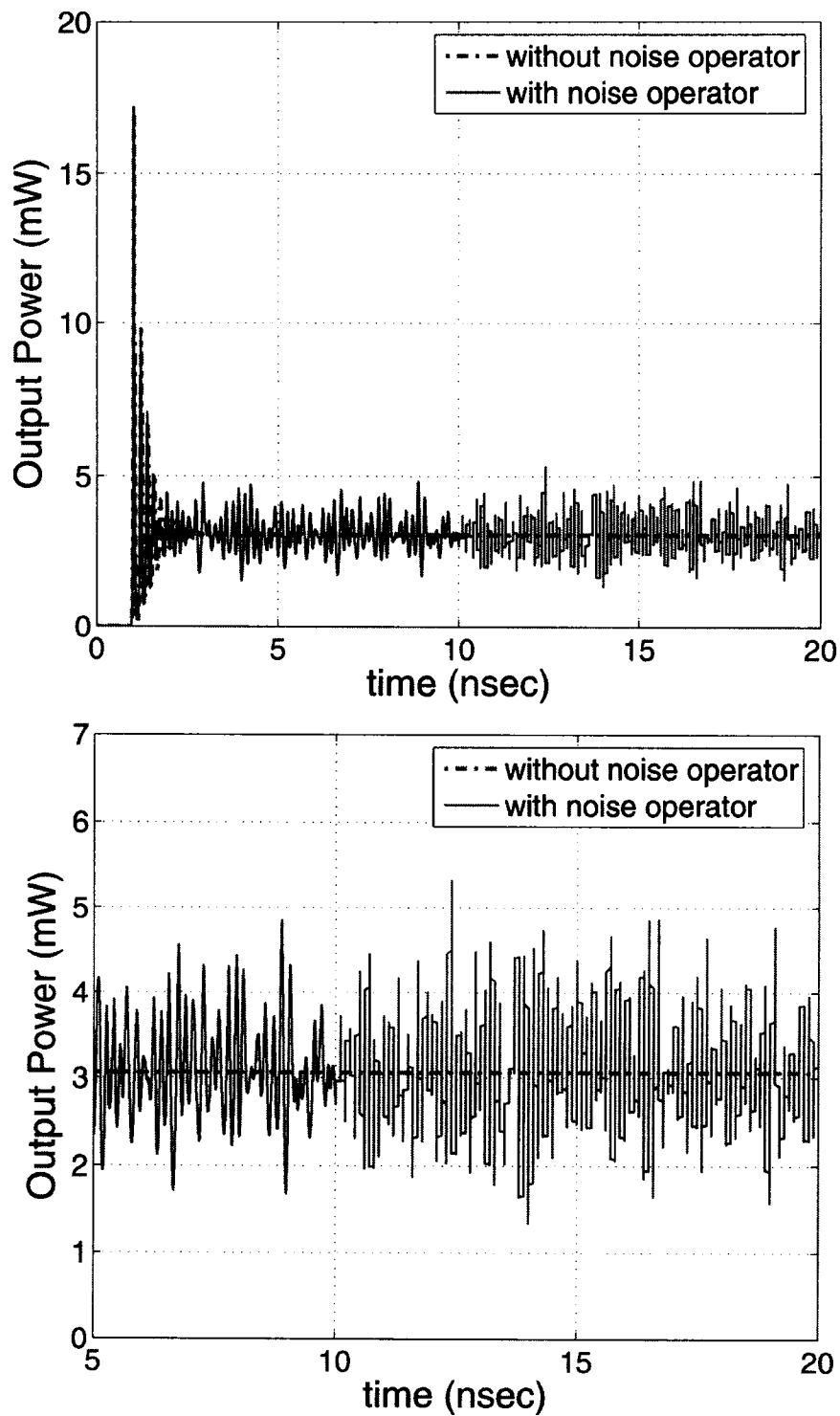


Figure 3.18: Time domain laser model's output with and without noise sources.

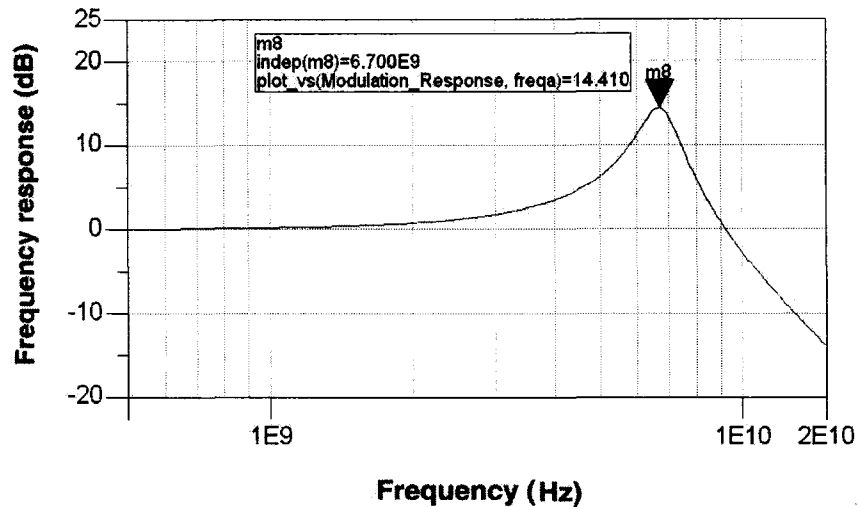


Figure 3.19: Simulated modulation frequency response .

25 *nsec*. A short time step of $\Delta t = 10$ *psec* was used to cover a frequency spectrum of up to 50 *GHz*. The simulation was extended to up to 250 *nsec* hence requiring around 22,500 integration steps. Figure 3.20 shows the simulated RIN for a DFB laser operating at the same condition as in Figure 3.19. As expected, the RIN exhibited a peak around the relaxation frequency that is 6.7 *GHz*.

RIN versus bias current for fixed unintended optical back-reflection

Figure 3.21 on the following page shows the simulated RIN as a function of the bias current I_{bias} ranging from 12 *mA* to 40 *mA* for a fixed feedback level of -45 *dB*. The result shows that the RIN decreases exponentially as the I_{bias} increases. This is in good agreement with the results previously presented in [12] and [17].

RIN versus external reflectivity

Figure 3.22 on page 62 shows the simulated RIN as a function of the external reflectivity, r_{2ex} , for a fixed bias current level of 15 *mA*. The RIN slightly increases as the external reflectivity increases until a certain feedback level is exceeded (-30 *dB* in this case). A dramatic increase in the RIN occurs beyond that point due to the transition to feedback Regime IV (coherence collapse regime). The simulation results are again in good agreement

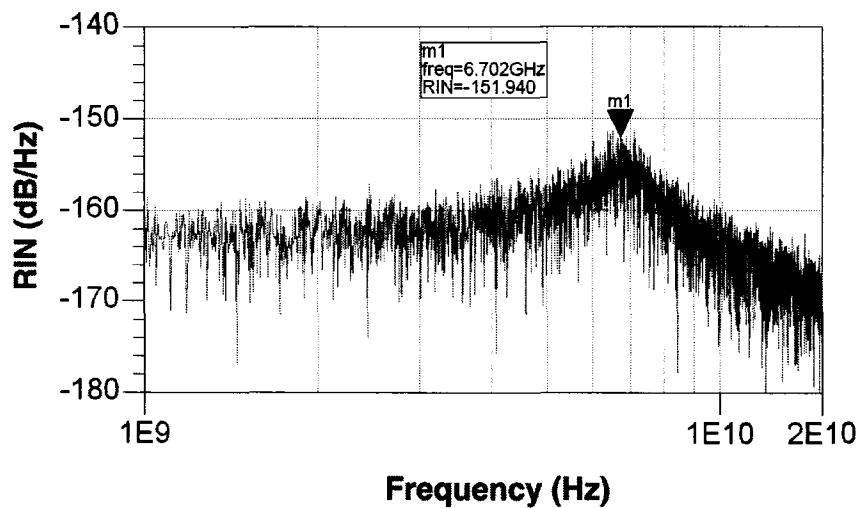


Figure 3.20: Simulated RIN of a DFB laser diode.

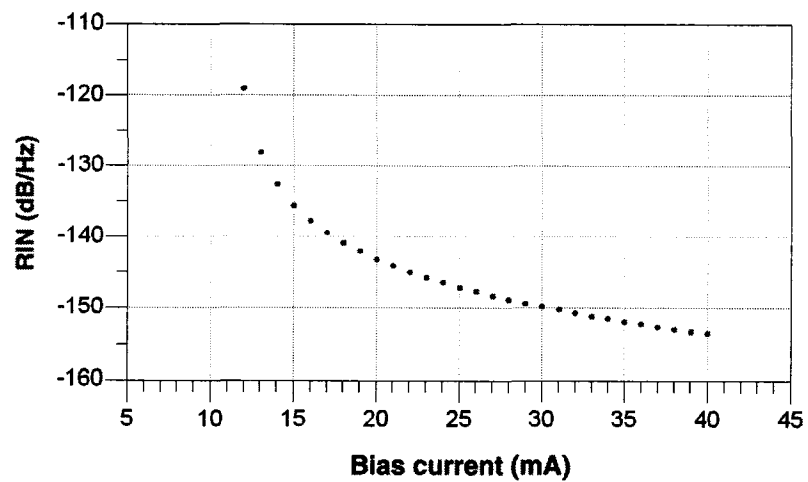


Figure 3.21: Simulated RIN as a function of bias current for a fixed feedback level of -45 dB.

with the results presented in [39] and [10].

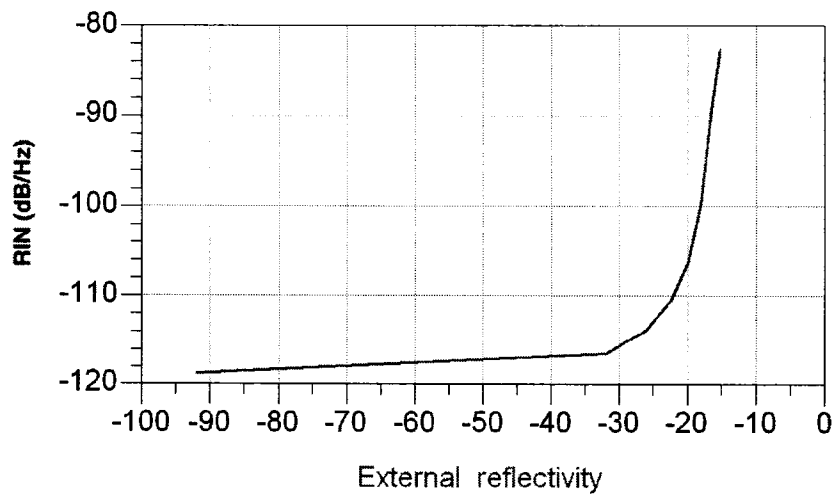


Figure 3.22: Simulated RIN versus external reflectivity.

The results presented in this chapter will next be experimentally verified in Chapter 4.

3.6 Summary

In this chapter, the simulation of DFB laser's various parameters in existence of optical feedback was presented. The feedback terms for the proposed laser rate equations were derived and normalized. A laser model was implemented in ADS using the proposed rate equations in order to simulate various laser behaviors in existence of feedback. The laser's DC characteristics, noise, and linearity were simulated using various ADS setups. The DC simulation results showed that the laser diode's threshold current level was decreased due to feedback. Modifications to the laser's modulation response and linearity were observed through harmonic balance simulations. The model was improved by including the noise terms to the rate equations and then the laser's intensity noise was simulated in a transient simulation setup. RIN simulation results matched those found in the literature.

Chapter 4

Experimental Work and Model Verification

4.1 Introduction

In this chapter, we discuss the experimental setup and demonstrate the results of the simulation work. The influence of the optical back-reflections on the laser DC characteristics, threshold current changes, linearity, and noise are all examined and analyzed.

4.2 DC Measurements

In order to determine the power required for a fiber-optic link, the measurement of the output optical power should be performed and analyzed for different feedback scenarios. This section shows how the feedback power can modify the DC characteristics of the laser diode and decreases the threshold current level. The model is also verified by comparing the measured to the simulation results.

4.2.1 Threshold Current Measurements Setup

Two single mode DFB laser diodes with different wavelengths were used in the experimental setup shown in Figure 4.1 on the following page. DFB laser diodes were mounted on the THORLABS TCLDM9 5.6 mm/9 mm laser diode mount. The ILX lightwave LDC-3724B laser diode controller was used to control the temperature and drive the laser. The emission wavelengths for the two DFB laser diodes were 1310 nm and 1550 nm. The DFB laser

diode output was launched to the T port of the OZ Optics Fiber Optic Beam Splitter (FOBS) and divided into two parts. Half of the power was coupled to the ILX Lightwave OMM-6810B optical power and wavelength meter to measure the output power. The other half of the power was sent to the OZ Optics fiber optic reflector through the OZ Optics variable attenuator to achieve the desired back reflection level. The Agilent 86140B Optical Spectrum Analyzer (OSA) was connected to the R port of the FOBS to monitor the reflected power. The feedback ratio was defined as the ratio of the reflected power to the laser output power without feedback. Fiber optic cables were used in the setup to avoid spurious reflections from interconnection points.

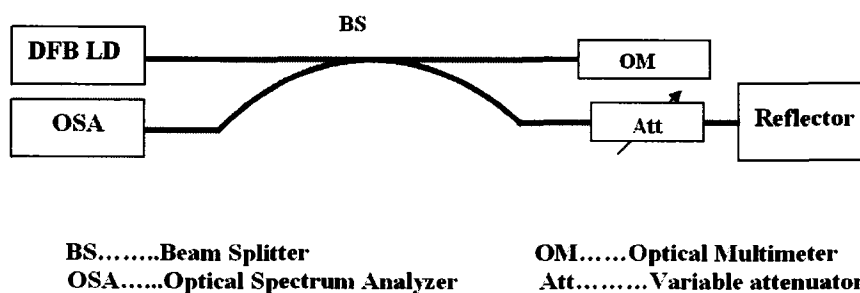


Figure 4.1: Experiment setup for DC measurements.

Figure 4.2 on the next page shows the setup used to measure the change in threshold current due to optical back-reflections. A brief description for each component is given in Appendix A.

4.2.2 Threshold Current Results and Model Verification

In order to obtain the optical power, the bias current was swept from 1 to 40 mA. Figure 4.3 and Figure 4.4 on page 67 show the measured optical power versus the biasing current for the 1550 nm DFB laser operating without feedback, and with -14 dB feedback. Figure 4.5 shows same results obtained using the 1310 nm DFB laser diode instead. We can conclude

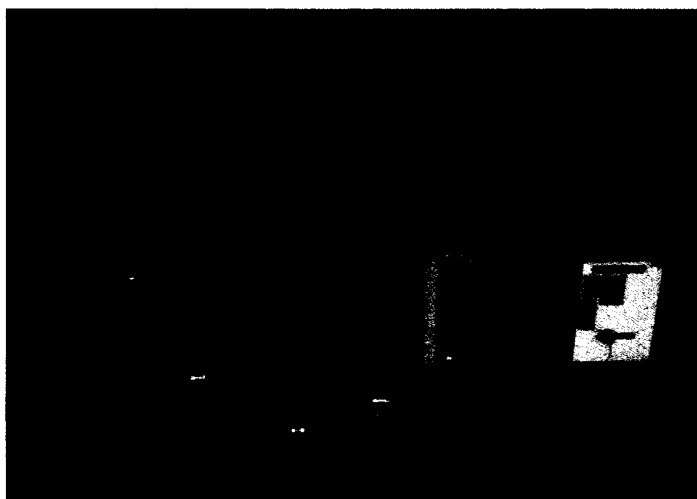


Figure 4.2: DC measurements experiment setup. Front right to left: the fiber optic reflector, the variable attenuator, the polarization controller, the fiber optic beam splitter, and the laser diode on the mount. Back right to left: the optical spectrum analyzer, the fiber optic power wavehead, the optical power and wavelength meter (top), and the laser diode controller (bottom).

from these results that the DFB laser diode threshold current was reduced due to the reflected power, which agrees with the simulated results.

Figure 4.6 on page 68 plots of the simulated threshold current versus the optical back-reflection coefficient. Some measured data points were also included for comparison purposes. The power measurements accuracy for the used optical power meter is 0.05. The results show a good agreement between simulation and measurements, the absolute error values for all measured points lie within a maximum allowable error level of 0.05 of the corresponding simulated values.

4.2.3 DFB Laser Diode Spectra Measurement Setup and Results

Figure 4.7 on page 69 shows the experimental setup used to examine the DFB laser diode spectra for different feedback levels. The single mode DFB laser diode was mounted on the THORLABS TCLDM9 5.6 mm/9 mm Laser diode Mount, and it was temperature controlled and biased by the ILX lightwave LDC-3724B laser diode controller. The emission wavelength for the DFB laser diode was 1550 nm. The DFB laser diode output is sent

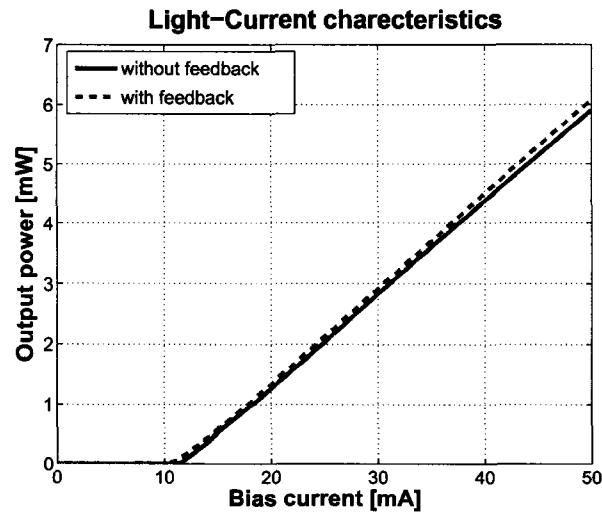


Figure 4.3: P-I curve for 1550 nm DFB laser diode without feedback and with -14 dB feedback ratio.

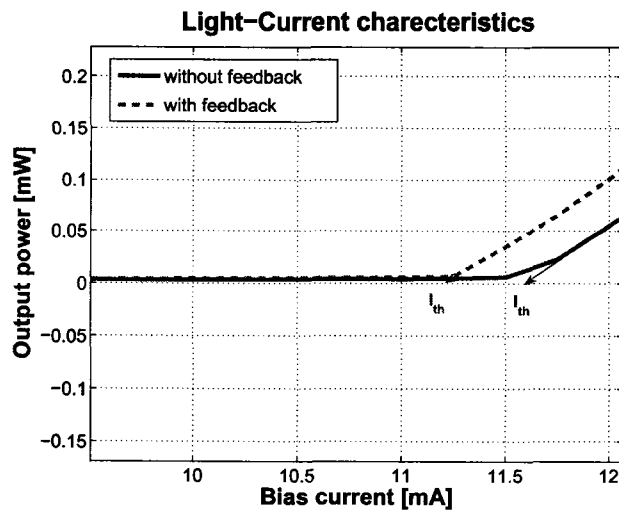


Figure 4.4: Threshold current change for 1550 nm DFB laser diode with -14 dB feedback ratio compared to the same laser diode without feedback.

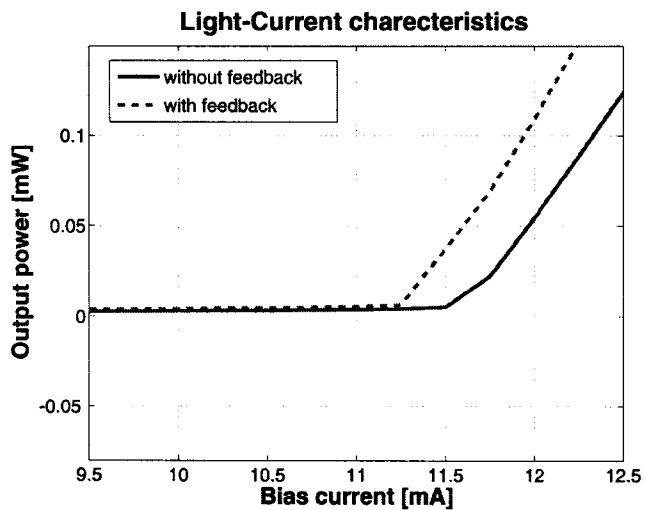


Figure 4.5: Threshold current change for 1310 nm DFB laser diode with -14 dB feedback ratio compared to the same laser diode without feedback.

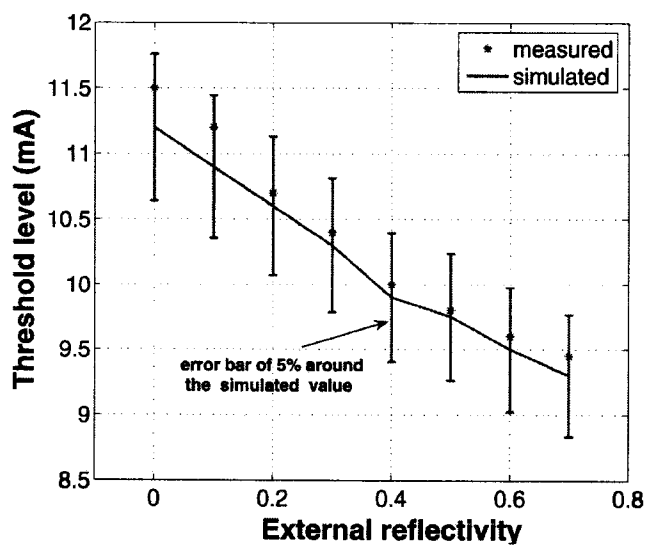


Figure 4.6: Measured and simulated threshold current change due to optical back-reflection.

to the T port of the FOBS, where it was divided. One half of the power was coupled to the Agilent 86140B OSA, which was used to examine the spectral characteristics of the laser diode output, while the other half was sent to the OZ Optics Fiber optic reflector to achieve the desired back reflection level. The feedback level was controlled by the OZ Optics variable attenuator. The OZ Optics Polarization controller was used to guarantee that the power reflected back into the laser had the same polarization as the emitted power. The reflected power through the R port of the FOBS was measured using the ILX Lightwave OMM-6810B Optical Power and Wavelength Meter. A brief description of the different components used in the measurements is included in Appendix A.

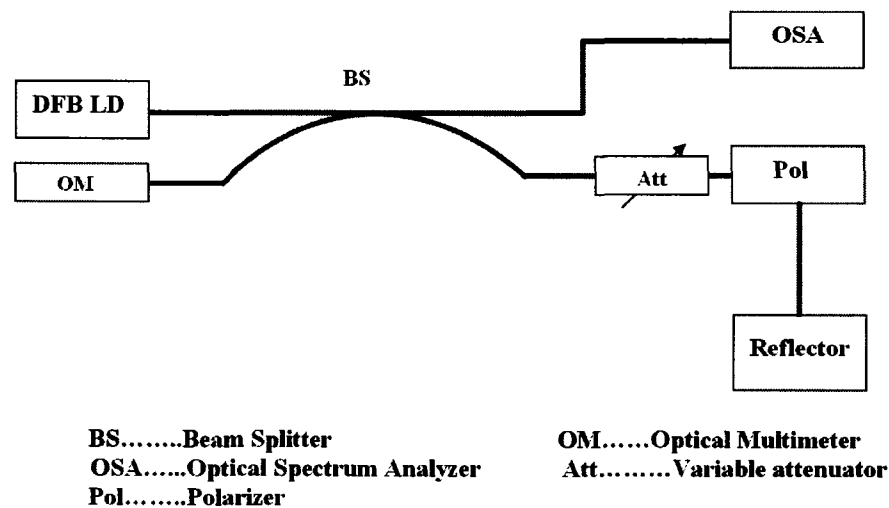


Figure 4.7: DFB laser diode spectra experiment setup.

Figure 4.8 on the next page shows the spectra of the 1310 nm DFB laser diode with different feedback levels. Figure 4.8(a) shows the spectrum of the free running DFB laser diode biased at 12 mA without any induced feedback. In this case, the DFB laser diode operates in a single longitudinal mode. The spectrum still shows a single mode operation under -40 dB optical reflection as shown in Figure 4.8(b). As the feedback level was increased to -15 dB, the laser became unstable and the DFB laser diode spectrum was broadened due to its operation in the coherence collapse regime as shown in Figure 4.8(c). The feedback level was further increased to -10 dB to drive the DFB laser diode to operate

in the external cavity operation regime (Regime V) with a single mode operation as shown in Figure 4.8(d) [54].

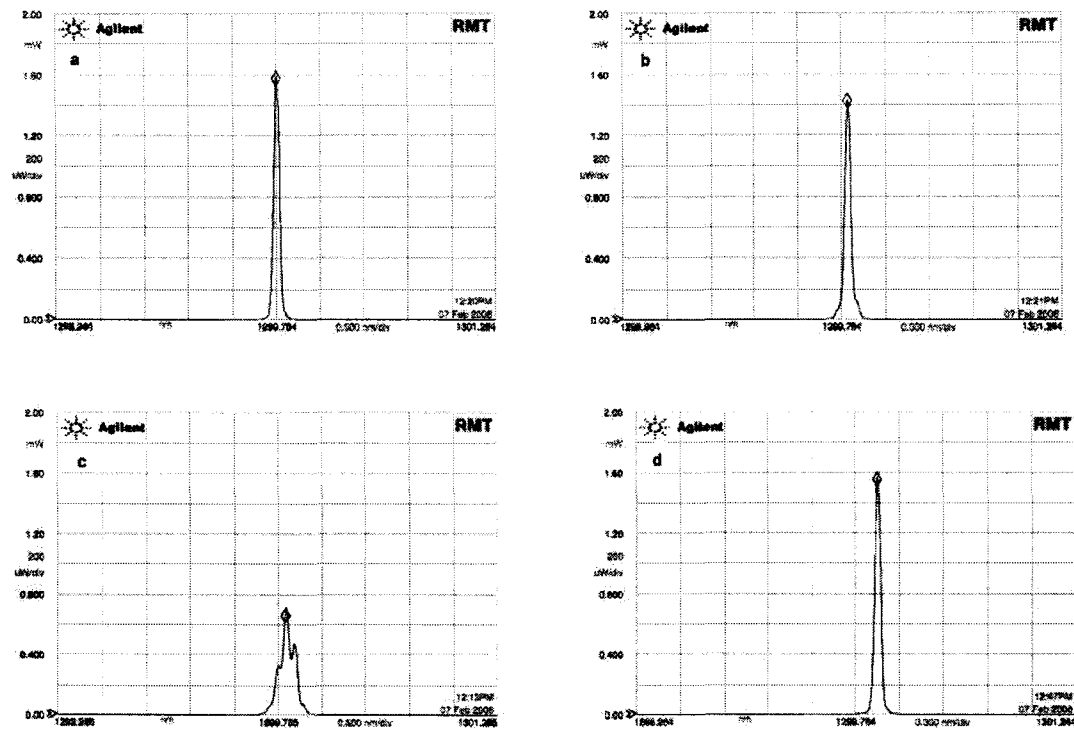


Figure 4.8: Optical spectra of the 1310 nm DFB laser diode biased at 12 mA and with different optical feedback powers: a) -45 dB b) -40 dB c) -15 dB d) -10 dB.

4.3 Noise and Linearity Measurements

The Agilent 71400C lightwave signal analyzer shown in Figure 4.9 on the following page is a tool to measure important laser diode characteristics such as signal strength, modulation bandwidth, signal distortion, and noise. The Agilent 71400C lightwave signal analyzer can be used in conjunction with the Agilent 11980A fiber-optic interferometer to measure the laser diode linewidth.

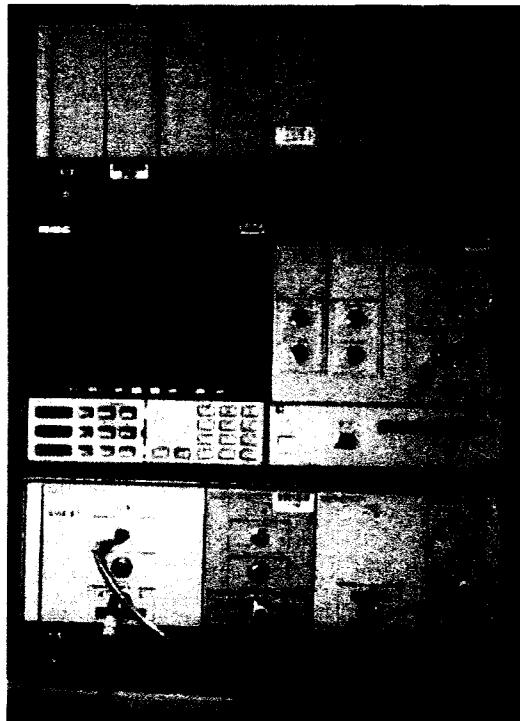


Figure 4.9: Agilent 71400C lightwave signal analyzer.

4.3.1 RIN Measurements Experimental Setup

The Agilent 71400C lightwave signal analyzer with a RIN measurement module (a special software routine) was used for the laser RIN measurements. The RIN module is mainly capable of measuring two quantities, RIN_{SYS} and RIN_{laser} . RIN_{SYS} measures the total system noise taking into account the laser intensity noise, shot, and the thermal noise of the instrument. RIN_{laser} is equivalent to the ratio of the laser noise to the average power precluding the shot and thermal noise terms.

Figure 4.10 on the next page shows the experimental setup used in the measurements. The DFB laser diode was mounted on the *THORLABS TCLDM9 5.6 mm/9 mm* laser diode mount, and it was temperature controlled and biased by the *ILX lightwave LDC – 3724B* laser diode controller. The emission wavelength for the DFB laser diode was 1310 nm . The DFB laser diode output is sent to the T port of the FOBS, where it was split into two halves. The first half of the power was coupled to the *Agilent 71400C* lightwave signal analyzer to measure the RIN. The measured RIN was then displayed on a 70004A display unit and connected through a GPIB (IEEE488.2 interface) to a personal computer for acquiring screen images and controlling trace data using the *Agilent N1031A BenchLink* lightwave software. The remaining half of the power was directed to the OZ Optics fiber optic reflector to achieve the desired back reflection level. The feedback level was controlled by the OZ Optics variable attenuator. The OZ Optics Polarization controller was used to guarantee that the power reflected back into the laser had the same polarization as the emitted power. The reflected power through the R port of the FOBS is measured using the *ILX Lightwave OMM – 6810B* Optical Power and Wavelength Meter.

4.3.2 RIN Measurement Results and Model Verification

RIN versus bias current

Figures 4.11 - 4.15 on page 75 show the measured average relative intensity noise for 1300 nm DFB at 1 GHz frequency offset. The DFB laser was operated at five different bias current levels, 25, 30, 35, 40, and 60 mA. The measured unintended back-reflection that attributed to the connectors was -45 dB .

The RIN exhibits a peak at the laser's relaxation oscillation frequency, this peak shifts

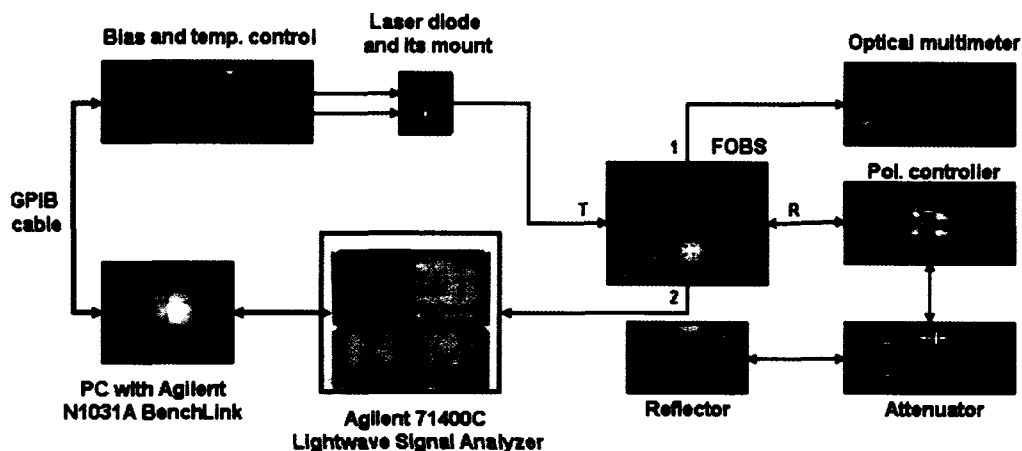


Figure 4.10: Relative intensity noise measurement experimental setup.

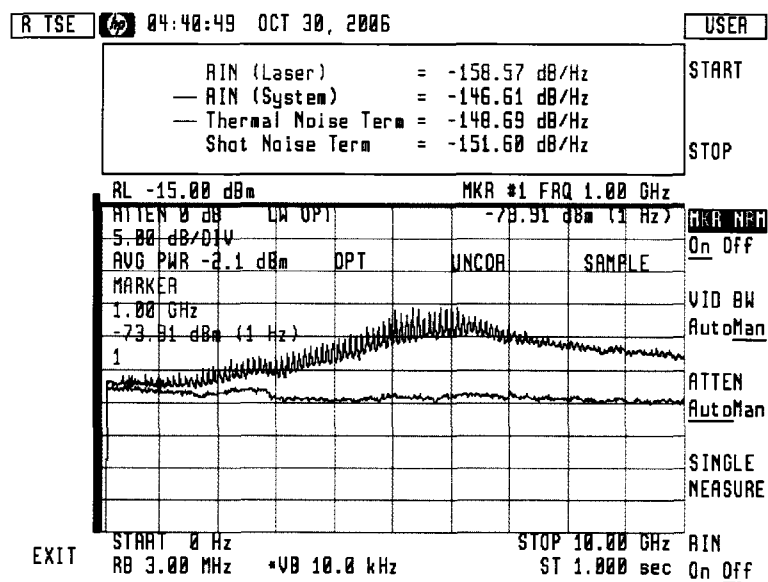


Figure 4.11: Measured relative intensity noise of 1300 nm DFB laser biased at 25 mA and measured at 1 GHz frequency offset.

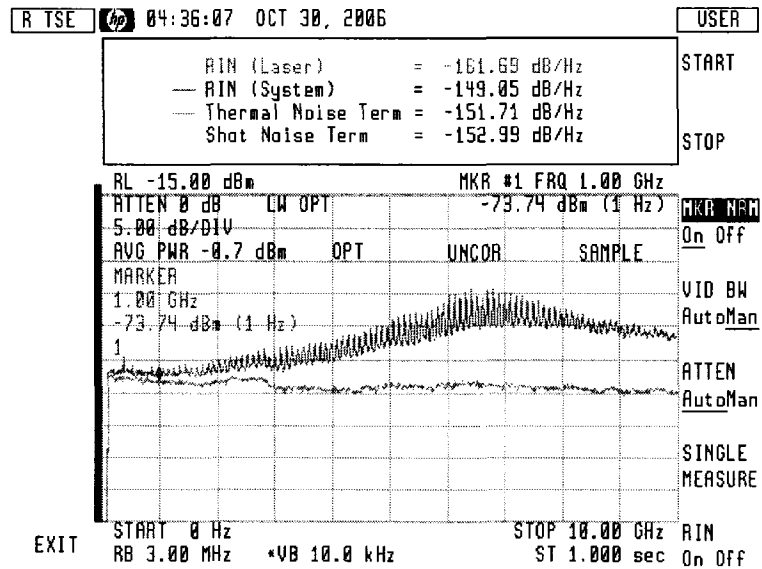


Figure 4.12: Measured relative intensity noise of 1300 nm DFB laser biased at 30 mA and measured at 1 GHz frequency offset.

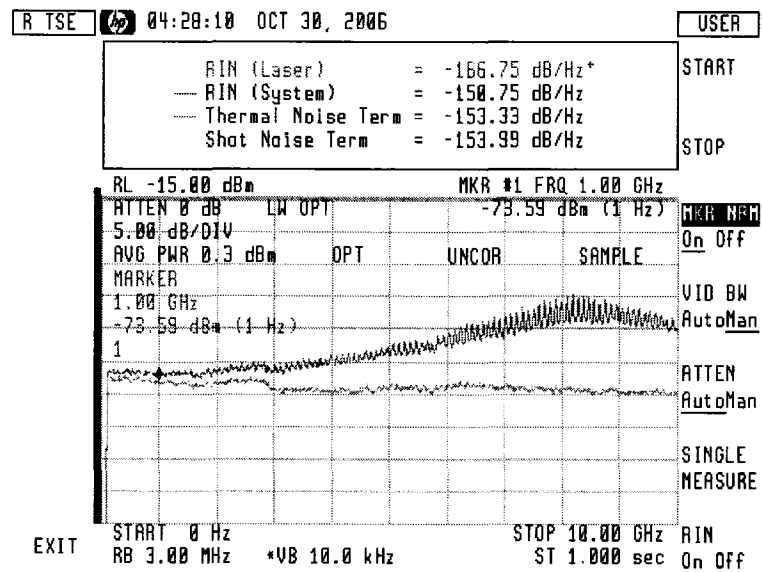


Figure 4.13: Measured relative intensity noise of 1300 nm DFB laser biased at 35 mA and measured at 1 GHz frequency offset.

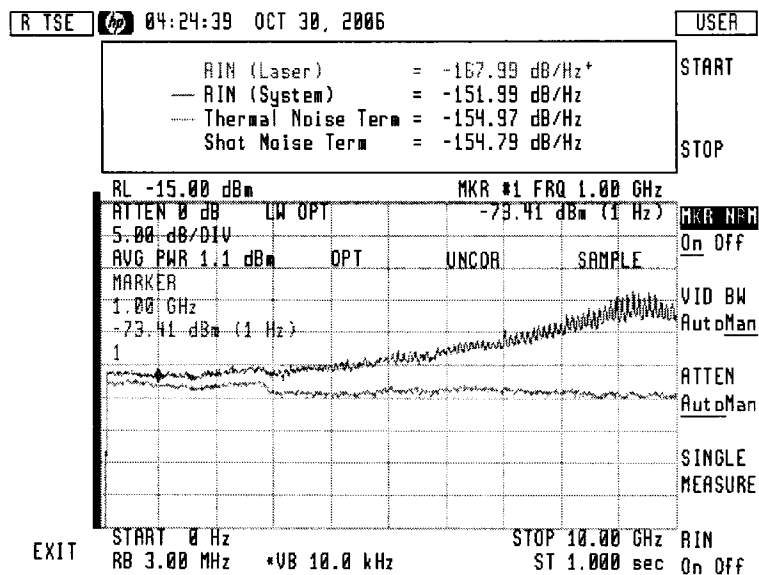


Figure 4.14: Measured relative intensity noise of 1300 nm DFB laser biased at 40 mA and measured at 1 GHz frequency offset.

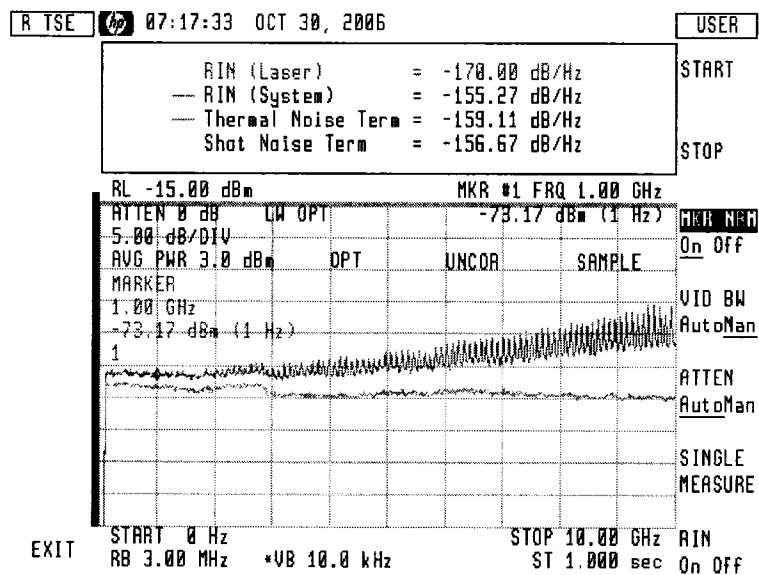


Figure 4.15: Measured relative intensity noise of 1300 nm DFB laser biased at 60 mA and measured at 1 GHz frequency offset.

towards higher values as the bias current increases. The above measured RIN for different bias levels are summarized in Table 4.1 and are plotted in Figure 4.16 on the next page.

Table 4.1: Measured average RIN at 1 GHz frequency offset for different bias levels

Bias Level [mA]	Measured average RIN [dB/Hz]
25	-158.57
30	-161.69
35	-166.75
40	-167.99
60	-170

Figure 4.16 on the following page shows the measured and simulated RIN as a function of the laser bias current for a fixed unintentional feedback level of -45 dB/Hz. The results show that the RIN is a decreasing function of bias current; increasing bias current from 25 mA to 60 mA decreases the measured RIN value from -158.57 dB/Hz to -170 dB/Hz. Agilent 71400C light wave signal analyzer can measure the laser RIN with an accuracy variations of (3-6 dB). The results demonstrate that the simulated and measured results are in a good agreement, the absolute error values for all measured points lie within a maximum allowable error level of 2 dB of the corresponding simulated values. The results also agree with findings reported in the literature [12].

RIN versus external reflectivity

Figures 4.17 on the next page - 4.21 on page 79 show the measured average relative intensity noise of a 1310 nm DFB laser diode for bias current level of 15 mA and average external reflectivity ranging from -45 dB to -10 dB. The rest of the measurement results are found in Appendix A.

The RIN spectrum of the DFB laser diode without intentional feedback is shown in Figure 4.17 on the next page. The RIN peak at around 3.5 GHz, which is the laser relaxation oscillation frequency at bias level of 15 mA. The measured average RIN is -121.99 dB/Hz. When weak feedback, -40 dB, is applied to the DFB laser, the measured average RIN is slightly increased to -120.43 dB/Hz as shown in Figure 4.18 on page 78.

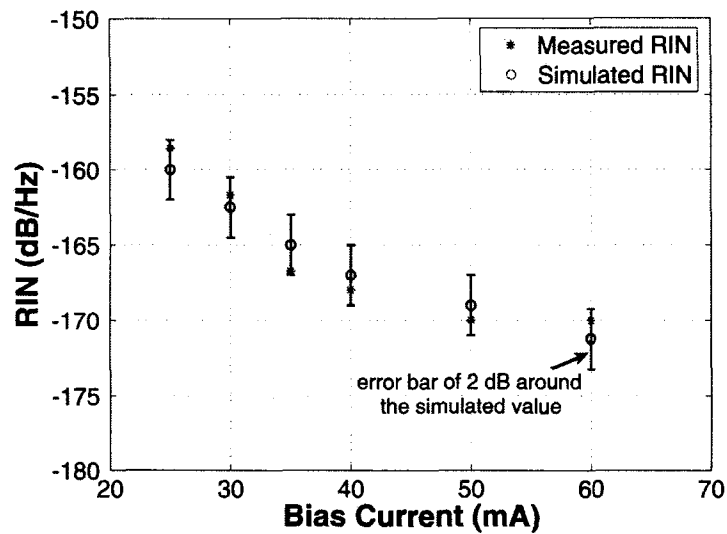


Figure 4.16: Measured and simulated relative intensity noise vs. bias current.

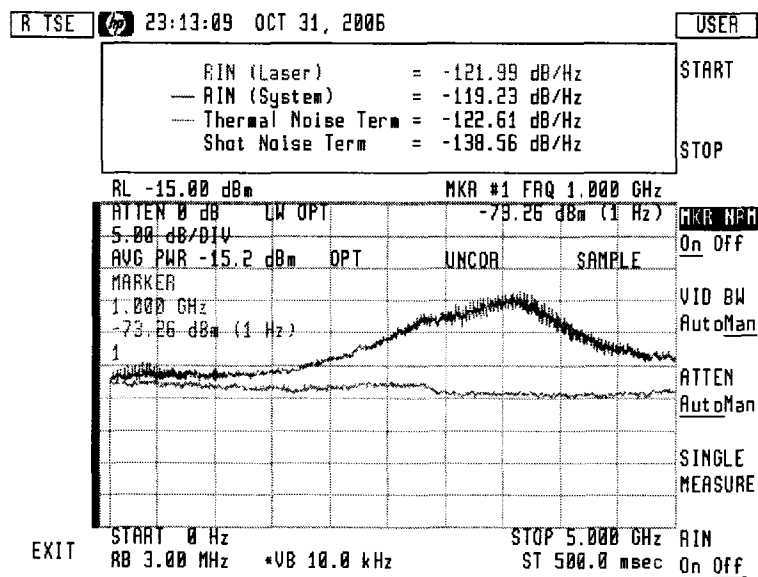


Figure 4.17: Measured relative intensity noise for bias current level of 15 mA and external reflectivity of -45 dB.

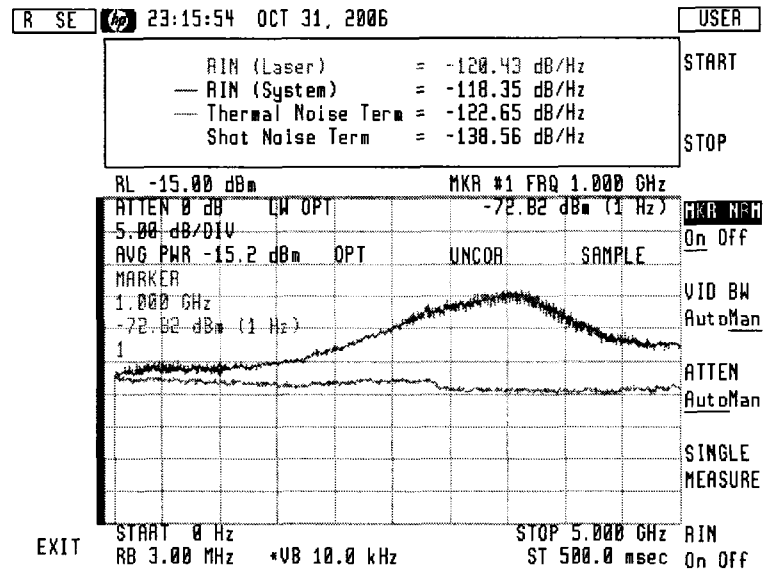


Figure 4.18: Measured relative intensity noise for bias current level of 15 mA and external reflectivity of -40 dB.

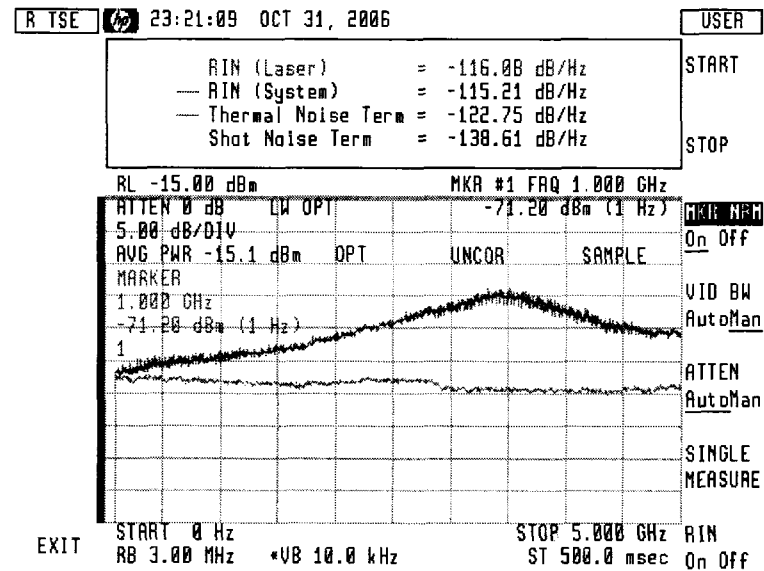


Figure 4.19: Measured relative intensity noise for bias current level of 15 mA and external reflectivity of -27 dB.

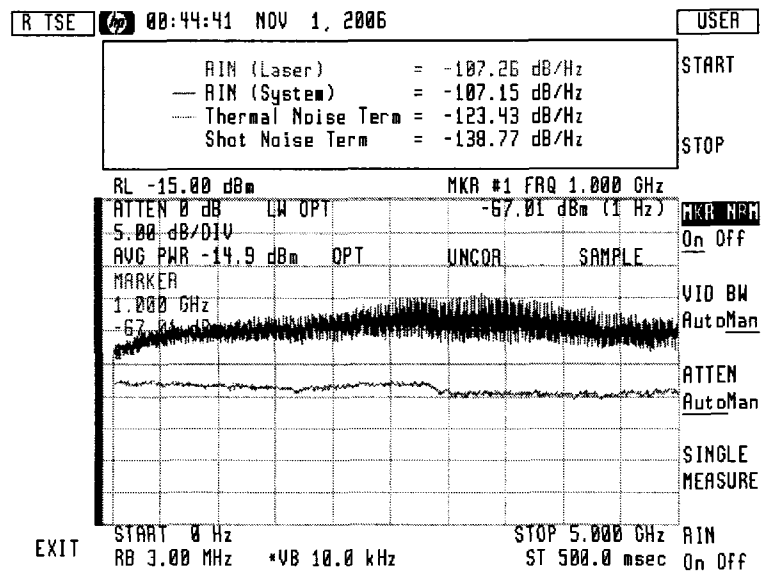


Figure 4.20: The measured relative intensity noise for bias current level of 15 mA and external reflectivity of -20 dB.

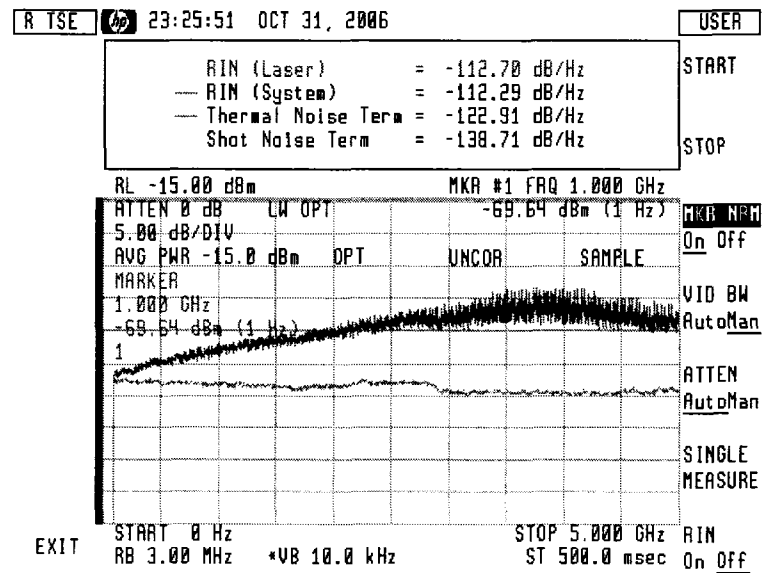


Figure 4.21: Measured relative intensity noise for bias current level of 15 mA and external reflectivity of -10 dB.

A bigger increase in the RIN is observed at higher feedback as shown in Figure 4.19 on page 78. The measured average RIN increased to -116.08 dB/Hz when a feedback level of -27 dB was applied to the DFB laser. A considerable increase in the RIN spectrum is observed when the feedback is further increased to 20 dB due to the operation in the coherence collapse regime. The measured average RIN in this case was -107.26 dB/Hz as shown in Figure 4.20 on the preceding page. At this regime the laser emits in random phase, the linewidth of the emitted light is much broadened, and no distinct peak for the noise spectrum can be observed. Increasing the feedback to very high level, 10 dB, caused the laser to reach the stable feedback Regime V. The measured average RIN was -112.70 dB/Hz as shown in Figure 4.21 on the previous page. More reduction in the RIN of the DFB laser is expected to occur for higher feedback. The available feedback in our experiments is limited to only 10 dB due to the insertion loss of the various used equipment.

The above measured average RIN results for different feedback levels are summarized in Table 4.2 and are plotted in Figure 4.22 on the following page. The figure shows that the average RIN increases slightly as the external reflectivity increases. However, when the feedback level exceeds a certain level (-30 dB in these measurements), the measured relative intensity noise of the laser exhibits higher values due to the laser operation in Regime IV, the coherence collapse regime. A further increase in the feedback level (greater than -15 dB in these measurements) forced the DFB laser diode into feedback Regime V with low measured relative intensity noise. The simulation results were included in Figure 4.22 to facilitate a comparison with the measured results. Agilent 71400C lightwave signal analyzer can measure the laser RIN with an accuracy variations of (3-6 dB). The simulated and measured results are in good agreement for feedback regimes I, II, III, and IV, the absolute error values for all measured points lie within a maximum allowable error level of 5 dB of the corresponding simulated values. These results are also in good agreement with results presented in [30] and [42].

Although the laser rate equations that include feedback and noise terms were normalized to improve the simulator numerical solvers convergence, the model was unable to simulate the RIN in feedback Regime V and faced convergence difficulties. It was observed that the ADS numerical solver was unable to solve these rate equations as the laser enters feedback Regime V, this is attributed to the high reflection level in Regime V.

Table 4.2: Measured average RIN at 1 GHz frequency offset for 15 mA bias current and different feedback levels

Feedback Level [dB]	Measured average RIN [dB/Hz]
-45	-121.99
-42	-120.88
-40	-120.43
-36	-120.51
-33	-120.08
-29	-119.80
-27	-116.08
-24	-112.03
-20	-107.26
-15	-109.06
-10	-112.70

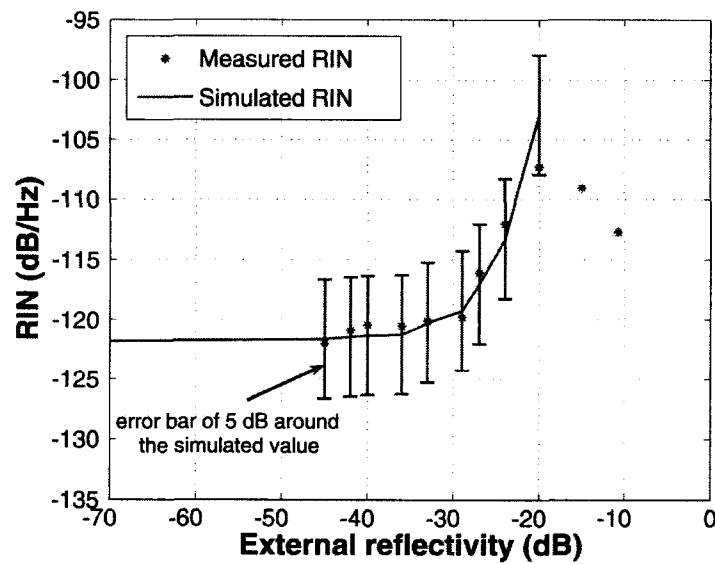


Figure 4.22: Measured and simulated RIN [dB/Hz] of DFB for different external reflectivities [dB], $I_{bias}=12$ mA, $\lambda=1310$ nm.

It is worth noting that the drop that exists at a frequency 2.9 GHz is due to the fact that the Agilent 71400C lightwave signal analyzer uses two different tracking generator modules to cover the full frequency range from 20 Hz to 18 GHz. The first module covers frequencies ranging from 20 Hz to 2.9 GHz, while the second covers frequencies ranging from 2.7 GHz to 18 GHz. The drop that exists at a frequency of 2.9 GHz is due to the transition from the first module to the second.

4.3.3 Modulation Frequency Response Measurements

The modulation frequency response of the DFB laser diode at different optical back-reflections levels was measured using the experimental setup shown in Figure 4.23 on the next page. The DFB laser diode was mounted on the *THORLABS TCLDM9 5.6 mm/9 mm* laser diode mount. It was temperature controlled and biased by the *ILX lightwave LDC-3724B* laser diode controller. The emission wavelength for the DFB laser diode was 1310 nm. The DFB laser diode output is sent to the T port of the FOBS, where it was divided. Half of the power was coupled to the *Agilent 71400C* lightwave signal analyzer to measure the modulation frequency response. The other half of the power was directed to the OZ Optics fiber optic reflector to achieve the desired back reflection level. The feedback level was controlled by the OZ Optics variable attenuator. The OZ Optics Polarization controller was used to guarantee that the reflected power back into the laser had the same polarization as the emitted power. The reflected power through the R port of the FOBS was measured using the *ILX Lightwave OMM-6810B* Optical power and wavelength meter.

In this experiment, an Agilent RF tracking generator (70300A, 100 Hz to 2.9 GHz) and an Agilent micro-wave tracking generator (70301A, 2.7 GHz to 18 GHz) from the Agilent 71400C lightwave signal analyzer were used to provide a sweep modulation frequency source whose frequency was synchronized with the sweep of the spectrum analyzer. The RF output of the 70300A was connected to the RF input of 70301A to cover the full range of frequency (100 HZ to 18 GHZ). The output of the tracking generator was used to directly modulate the laser diode using an RF cable connected to a standard RF-SMA connector in the laser mount. The mount is designed with a bias-T that accepts a 50 Ω impedance modulation input through a standard RF-SMA connector. The modulated light enters the

lightwave section in the 71400C system through a Single-Mode Fiber (SMF) connected to the front-panel input connector. The optical power is detected, collimated, amplified, and then focused onto a 22 GHz bandwidth InGaAs photodetector using the Agilent 70810B lightwave section. The data was displayed on a 70004A display unit and acquired through a GPIB (IEEE488.2 interface) to a personal computer for obtaining screen images and collecting trace data using Agilent N1031A BenchLink lightwave software.

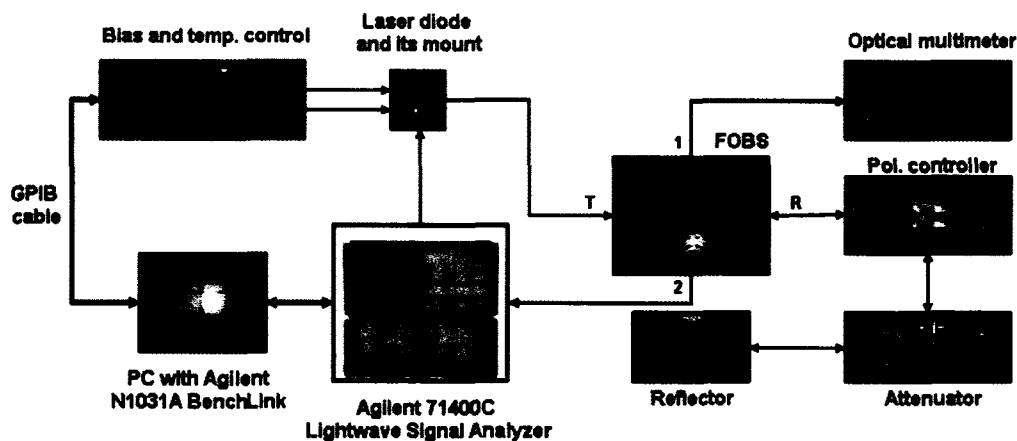


Figure 4.23: Modulation frequency response measurement experimental setup.

Figure 4.24 on the following page through Figure 4.27 on page 85 show the measured modulation frequency response of 1300 nm DFB laser diode biased at 30 mA, with different feedback levels.

The measured relaxation oscillation frequency was 6.444 GHz with optical back-reflections of -45 dB, and 6.472 GHz with optical back-reflections of -30 dB as shown in Figures 4.24 and 4.25 respectively. When the feedback level was increased from -15 dB to -10 dB the measured relaxation oscillation frequency increased from 6.506 GHz to 6.534 GHz as shown in Figures 4.26 on page 85 and 4.27 on page 85 respectively.

4.3.4 Distortion Measurements Setup and Results

The linearity performance of the laser is determined by measuring different types of distortion that are caused by the laser. In this experiment, Agilent 71400C lightwave signal

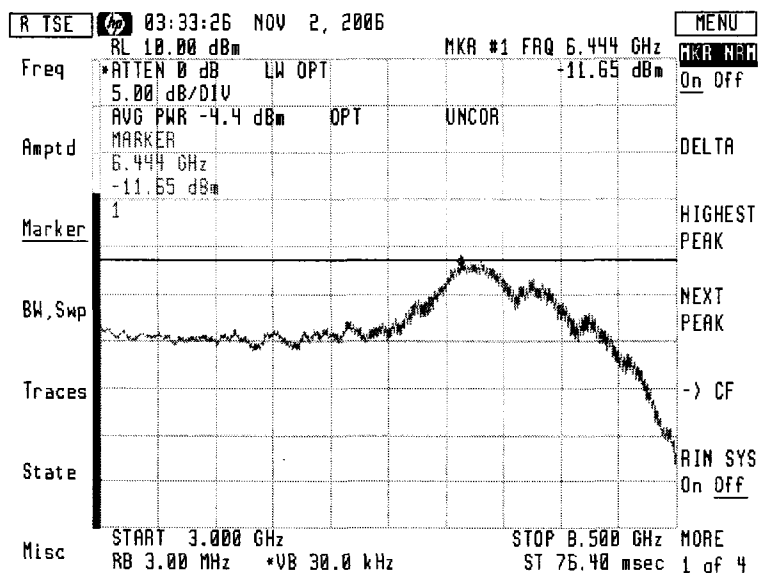


Figure 4.24: The measured relaxation oscillation frequency of the 1310 nm DFB laser diode biased at 30 mA with -45 dB.

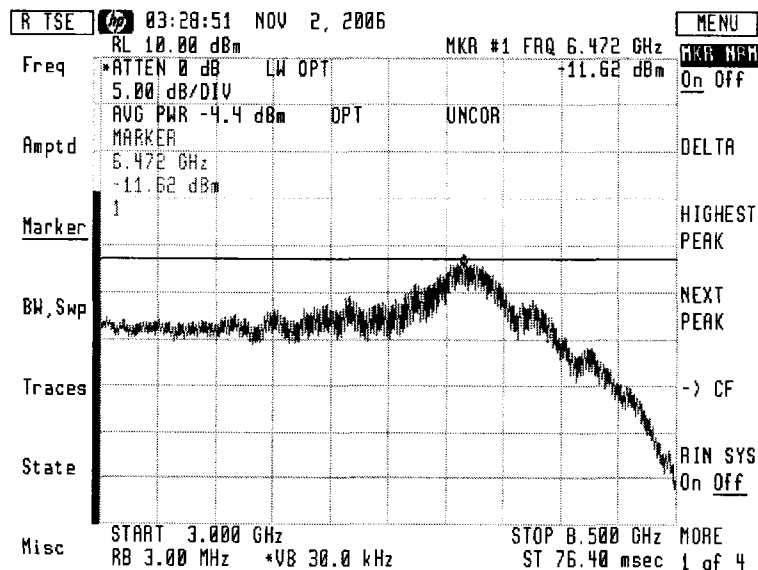


Figure 4.25: Measured relaxation oscillation frequency of the 1310 nm DFB laser diode biased at 30 mA with -30 dB.

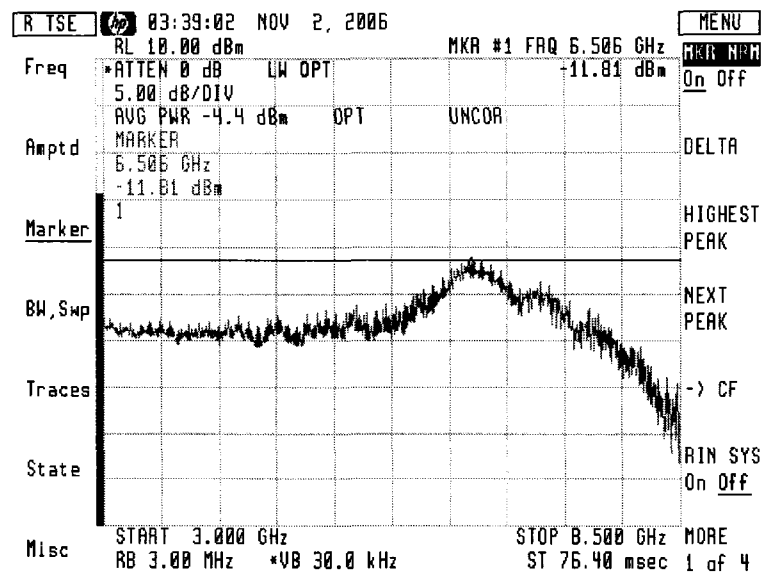


Figure 4.26: Measured relaxation oscillation frequency of the 1310 nm DFB laser diode biased at 30 mA with -15 dB.

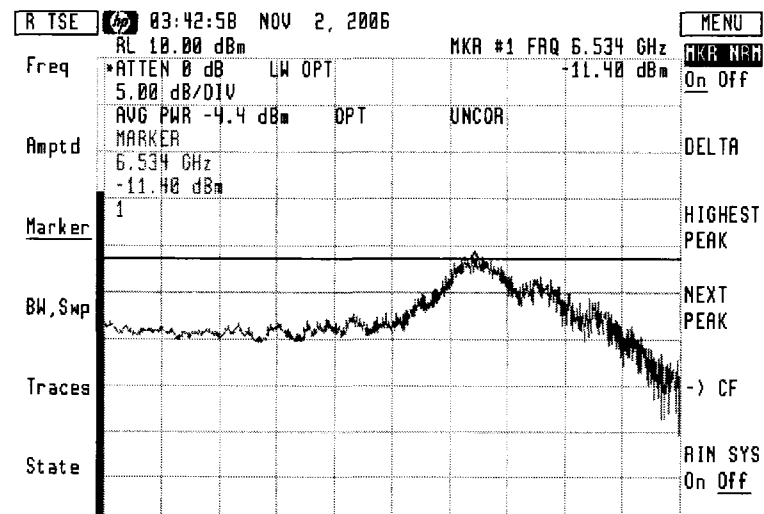


Figure 4.27: Measured relaxation oscillation frequency of the 1310 nm DFB laser diode biased at 30 mA with -10 dB.

analyzer and Agilent E4438C ESG vector signal generator were used to measure the second and third order harmonic distortion in presence of feedback. The setup was similar to that of modulation frequency response measurement that was presented in the previous section, except that the output from E4438C ESG signal generator was used to modulate the DFB laser diode through the T bias of the laser mount. Figure 4.28 shows the detailed block diagram of the experimental setup for the distortion measurement in presence of optical back-reflections.

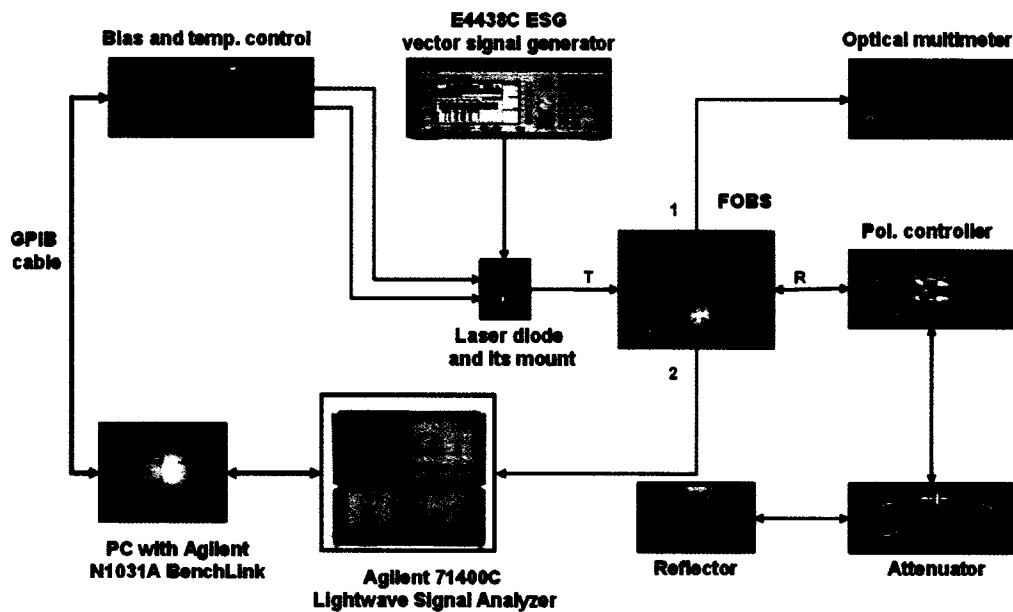


Figure 4.28: Distortion measurement experimental setup.

Figure 4.29 on the next page shows the measured second order harmonic distortion of DFB laser at different feedback levels normalized to the fundamental tone power. The results show that as the feedback level increases, the second order harmonic distortion increases. At a bias current of 20 mA, the measured second order harmonic distortion was -17 dB for the isolated DFB laser, -15 dB for the same DFB laser with -45 dB back-reflection, and -12 dB for the same DFB laser with -15 dB back-reflection. The results also show that the second order harmonic distortion is a decreasing function of the bias current for all of feedback levels.

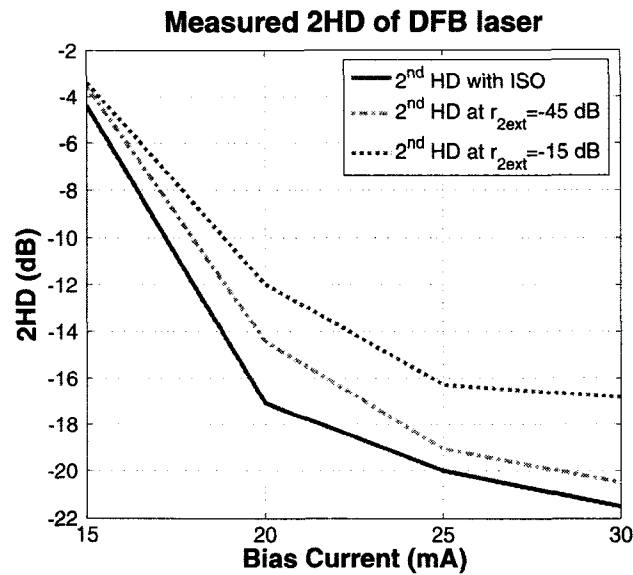


Figure 4.29: Measured second order harmonic distortion of DFB laser at different feedback levels.

Figure 4.30 on the following page shows the measured third order harmonic distortion of the DFB laser at different feedback levels normalized to the fundamental tone power. The results show that as the feedback level increases, the third order harmonic distortion increases. At a bias current of 20 mA, the measured third order harmonic distortion is -18 dB for the isolated DFB laser, -17 dB for the same DFB laser with -45 dB back-reflection, and -13 dB for the same DFB laser with -15 dB back-reflection. The results also show that the third order harmonic distortion is a decreasing function of the bias current for of all feedback levels.

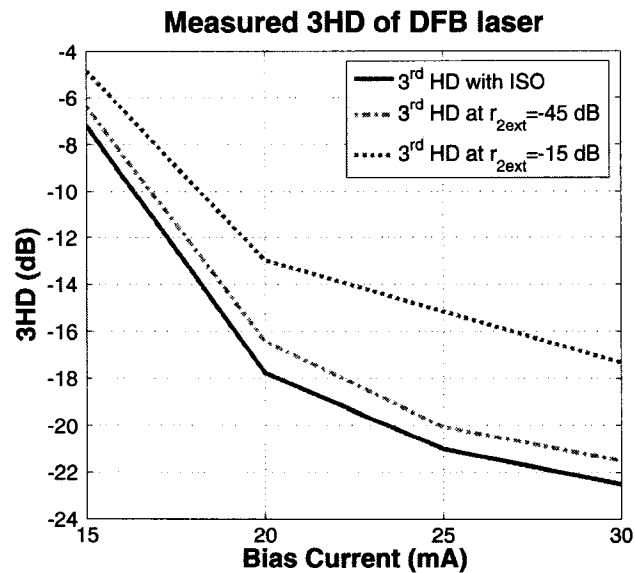


Figure 4.30: Measured third order harmonic distortion of DFB laser at different feedback levels.

4.4 Summary

This chapter contains various experimental setups that have been used to examine the laser performance with optical feedback as well as to verify the simulation results. Different DFB laser spectra were shown for different optical feedback levels. An induced tunable back-reflections setup were presented to measure laser's DC characteristics, noise, and linearity using the Agilent 71400C lightwave signal analyzer. The simulation and measurement results were compared and the results closely matched.

Chapter 5

FBG Design and Implementation

5.1 Introduction

In this chapter the design and implementation of the Fiber Bragg Grating (FBG) will be presented. The required FBG parameters will be determined based on the laser output characteristics, and the required back-reflection level needed to drive the laser to the feed-back Regime V. Simple analytical formulas were used to determine the primarily design parameters, then the OptiGrating design software was used to design the desired FBG. Finally the FBG was implemented in the laboratory.

5.2 FBG Introduction and Basic Calculations

5.2.1 FBG Principles

The FBG consists of a fiber segment whose core refractive index varies periodically along its length as shown in Figure 5.1 on the next page. This refractive index variation is formed by exposure of the fiber core to an intense optical interference pattern [55]. The FBG has many advantages, such as: achieving all-fiber geometry, low insertion loss, and low cost. In addition to its flexibility, it is able to achieve the desired spectral characteristics [56]. The FBGs can be used in many applications including DFB lasers, all fiber lasers, optical filters for WDM systems, dispersion compensation in optical communications, and optical sensors [57]. In this work the FBG will be attached to the laser pigtail to work as a reflector. Although the presence of the FBG will reduce the laser output, the optical feedback from the FBG will reduce the laser threshold current which will compensate for

the power reduction, and give almost the same P-I characteristics of a laser without the attached FBG [58].

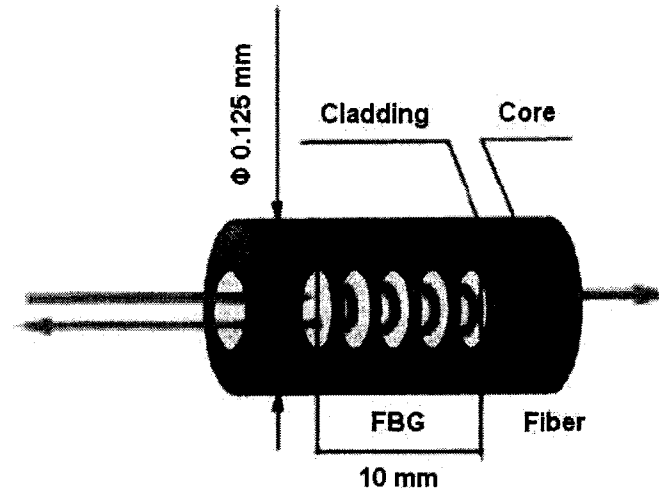


Figure 5.1: FBG structure

The coupled mode theory can be used to analyze the field propagation in the FBG, and to obtain the quantitative information about the diffraction efficiency and spectral characteristics of the FBG. It provides a straightforward technique that can model the optical properties of the FBG accurately [56]. The coupled mode approach involves the numerical solution of two coupled differential equations. An analytic solution is possible in case of uniform FBGs. Also, matrix methods such as the transfer matrix method can be used in the analysis; where the FBG is divided into sections, the length of each section is larger than the largest corrugation period. The variation of the refractive index of each section is considered as a uniform grating described by a transfer matrix, the product of the individual matrices give the global matrix which characterizes the FBG [57].

The FBG is characterized by its length and grating period, which can be obtained from the following relations:

$$2n_{eff}\Lambda = \lambda_{Bragg} \quad (5.2.1)$$

$$r_{max} = \tanh^2(\kappa L) \quad (5.2.2)$$

where n_{eff} is the effective refractive index, Λ is the grating period, λ_{Bragg} is the grating wavelength, r_{max} is the Bragg grating maximum reflectivity, r_{max} is the Bragg grating maximum reflectivity, L is the grating length, κ is the grating coupling coefficient.

5.2.2 FBG Parameter Calculations

Laser output parameters

The output of the Laser mate 1550 nm MQW-DFB pigtailed laser diode, mounted on the the THORLABS TCLDM9 5.6mm/9mm mount and driven by the ILX lightwave LDC-3724B laser diode controller, was measured with an Agilent 86140B Optical Spectrum Analyzer to determine the operating wavelength at different bias currents. Figure 5.2 on the following page shows the DFB laser diode output at bias current of 12mA, 15mA, 25mA, 35mA, and 40mA. The results show that as the bias current increases the laser emission wavelength shifts towards higher values, the laser emission wavelength was concentrated around 1553 nm with a deviation of ± 0.5 nm. With these results, the FBG wavelength have to match to this wavelength range.

FBG parameters

As shown in the previous section, the FBG wavelength should be designed for a wavelength of 1553 ± 0.5 nm. From the previous chapter, the feedback level required to cause the DFB laser diode to operate in feedback Regime V should be greater than -10 dB. The FBG period and length can be calculated from (5.2.1 on the previous page) and (5.2.2 on the preceding page), for a feedback level of -7 dB, the FBG period is $\Lambda=0.5257 \mu m$ and the FBG coupling-length product κL is 0.4812.

5.3 OptiGrating Design Software

OptiGrating 4.2.1 is a powerful modeling software that offers many different options for analyzing and designing FBGs. The FBG shape, length, apodization, and chirp can be adjusted according to the fiber diameter and refractive index. The OptiGrating 4.2.1 can perform the necessary numerical simulations based on solving the coupled mode equations using the transfer matrix method. The detailed FBG design steps using OptiGrating 4.2.1

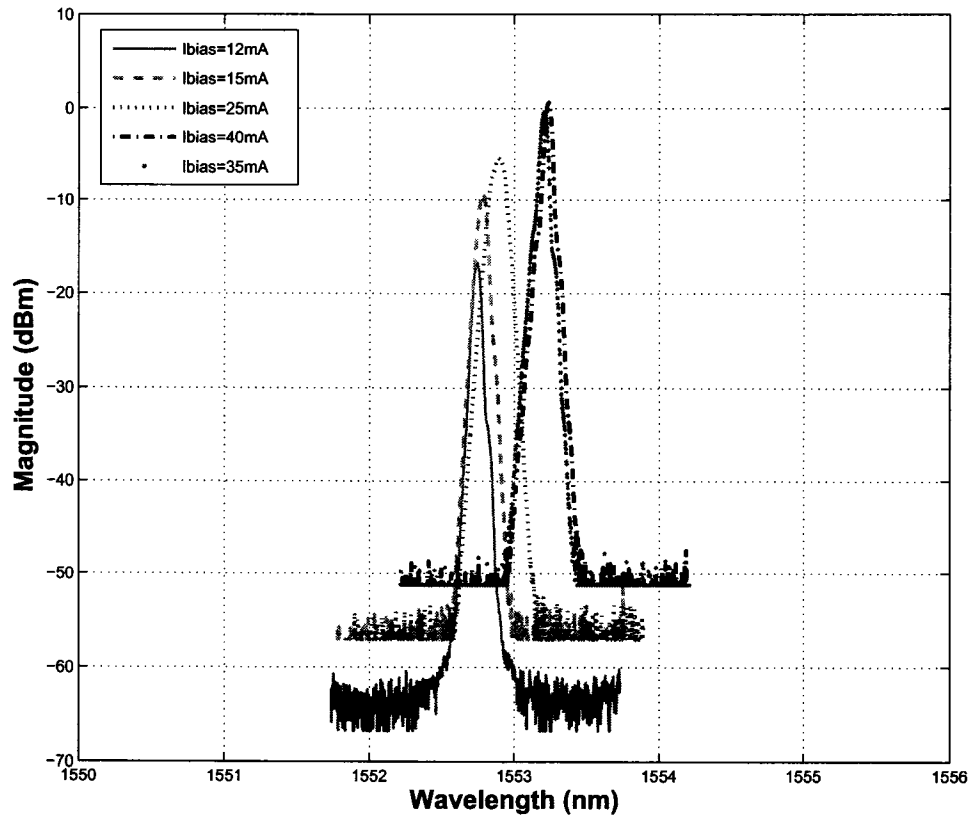


Figure 5.2: 1550 nm DFB laser diode spectrum at different bias current levels.

are included in Appendix B.

5.4 FBG Implementation

5.4.1 FBG Implementation Procedures

The grating is fabricated through an intense ultraviolet (UV) light irradiation using a phase mask as explained below.

Optical fiber preparation

As the ultraviolet can not well penetrate the acrylic (or polyimide) coatings that are on a standard optical fiber, a small section of the buffer material should be removed (2 cm) to expose the silica cladding. The optical fiber is placed in the appropriate fiber holder and temporary connectors are used on the fiber ends to monitor the Bragg grating with the source and optical spectrum analyzer.

Phase mask

Phase masks are corrugated circular sheets of silica. Each phase mask has a different pitch (periodicity) to the corrugated ridges on its surface. Bragg grating wavelength is determined by the phase mask pitch. The phase mask functions to split the incoming UV light into multiple diffracted beams as shown in Figure 5.3.

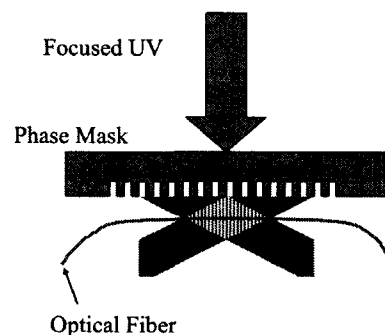


Figure 5.3: Phase mask.

Interferometric (Holographic) technique

The interferometric technique creates the UV interference pattern by splitting the incoming UV into two separate light paths and recombining them at the optical fiber location as shown in Figure 5.4. The splitting is done using the phase mask; once the phase mask splits the light, the two first order diffraction beams are guided to the optical fiber by two mirrors mounted to rotational stages. Bragg grating wavelength control is done by adjusting one of the mirrors to change the angle at which the two UV beams interfere.

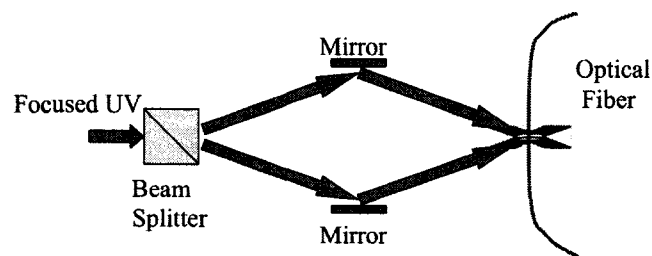


Figure 5.4: Interferometric technique.

Post processing of Bragg grating

Over time, the average refractive index of the Bragg grating decreases causing a shift in the Bragg wavelength. To prevent this from happening during testing the FBG must be annealed. Typical standard annealing bakes the Bragg gratings in an oven for 4 hours at 300 F.

Figures 5.5 on the next page and 5.6 on the following page show the FBG writing processes at the Carleton Laboratory for Laser Induced Photonic Structures (CLLIPS), while Figure 5.7 on page 96 shows the phase mask that has been used in the writing process.

5.4.2 The Implemented FBG Characteristics

Figure 5.8 on page 97 shows the implemented FBG reflection and transmission characteristics. This FBG will be designated as FBG1 throughout this work. FBG1 has its peak



Figure 5.5: Different equipments used in the implementation of FBG at CLLIPS.



Figure 5.6: FBG writing process at CLLIPS.

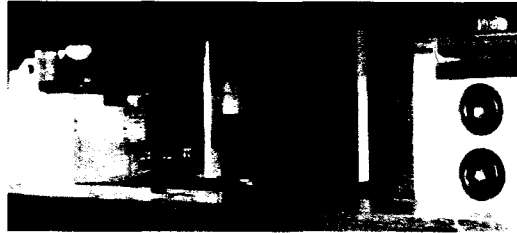


Figure 5.7: The phase mask used in FBG implementation at CLLIPS.

reflectivity of 0.2166 at wavelength 1552.649 nm, the measured 3-dB bandwidth of FBG1 is 0.914 nm.

The other implemented FBGs characteristics are shown in Appendix B. The performance of DFB laser diode attached to FBG will be discussed in Chapter 6.

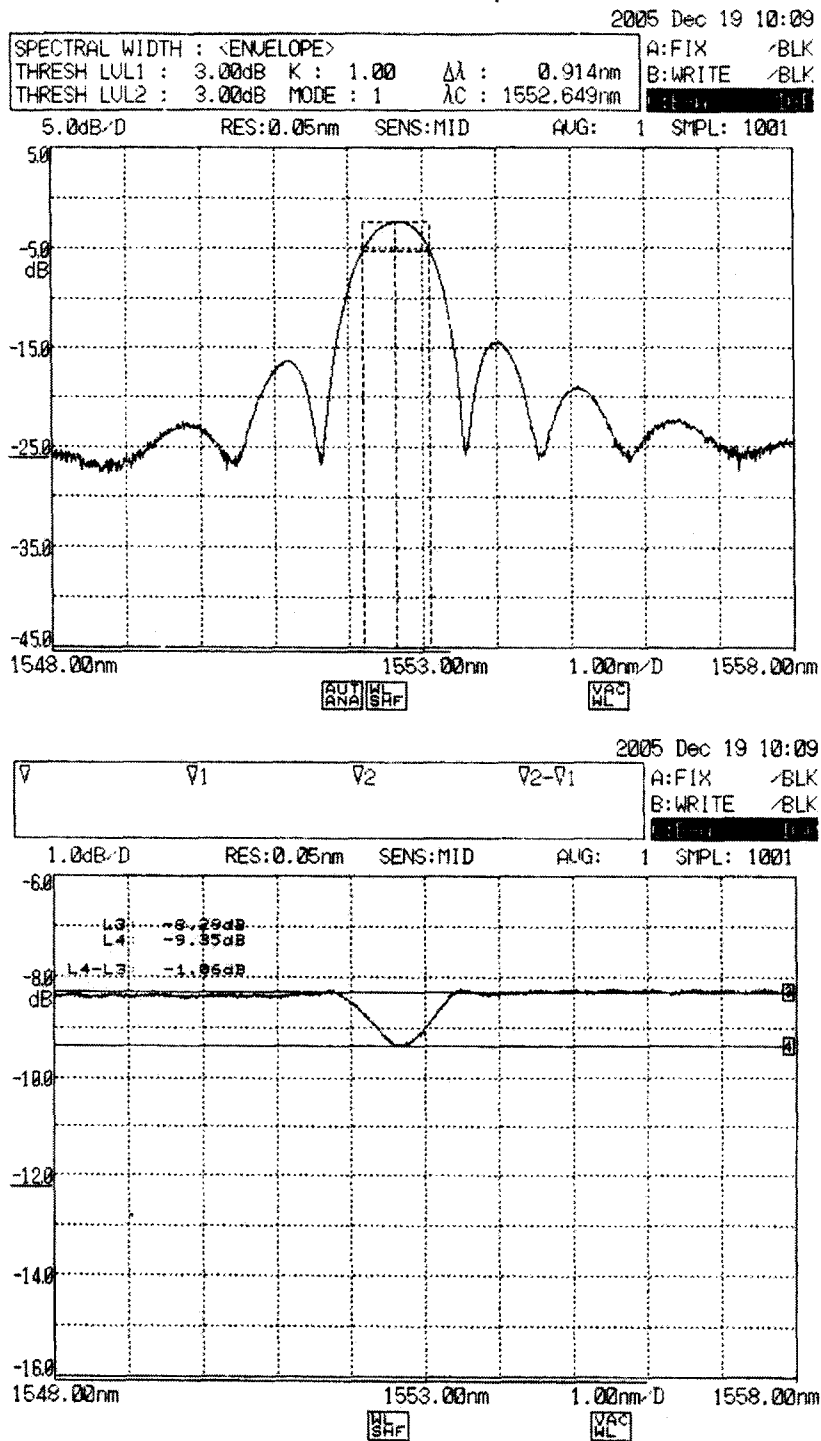


Figure 5.8: The implemented FBG1 reflection (top) and transmission (bottom) characteristics.

5.5 Summary

In this chapter we presented the design and implementation of FBG. This design is based on the laser output characteristics, and the back-reflection level required to drive the laser to operate in feedback Regime V. Analytical formulas used to determine the design parameters were discussed. OptiGrating design software was used to design the desired FBG. Implementation procedures for FBG at CLIPS are presented at the end of chapter.

Chapter 6

DFB Laser Diode with External FBG

In this chapter, a feedback topology is proposed that advantageously applies optical feedback to the DFB laser in order to enable the omission of the isolator without significantly degrading the performance of the DFB laser. The proposed topology is achieved by attaching a FBG to a DFB laser. FBG characteristics were chosen such that the attached DFB laser would be driven to operate in feedback Regime V. Several FBGs have been implemented and a variety of DFB laser modules were used to experimentally determine the DFB laser diode performance when attached to a FBG. Table 6.1 summarizes the different components used in this work along with their affiliated notations.

Notation	Description	Manufacturer
FBG1	FBG with $R = 0.2166$ at $\lambda=1552.649$ nm	CLLIPS
FBG2	FBG with $R = 0.2773$ at $\lambda=1552.698$ nm	CLLIPS
FBG4	FBG with $R = 0.2112$ at $\lambda=1552.653$ nm	CLLIPS
FBG7	FBG with $R = 0.50$ at $\lambda=1553.231$ nm	CLLIPS
FBG10	FBG with $R = 0.25$ at $\lambda=1552.505$ nm	CLLIPS
FBG11	FBG with $R = 0.293$ at $\lambda=1552.83$ nm	Avensys
FBG12	FBG with $R = 0.2897$ at $\lambda=1313.19$ nm	Avensys
DFB1	FLD3F7CZ 1310 nm isolated butterfly DFB laser diode (LD)	Eudyna (Fujitsu)
DFB2	ES/FLD3F7CZ557-MX09081 1310 nm unisolated DFB LD	Eudyna (Fujitsu)
DFB3	ES/FLD3F7CZ557-MX09082 1310 nm unisolated DFB LD	Eudyna (Fujitsu)
DFB4	T13D-PFA2-C1 1310 nm unisolated coaxial DFB LD	Laser Mate
DFB5	T15D-PFA2-C1 1550 nm unisolated coaxial DFB LD	Laser Mate

Table 6.1: Various components used in measurements.

The DFB laser diodes have to be biased properly in order to emit around the central

wavelength of the attached FBG, hence, achieving the back-reflection required for the feedback Regime V operation. The performance of the proposed feedback topology is analyzed in the remainder of this chapter. The spectrum of the DFB laser diode attached to the FBG was examined; the RIN and distortion of the combined configuration was measured. Results of the proposed configuration was also compared to that of the isolated DFB laser.

6.1 Spectrum Stability

Previously reported research discuss using FBGs to force a laser into Regime IV [58]. This regime is mostly applicable to low-speed digital signaling applications and erbium-doped fiber amplifiers pumping. For CATV applications, operation in Regime V is highly recommended. This section will show how the use of an FBG stabilized the intensity and wavelength fluctuations of an unisolated DFB laser. This was due to operation in feedback Regime V.

6.1.1 1550 nm wavelength range

FBG1 was attached to DFB5. The reflection and transmission characteristics of FBG1 are found in Figure 5.8 on page 97. The DFB5 spectrum shows high intensity and wavelength stability with narrow linewidth. This is contributed to the induced optical back-reflections by FBG1. Figure 6.1 on the next page shows the resulting spectrum for a 15 mA bias current.

FBG2 reflection and transmission characteristics are shown in Figure B.7 on page 157. When FBG2 was attached to DFB5 and biased at 15 mA in order to emit around the central wavelength of the FBG2, the resulting output spectrum exhibited a stable narrow linewidth operation. This is shown in Figure 6.2 on the next page.

DFB5 also achieved stable spectra when attached to all other FBGs. These results are shown in Appendix B.

The measured DFB laser spectra shown in Figure 5.2 on page 92 shows that as the bias current increases the laser emission wavelength shifts towards higher values. Optical reflections from FBG reduces the laser threshold level [58], which is equivalent to an increase

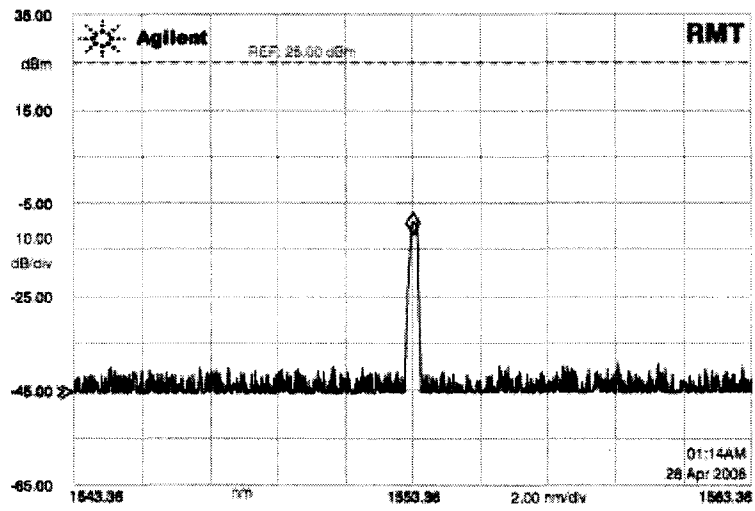


Figure 6.1: Spectrum of DFB5 attached to FBG1 and operating at a bias level of 15 *m.A.*

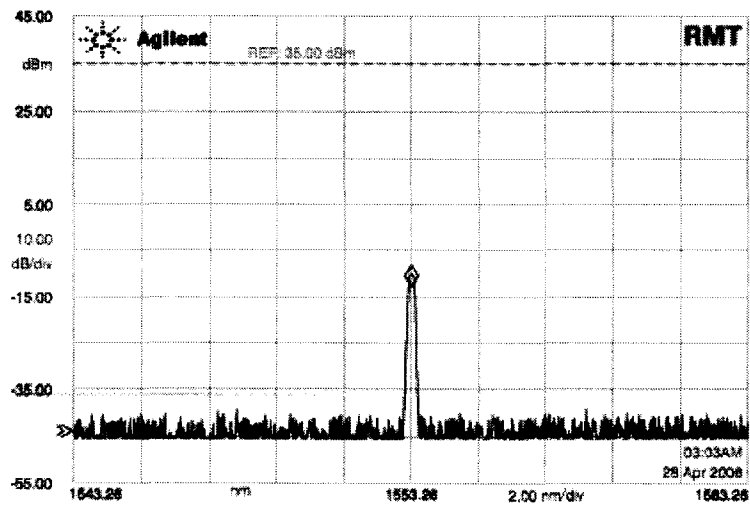


Figure 6.2: Spectrum of DFB5 attached to FBG2 and operating at a bias level of 15 *m.A.*

in the laser's bias current. This can explain why there is a wavelength shift in the laser output when the FBG is attached.

6.1.2 1310 nm wavelength range

FBG12 has been spliced to DFB2 to minimize connector losses as well as improve the coupling efficiency between the laser diode and the FBG. FBG12 shown in Figure B.12 has a peak reflectivity of 0.2897, lies at 1313.19 nm and has a bandwidth (FWHM) of 0.45 nm.

When DFB2 was biased properly to emit at FBG12 peak reflectivity wavelength, that is 1313.19 nm, the reflection was strong enough to drive DFB2 to operate in the stable feedback Regime V as shown in Figure 6.3.

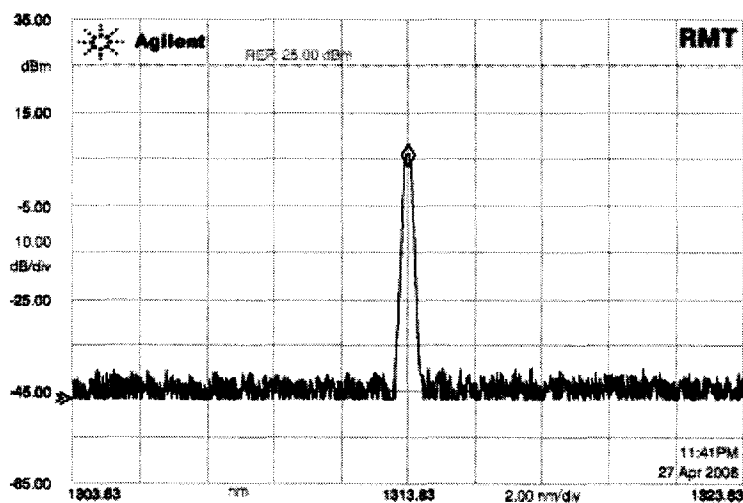


Figure 6.3: Spectrum of DFB2 attached to FBG12 and operating at stable feedback Regime V.

When DFB2 laser was biased to emit at 1313 nm, a strong back-reflection from FBG12 was achieved. However, the level of the back-reflection was less than that required to achieve feedback Regime V operation. Hence, DFB2 was driven to operate in the coherence collapse regime (Regime IV), in which an unstable operation for DFB2 with broadened linewidth was observed. Figure 6.4 on the following page shows the resulting spectrum.

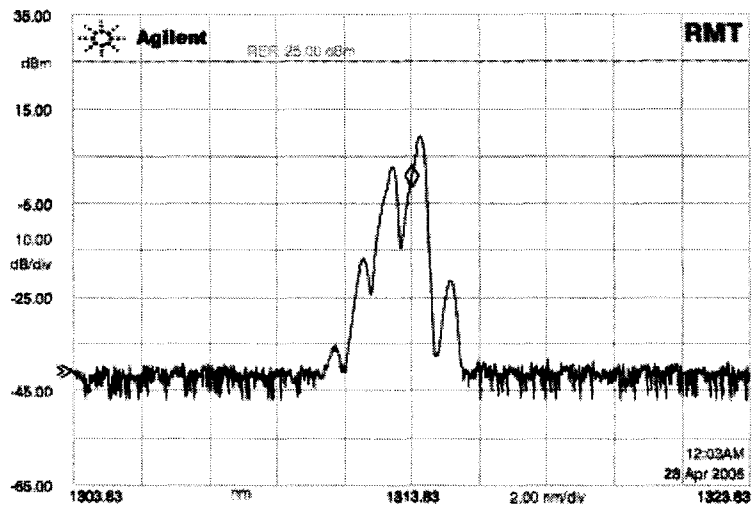


Figure 6.4: Spectrum of DFB2 attached to FBG12 and operating at unstable feedback Regime IV.

6.2 Relative Intensity Noise Measurements

Carrier-to-Noise Ratio (CNR) is defined as the ratio of the carrier to the total noise power in 4 MHz bandwidth. Analog AM-VSB video CATV signals require a CNR near 50 dB for acceptable picture quality. This CNR is much larger than the 20 dB required for digital and FM systems [4]. RIN from the laser is one of the major factors that limits the CNR. Low RIN is highly recommended for the DFB lasers in order to achieve the desired CRN for analog CATV systems. This section shows how low RIN can be achieved by attaching an FBG to the DFB laser diode.

6.2.1 1550 nm wavelength range

Figure 6.5 on the next page shows the measured average RIN of DFB5 biased at 15 mA. Figure 6.6 on the following page shows the measured average RIN of DFB5 attached to a 30 dB optical isolator and biased at the same level. The RIN was measured at 1 GHz frequency offset. Using optical isolator decreases the average RIN from -108.96 dB/Hz to -114.51 dB/Hz.

Figure 6.7 on page 105 shows the measured average RIN of DFB5 biased at 15 mA,

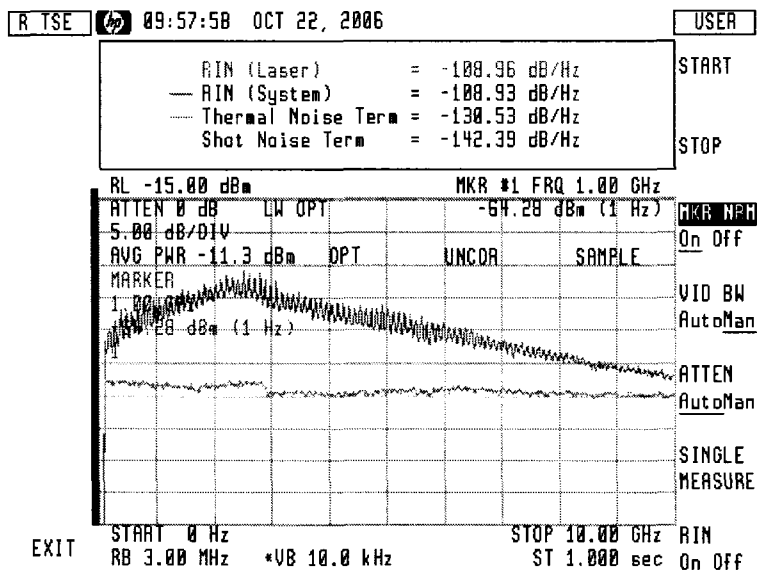


Figure 6.5: Measured average RIN of DFB5 operating at a bias level of 15 mA.

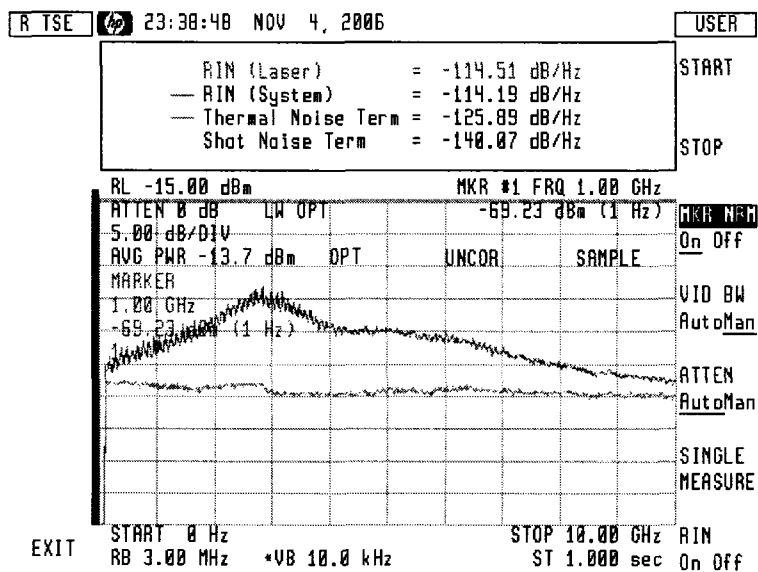


Figure 6.6: Measured average RIN of DFB5 attached to a 30 dB optical isolator, and operating at a bias level of 15 mA.

with FBG10 attached to DFB5. The measured average RIN at a 1 GHz frequency offset is -115.13 dB/Hz.

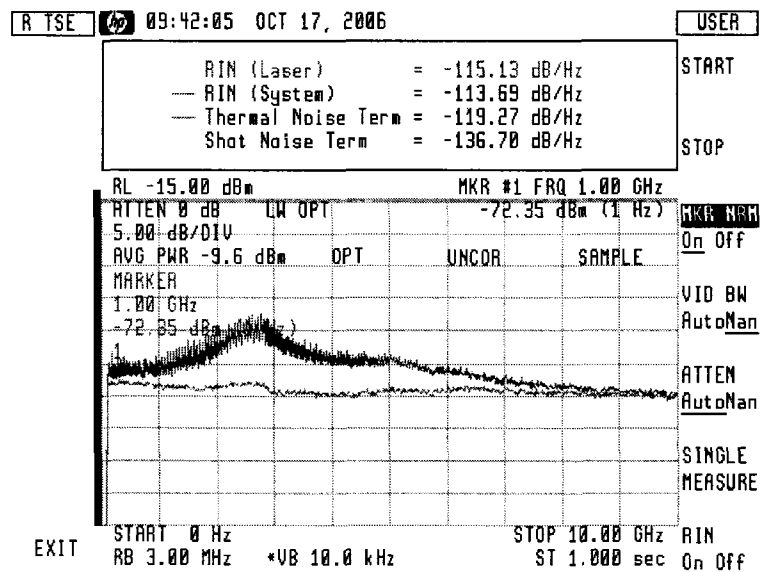


Figure 6.7: Measured average RIN of DFB5 attached to FBG10, and operating at a bias level of 15 mA.

Figure 6.8 on the following page shows the measured average RIN of DFB5 biased at 15 mA, with FBG11 attached to DFB5. The measured average RIN at a 1 GHz frequency was -117.31 dB/Hz. Average RIN measured for DFB5 attached to other FBGs is shown in Appendix B.

Table 6.2 on the next page summarizes the above measured average RIN for the various DFB5 configurations.

Results show that using FBG1, FBG2, or FBG10 improves the unisolated DFB5's RIN by an average of 7 dB/Hz. This improvement is comparable to the improvement obtained using a 30 dB optical isolator. However, using FBG11 achieves better RIN while maintaining the same bias current level.

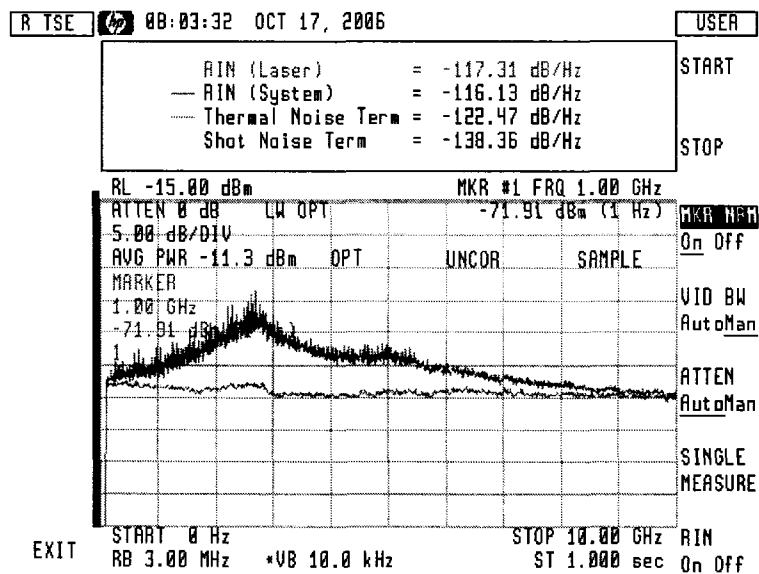


Figure 6.8: Measured average RIN of DFB5 attached to FBG11, and operating at a bias level of 15 mA.

Configuration	FBG reflectivity	measured RIN (dB/Hz)
Unisolated DFB5	-	-108.96
DFB5 with 30-dB isolator	-	-114.51
FBG1 attached to DFB5	0.2166	-114.02
FBG2 attached to DFB5	0.2737	-115.99
FBG10 attached to DFB5	0.25	-115.13
FBG11 attached to DFB5	0.293	-117.31

Table 6.2: Measured average RIN for different DFB5 configurations.

6.2.2 1310 nm wavelength range

Figures 6.9 and 6.10 on the following page respectively show the average RIN measurements for DFB2 attached to FBG12, and for DFB1 with a built-in optical isolator. DFB2 attached to FBG12 achieved an average RIN level of -158.49 dB/Hz. That is comparable to an average RIN level of -157.87 dB/Hz of DFB1 at a 1 GHz frequency offset and same average optical power (i.e. 5.1 dBm) [54].

Two observations are noteworthy. Firstly, although it is known that the laser RIN has its maximum near the relaxation oscillation frequency, this is not witnessed in the measurement plots. This is due to the fact that the relaxation frequency of the laser at this bias level is much more than the stop frequency of the measurement (i.e, 5 GHz). Secondly, the drop that exists at a frequency 2.9 GHz is due to the fact that the Agilent 71400C lightwave signal analyzer uses two different tracking generator modules to cover the full frequency range from 20 Hz to 18 GHz. The first module covers frequencies ranging from 20 Hz to 2.9 GHz, while the second covers frequencies ranging from 2.7 GHz to 18 GHz. The drop that exists at a frequency of 2.9 GHz is due to the transition from the first module to the second.

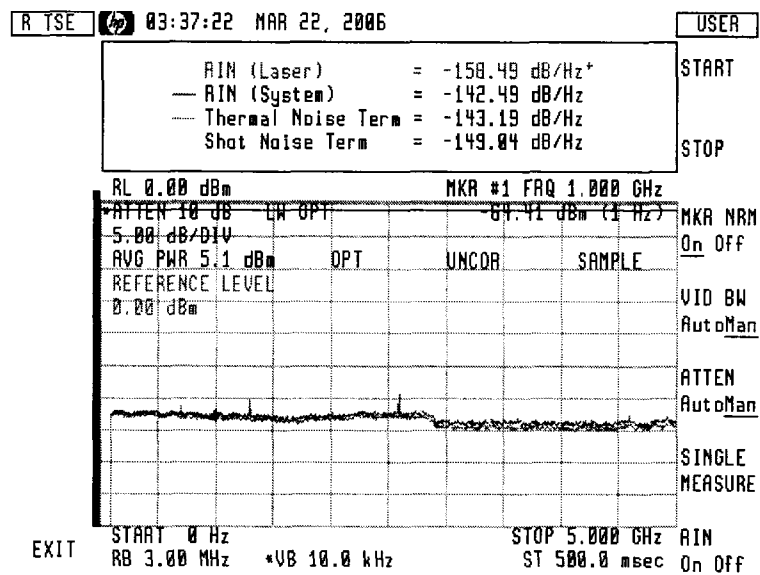


Figure 6.9: Measured RIN of DFB2 attached to FBG12.

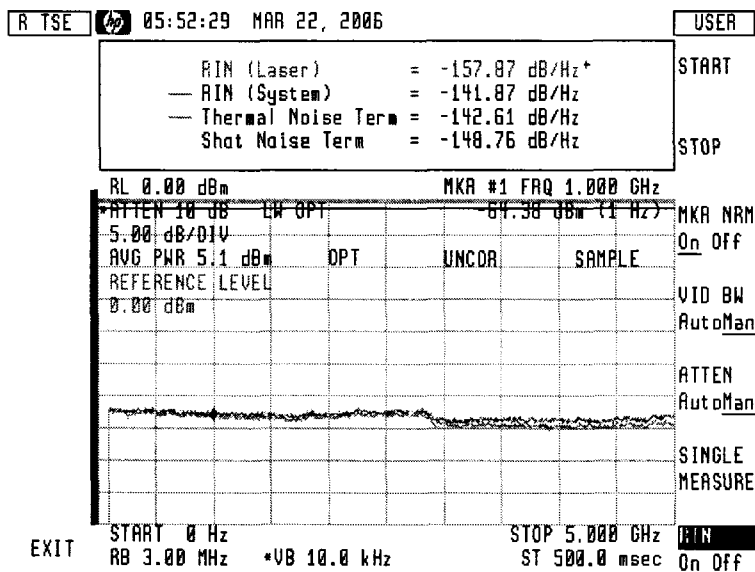


Figure 6.10: Measured RIN for DFB1.

6.3 Distortion Measurements

In addition to the high CNR recommended for analog CATV systems, low CSO and CTB are also desirable in order to achieve high analog CATV signal quality. CSO is defined as the ratio of the carrier to the total power within the largest accumulation of second-order distortion products within each channel. CTB is similarly defined as the ratio of carrier to total power within the largest accumulation of third-order distortion products within each channel. This section shows how attaching a FBG to a DFB laser affects the second and third order harmonic distortions of the DFB laser.

6.3.1 1550 nm wavelength range

Figures 6.11 to 6.14 on page 111 show the measured distortion of DFB5 attached to various tested FBGs as a function of bias current. Measured distortion for DFB5 both with and without an isolator were also included on the figures for the sake of comparison. Distortion measurement results for the other tested FBGs are included in Appendix B.

Figure 6.11 shows the measured second order harmonic distortion for FBG1 attached to DFB5 operating at a carrier frequency of 500 MHz and a power of 0 dBm. Figure 6.12 shows the results of the third-order harmonic distortion for the same setup.

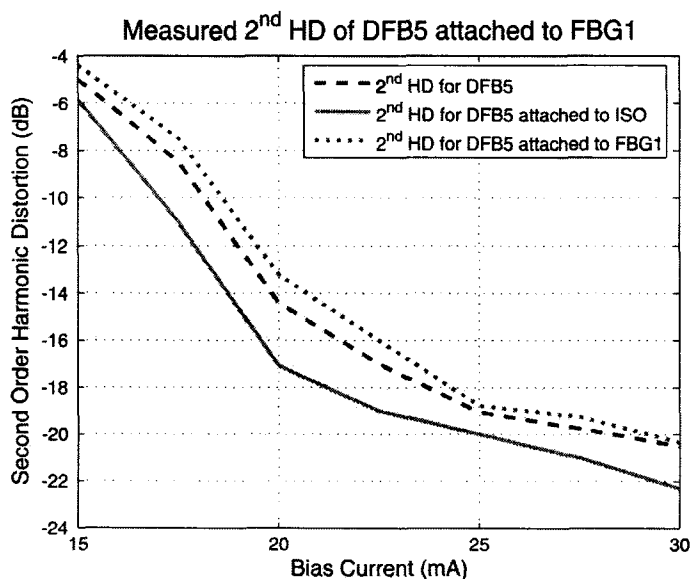


Figure 6.11: Measured second order harmonic distortion of FBG1 attached to DFB5 normalized to the fundamental frequency .

Figure 6.13 and Figure 6.14 on page 111 show the measured second and third order harmonic distortions for FBG2 attached to DFB5 operating at a carrier frequency of 500 MHz and a power of 0 dBm.

Results demonstrate that both second and third order harmonic distortions are decreasing functions of the bias current. Moreover, compared to isolated DFB laser, using FBGs increases both second and third order harmonic distortions by less than 5 dB compared to the isolated DFB. The above results are summarized in Table 6.3 on page 111.

6.3.2 1310 nm wavelength range

Figure 6.15 on page 112 and Figure 6.16 on page 113 show the measured distortions as a function of the bias current for FBG12 attached to DFB2.

Figure 6.15 on page 112 shows the measured second order harmonic distortions for

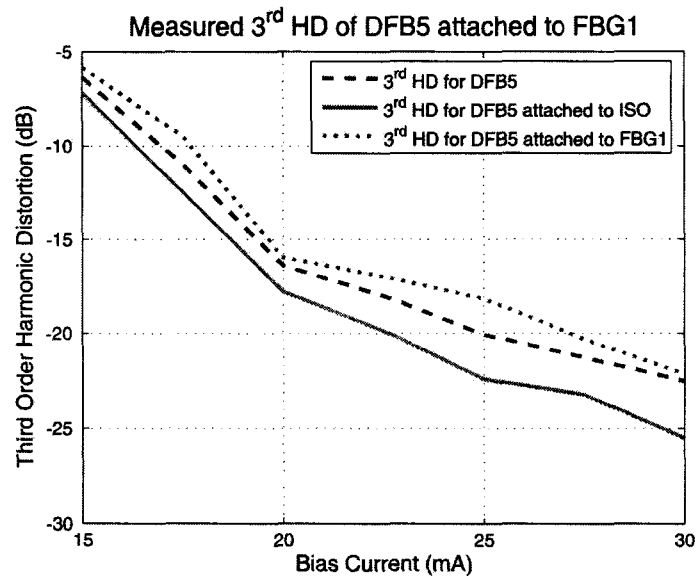


Figure 6.12: Measured third order harmonic distortion of FBG1 attached to DFB5 normalized to the fundamental frequency.

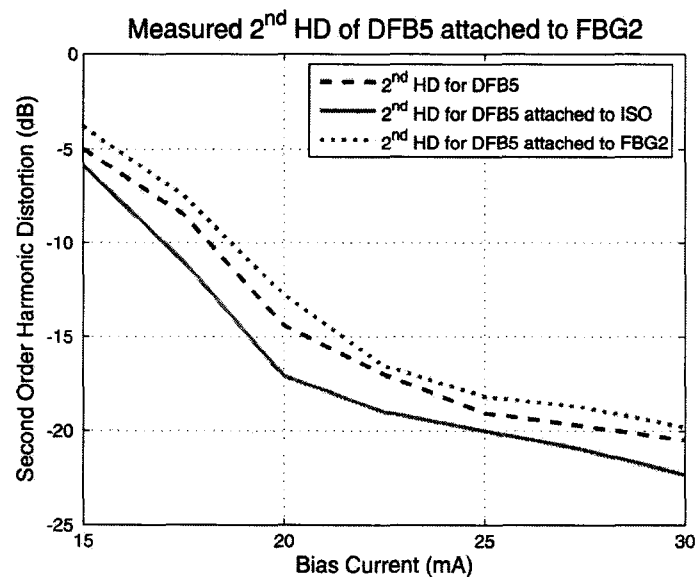


Figure 6.13: Measured second order harmonic distortion of FBG2 attached to DFB5 normalized to the fundamental frequency.

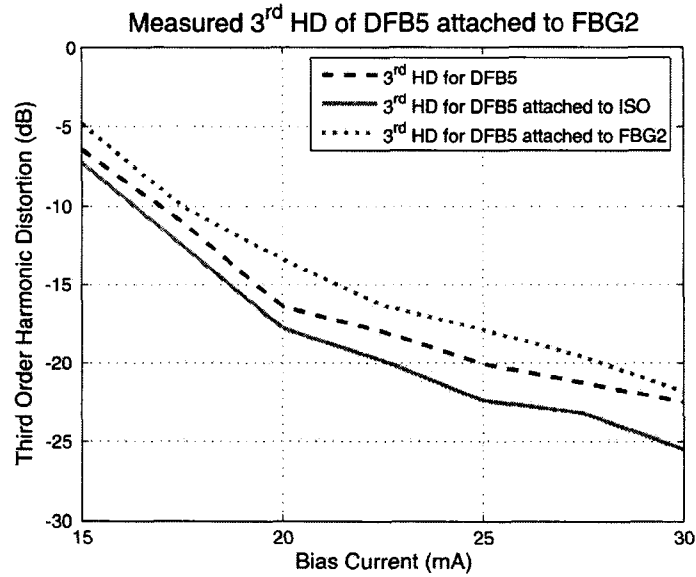


Figure 6.14: The measured third order harmonic distortion of FBG2 attached to DFB5 normalized to the fundamental frequency.

Configuration	FBG reflectivity	2 nd HD (dB)	3 rd HD (dB)
Unisolated DFB5	-	-19.06	-20.06
DFB5 with 30-dB isolator	-	-20	-22.01
FBG1 attached to DFB5	0.2166	-18.78	-18.15
FBG2 attached to DFB5	0.2737	-18.17	-17.87
FBG4 attached to DFB5	0.2112	-17.8	-19.7
FBG7 attached to DFB5	0.50	-17.1	-19.7
FBG10 attached to DFB5	0.25	-18.4	-19.5
FBG11 attached to DFB5	0.293	-18.4	-19.1

Table 6.3: Measured distortion for various DFB5 configurations (bias current=25 mA).

FBG12 attached to DFB2 operating at a carrier frequency of 500 MHz and a power of 0 dBm. Figure 6.16 on the following page shows the measured third order harmonic distortion. Equivalent measurements for DFB1 were included in the figures for comparison purposes.

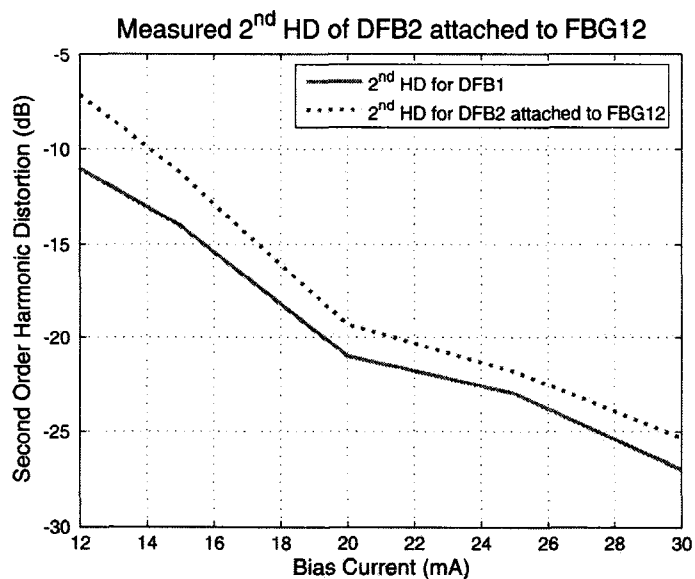


Figure 6.15: Measured second order harmonic distortion of DFB2 attached to FBG12 normalized to the fundamental frequency.

These results show that both second and third order harmonic distortion are decreasing functions of the bias current. Moreover, using FBGs has slightly increased the lasers' distortions.

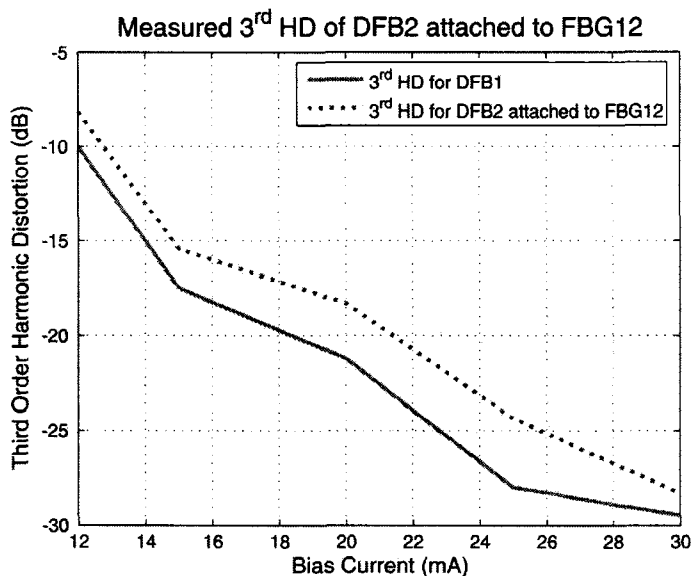


Figure 6.16: Measured third order harmonic distortion of DFB2 attached to FBG12 normalized to the fundamental frequency.

6.4 Summary

Using FBG stabilizes DFB lasers and improve their RIN. All tested DFB laser diodes showed a stable spectrum, low RIN, and narrow linewidth output when attached to the implemented FBGs. Performance of DFB lasers attached to appropriate FBGs were comparable to that of isolated DFB lasers. When feedback Regime V operation is reached, increasing FBG reflectivity decreases the RIN. However, this may come at the expense of lower output optical power. Furthermore, including a FBG has increased the DFB lasers' distortions by around 3 dB compared to isolated DFB lasers. Lasers' nonlinearity compensation will be discussed in detail in Chapter 7.

Using optical isolator can improve the unisolated laser noise and linearity performance, on the other hand it increases cost and complicate the construction of the laser module. Extra time is required to optically align the isolator, additionally it cannot guarantee complete removal for the optical back-reflections. In this chapter we showed that using an unisolated DFB laser attached to a FBG and operating in feedback Regime V achieves noise and linearity performance that is comparable to that of the isolated DFB laser.

Chapter 7

Inverse Laser Model Including Feedback Derivation and Modeling

7.1 Introduction

The laser is a non-linear system; it produces both even and odd order harmonic distortion. To meet the restrictions imposed on the DFB lasers for analog CATV systems, the laser's distortion should be kept at a minimum. Fabrication of high linearity laser is an expensive task and requires extensive screening that may result in low yields. The other alternative is to use one of the linearization techniques. Several linearization techniques were reviewed in [19] these included: optical feedback and optical feed-forward [59–63], post-distortion [64–66], pre-distortion [67–72], adaptive pre-distortion [73–76], external light injection [77], and cascaded linearized modulator [78]. The analysis made in [19] in terms of performance, cost, and suitability for analog CATV systems supported the use of pre-distortion techniques.

In this chapter a laser pre-distorter will be developed based on the inverse laser Volterra model including feedback effect. The rate equations that describing the original laser model will be algebraically manipulated in order to get the laser driving current as a function of the laser output power, then third order Volterra transfer functions will be extracted from these equations representing the pre-distorter Volterra model. The third order pre-distorter Volterra model will be implemented in ADS and cascaded to the original laser model to reduce the overall distortion and hence keep the Composite Second Order (CSO) and Composite Triple Beat (CTB) at lower levels.

7.2 Inverse Laser Model Including Feedback Derivation

When the distortion is frequency dependent in a non-linear system, the nonlinearity can be represented by a Volterra functional series (a power series with memory) [79,80], instead of a Taylor series (a power series without memory). The coefficients will be extracted using Volterra transfer functions in order to determine the laser inverse function by deriving the Volterra series of $I = f(P)$, where I is the injection current, and P is the photon density.

The laser diode rate equations including feedback term are given by the following two relations:

$$\frac{dP_n(t)}{dt} = \frac{(C_n(t) - C_{tr}^n)}{\tau_{ph}(1 - C_{tr}^n)} \frac{P_n(t)}{\sqrt{1 + P_r^n}} - \frac{P_n(t)}{\tau_{ph}} + \beta_{sp} C_n(t) + \frac{2}{\tau_L} \kappa_{ext} P_n(t) \cos(\omega_{th} \tau_{ext}) \quad (7.2.1)$$

and

$$\frac{dC_n(t)}{dt} = \frac{I(t)}{qV_c C_{th}} - \frac{(C_n(t) - C_{tr}^n)}{\tau_e \tau_{ph}(1 - C_{tr}^n)} \frac{P_n(t)}{\sqrt{1 + P_r^n}} - \frac{C_n(t)}{\tau_e} \quad (7.2.2)$$

The different parameters of (7.2.1) and (7.2.2) were defined in the Chapter 3. To get $I = f(P)$ the laser diode rate equations should be denormalized and algebraically manipulated. From (7.2.1) the carrier density is given as,

$$C = \frac{\frac{dP}{dt} + \frac{P}{\tau_{ph}} + \frac{GC_{tr}P}{\sqrt{1+P/P_s}} - \frac{2}{\tau_L} \kappa_{ext} P \cos(\omega_{th} \tau_{ext})}{\frac{\Gamma \beta_{sp}}{\tau_e} + \frac{GP}{\sqrt{1+P/P_s}}} \quad (7.2.3)$$

Expressing P and C in terms of their DC and AC components, i.e, $P = P_{dc} + P_{ac}$ and $C = C_{dc} + C_{ac}$ in (7.2.3) yields,

$$C_{dc} + C_{ac} = \frac{P' + \frac{(P_{dc} + P_{ac})}{\tau_{ph}} + \frac{GC_{tr}(P_{dc} + P_{ac})}{\sqrt{1+(P_{dc} + P_{ac})/P_s}} - \frac{2}{\tau_L} \kappa_{ext} (P_{dc} + P_{ac}) \cos(\omega_{th} \tau_{ext})}{\frac{\Gamma \beta_{sp}}{\tau_e} + \frac{G(P_{dc} + P_{ac})}{\sqrt{1+(P_{dc} + P_{ac})/P_s}}} \quad (7.2.4)$$

Let $\Phi = \frac{1}{\sqrt{1+(P_{dc} + P_{ac})/P_s}}$ and $\Psi = \frac{1}{co + G(P_{dc} + P_{ac})\Phi}$, where $co = \frac{\Gamma \beta_{sp}}{\tau_e}$. Expanding Φ and Ψ up to the third order using Taylor series such that:

$$\Phi = M0 + M1 P_{ac} + M2 P_{ac}^2 + M3 P_{ac}^3 \quad (7.2.5)$$

and

$$\Psi = D0 + D1 P_{ac} + D2 P_{ac}^2 + D3 P_{ac}^3 \quad (7.2.6)$$

The following Taylor series coefficients were extracted using Mathematica.

$$M0 = \frac{1}{\sqrt{1 + P_{dc}/P_s}} \quad (7.2.7)$$

$$M1 = -\frac{1}{2(1 + (P_{dc}/P_s)^{3/2}P_s)} \quad (7.2.8)$$

$$M2 = \frac{1}{8(1 + P_{dc}/P_s)^{5/2}P_s^2} \quad (7.2.9)$$

$$M3 = -\frac{1}{16(1 + P_{dc}/P_s)^{7/2}P_s^3} \quad (7.2.10)$$

$$D0 = \frac{1}{co + GM0P_{dc}} \quad (7.2.11)$$

$$D1 = -\frac{GM0 + GM1P_{dc}}{(co + GM0P_{dc})^2} \quad (7.2.12)$$

$$D2 = \frac{1}{2} \left(\frac{2(GM0 + GM1P_{dc})^2}{(co + GM0P_{dc})^3} - \frac{2GM1 + 2GM2P_{dc}}{(co + GM0P_{dc})^2} \right) \quad (7.2.13)$$

$$D3 = \frac{1}{6} \left(-\frac{6(GM0 + GM1P_{dc})^3}{(co + GM0P_{dc})^4} + \frac{6(GM0 + GM1P_{dc})(2GM1 + 2GM2P_{dc})}{(co + GM0P_{dc})^3} - \frac{6GM2 + 6GM3P_{dc}}{(co + GM0P_{dc})^2} \right) \quad (7.2.14)$$

Substitution of (7.2.5) and (7.2.6) into (7.2.4) gives the carrier density and its derivative as,

$$(C_{dc} + C_{ac}) = Z0 + Z1P_{ac} + Z2P'_{ac} + Z3P_{ac}^2 + Z4P_{ac}P'_{ac} + Z5P_{ac}^3 + Z6P_{ac}^2P'_{ac} + Z7P_{ac}^3P'_{ac} \quad (7.2.15)$$

$$C'_{ac} = Z1P'_{ac} + Z2P''_{ac} + 2Z3P_{ac}P'_{ac} + Z4(P'_{ac})^2 + Z4P_{ac}P''_{ac} + 3Z5P_{ac}^2P'_{ac} + 2Z6P_{ac}(P'_{ac})^2 + Z6P_{ac}^2P''_{ac} + 3Z7P_{ac}^2(P'_{ac})^2 + Z7P_{ac}^3P''_{ac} \quad (7.2.16)$$

where,

$$Z0 = C_{tr} D0 G M0 P_{dc} + \frac{D0P_{dc}}{\tau_{ph}} - \frac{2D0\kappa_{ext}P_{dc} \sin(\omega_{th}\tau_{ext})}{\tau_l} \quad (7.2.17)$$

$$Z1 = C_{tr} D0 G M0 + C_{tr} D1 G M0 P_{dc} + C_{tr} D0 G M1 P_{dc} + \frac{D0}{\tau_{ph}} + \frac{D1 P_{dc}}{\tau_{ph}} - \frac{2D0\kappa_{ext} \sin(\omega_{th}\tau_{ext})}{\tau_l} - \frac{2D1\kappa_{ext}P_{dc} \sin(\omega_{th}\tau_{ext})}{\tau_l} \quad (7.2.18)$$

$$Z2 = D0 \quad (7.2.19)$$

$$Z3 = C_{tr} D1 G M0 + C_{tr} D0 G M1 + C_{tr} D2 G M0 P_{dc} + C_{tr} D1 G M1 P_{dc} + C_{tr} D0 G M2 P_{dc} + \frac{D1}{\tau_{ph}} + \frac{D2P_{dc}}{\tau_{ph}} - \frac{2D1\kappa_{ext} \sin(\omega_{th}\tau_{ext})}{\tau_l} - \frac{2D2\kappa_{ext}P_{dc} \sin(\omega_{th}\tau_{ext})}{\tau_l} \quad (7.2.20)$$

$$Z4 = D1 \quad (7.2.21)$$

$$\begin{aligned}
Z5 = & C_{tr}D2 G M0 + C_{tr}D1 G M1 + C_{tr}D0 G M2 + C_{tr}D3 G M0 P_{dc} \\
& + C_{tr}D2 G M1 P_{dc} + C_{tr}D1 G M2 P_{dc} + C_{tr}D0 G M3 P_{dc} \\
& + \frac{D2}{\tau_{ph}} + \frac{D3P_{dc}}{\tau_{ph}} - \frac{2D2\kappa_{ext} \sin(\omega_{th}\tau_{ext})}{\tau_l} - \frac{2D3\kappa_{ext}P_{dc} \sin(\omega_{th}\tau_{ext})}{\tau_l}
\end{aligned} \tag{7.2.22}$$

$$Z6 = D2 \tag{7.2.23}$$

$$Z7 = D3 \tag{7.2.24}$$

Substitution of (7.2.5) to (7.2.24) into (7.2.2) gives the modulation current as,

$$I_{ac} = -I_{dc} + qV_c \left[C'_{ac} + \frac{C_{ac} + C_{dc}}{\tau_e} + g_m ((C_{ac} + C_{dc}) - C_{tr}) \Phi(P_{ac} + P_{dc}) \right] \tag{7.2.25}$$

Where $g_m = G/\Gamma$. Substitution of (7.2.5), (7.2.15), and (7.2.16) into (7.2.25) and considering terms up to the third order gives,

$$\begin{aligned}
I_{ac} = & K \\
& + \{m_0P_{ac} + m_1P'_{ac} + m_2P''_{ac}\} \\
& + \{m_3P_{ac}^2 + m_4P_{ac}P'_{ac} + m_5(P'_{ac})^2 + m_5P_{ac}P''_{ac}\} \\
& + \{m_6P_{ac}^3 + m_7P_{ac}^2P'_{ac} + 2m_8P_{ac}(P'_{ac})^2 + m_8P_{ac}^2P''_{ac}\}
\end{aligned} \tag{7.2.26}$$

The laser's inverse model is represented by the input-output relation given by (7.2.26). The first row is a constant. The second, third and fourth rows will be used to extract the first, second, and third order Volterra transfer functions respectively. The constants m_0 to m_8 have been calculated using Mathematica.

$$\begin{aligned}
m_0 = & -C_{tr}g_mM0qV_c - C_{tr}g_mM1P_{dc}qV_c + g_mM0qV_cZ0 \\
& + g_mM1P_{dc}qV_cZ0 + g_mM0P_{dc}qV_cZ1 + \frac{qV_cZ1}{\tau_e}
\end{aligned} \tag{7.2.27}$$

$$m_1 = qV_c Z1 + g_m M0 P_{dc} qV_c Z2 + \frac{qV_c Z2}{\tau_e} \quad (7.2.28)$$

$$m_2 = qV_c Z2 \quad (7.2.29)$$

$$\begin{aligned} m_3 = & -C_{tr} g_m M1 qV_c - C_{tr} g_m M2 P_{dc} qV_c + g_m M1 qV_c Z0 + g_m M2 P_{dc} qV_c Z0 \\ & + g_m M0 qV_c Z1 + g_m M1 P_{dc} qV_c Z1 + g_m M0 P_{dc} qV_c Z3 + \frac{qV_c Z3}{\tau_e} \end{aligned} \quad (7.2.30)$$

$$m_4 = g_m M0 qV_c Z2 + g_m M1 P_{dc} qV_c Z2 + 2qV_c Z3 + g_m M0 P_{dc} qV_c Z4 + \frac{qV_c Z4}{\tau_e} \quad (7.2.31)$$

$$m_5 = qV_c Z4 \quad (7.2.32)$$

$$\begin{aligned} m_6 = & -C_{tr} g_m M2 qV_c - C_{tr} g_m M3 P_{dc} qV_c + g_m M2 qV_c Z0 + g_m M3 P_{dc} qV_c Z0 + g_m M1 qV_c Z1 \\ & + g_m M2 P_{dc} qV_c Z1 + g_m M0 qV_c Z3 + g_m M1 P_{dc} qV_c Z3 + g_m M0 P_{dc} qV_c Z5 + \frac{qV_c Z5}{\tau_e} \end{aligned} \quad (7.2.33)$$

$$\begin{aligned} m_7 = & g_m M1 qV_c Z2 + g_m M2 P_{dc} qV_c Z2 + g_m M0 qV_c Z4 + g_m M1 P_{dc} qV_c Z4 \\ & + 3qV_c Z5 + g_m M0 P_{dc} qV_c Z6 + \frac{qV_c Z6}{\tau_e} \end{aligned} \quad (7.2.34)$$

$$m_8 = qV_c Z6 \quad (7.2.35)$$

7.2.1 Volterra Series

The Volterra series technique is used to calculate and analyze the distortion terms in non-linear electronic elements. The inverse semiconductor laser model is obtained by considering the laser as a non-linear system with an input of $P(t)$ and an output of $I(t)$. Using Volterra series [81], the system output is given by:

$$\begin{aligned}
 I(t) = & \int_{-\infty}^{+\infty} g_1(\tau_1)P(t - \tau_1)d\tau_1 + \int_{-\infty}^{\infty} \int_{-\infty}^{\infty} g_2(\tau_1, \tau_2)P(t - \tau_1)P(t - \tau_2)d\tau_1d\tau_2 \\
 & + \int_{-\infty}^{+\infty} \int_{-\infty}^{+\infty} \int_{-\infty}^{+\infty} g_3(\tau_1, \tau_2, \tau_3)P(t - \tau_1)P(t - \tau_2)P(t - \tau_3)d\tau_1d\tau_2d\tau_3 + \dots \\
 & + \int_{-\infty}^{+\infty} \int_{-\infty}^{+\infty} \dots \int_{-\infty}^{+\infty} g_n(\tau_1, \tau_2, \dots, \tau_n)P(t - \tau_1)P(t - \tau_2)\dots P(t - \tau_n)d\tau_1d\tau_2\dots d\tau_n + \dots
 \end{aligned} \tag{7.2.36}$$

where $g_n(\tau_1, \tau_2, \dots, \tau_n) = 0$ for any $\tau_m < 0, m = 1, 2, \dots, n, n = 1, 2, \dots$. The series in the previous equation is called a Volterra series and the functions $g_n(\tau_1, \tau_2, \dots, \tau_n)$ are called the Volterra kernels of the system.

The above equation can be also expressed as,

$$I(t) = G_1 [(P(t))] + G_2 [(P(t))] + G_3 [(P(t))] + \dots + G_n [(P(t))] + \dots \tag{7.2.37}$$

where G_n , is the n^{th} -order Volterra operator and is given by the following integral,

$$G_n [(P(t))] = \int_{-\infty}^{\infty} \dots \int_{-\infty}^{\infty} g_n(\tau_1, \dots, \tau_n)P(t - \tau_1)\dots P(t - \tau_n)d\tau_1\dots d\tau_n \tag{7.2.38}$$

7.2.2 Extraction of Volterra Transfer Functions

Harmonic-input method

The harmonic-input method is used to determine the kernels G_k in the frequency domain. Considering the equation describing I_{ac} as a function of P_{ac} given by (7.2.26). When k

input tones (at the frequencies $\omega_1, \dots, \omega_k$) are applied to the laser model, they have the following form,

$$P_{ac} = P_{dc}(e^{j\omega_1 t} + e^{j\omega_2 t} + \dots + e^{j\omega_k t}) \quad (7.2.39)$$

When one tone input, $P_{ac} = P_{dc}e^{j\omega_1 t}$, is applied to the system described by (7.2.26), the first order Volterra transfer function is the coefficient of $e^{j\omega_1 t}$ and is given by,

$$G_1(\omega_1) = (m_0 + jm_1\omega_1 - m_2\omega_1^2) P_{dc} \quad (7.2.40)$$

The second order Volterra transfer function is obtained if two tone inputs, $P_{ac} = P_{dc}e^{j\omega_1 t} + P_{dc}e^{j\omega_2 t}$, are applied to (7.2.26). The coefficient of $e^{j(\omega_1+\omega_2)t}$ represents the second order Volterra transfer function and is given by,

$$G_2(\omega_1, \omega_2) = (2m_3 + jm_4(\omega_1 + \omega_2) - m_5(\omega_1 + \omega_2)^2) P_{dc}^2 \quad (7.2.41)$$

If three tone inputs, $P_{ac} = P_{dc} e^{j\omega_1 t} + P_{dc} e^{j\omega_2 t} + P_{dc} e^{j\omega_3 t}$, are applied to (7.2.26), the third order Volterra transfer function is the coefficient of $e^{j(\omega_1+\omega_2+\omega_3)t}$ and is given by,

$$G_3(\omega_1, \omega_2, \omega_3) = (6m_6 + 2jm_7(\omega_1 + \omega_2 + \omega_3) - 2m_8(\omega_1 + \omega_2 + \omega_3)^2) P_{dc}^3 \quad (7.2.42)$$

Equations (7.2.40) to (7.2.42) represent the laser inverse model frequency domain Volterra transfer functions.

Direct expansion method

The direct expansion method is used to derive the time domain laser inverse model from the frequency domain model. Equations (7.2.40) to (7.2.42) can be represented by their Laplace transforms easily by replacing each $j\omega$ by s as follows,

$$G_1(s_1) = (m_0 + m_1s_1 + m_2s_1^2) P_{dc} \quad (7.2.43)$$

$$G_2(s_1, s_2) = (2m_3 + m_4(s_1 + s_2) + m_5(s_1 + s_2)^2) P_{dc}^2 \quad (7.2.44)$$

$$G_3(s_1, s_2, s_3) = (6m_6 + 2m_7(s_1 + s_2 + s_3) + 2m_8(s_1 + s_2 + s_3)^2) P_{dc}^3 \quad (7.2.45)$$

Applying the inverse Laplace transformation to (7.2.43) to (7.2.45) to get their equivalents in the time domain as,

$$G_1[P(t)] = m_0 P(t) + m_1 \frac{dP(t)}{dt} + m_2 \frac{d^2 P(t)}{dt^2} \quad (7.2.46)$$

$$G_2[P(t)] = 2m_3 P^2(t) + m_4 \frac{d(P^2(t))}{dt} + m_5 \frac{d^2(P^2(t))}{dt^2} \quad (7.2.47)$$

$$G_3[P(t)] = 6m_6 P^3(t) + 2m_7 \frac{d(P^3(t))}{dt} + 2m_8 \frac{d^2(P^3(t))}{dt^2} \quad (7.2.48)$$

Equations (7.2.46) to (7.2.48) represent the laser inverse model in time domain. The complete third order time domain Volterra system of the pre-distorter is illustrated in Figure 7.1 on the next page.

An amplifier with gain m_0 was used to represent the first term of (7.2.46), the second term was represented by an amplifier with gain m_1 and a differentiator, and the third term was represented by an an amplifier with gain m_2 and two differentiators.

Equation (7.2.47) was represented by an amplifier with gain $2m_3$ for the first term, an amplifier with gain m_4 and a differentiator for the second term, and an amplifier with gain m_5 and two differentiators for the third term.

First term of (7.2.48) was represented by an amplifier with gain $6m_6$, second term was represented by an amplifier with gain $2m_7$ and a differentiator, and the third term was represented by an amplifier with gain $2m_8$ and two differentiators.

The constants m_0 to m_8 are functions of the laser parameters. The laser parameters are sensitive to thermal effects and aging, which requires the pre-distorter coefficients to

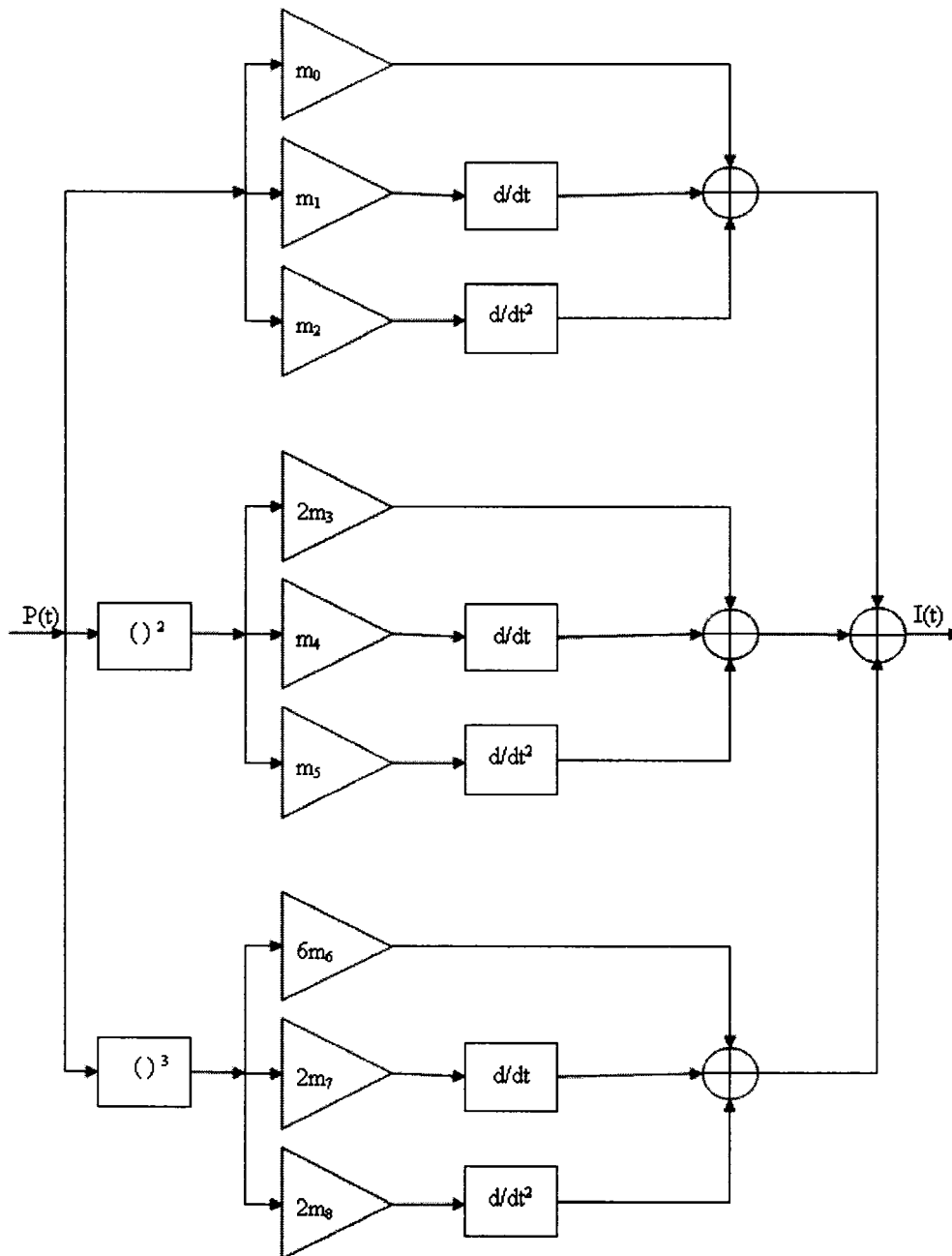


Figure 7.1: Block diagram of the laser inverse model.

be adjusted accordingly in order to compensate for these changes in the laser parameters. This addresses the need for an efficient way to sense the laser output and give feedback to the pre-distorter with these changes to modify its coefficients. Adaptive pre-distorters can monitor the lasers output and update the pre-distorter coefficients and compensate for any of the lasers' time-varying changes.

7.3 Inverse Laser Model Including Feedback Implementation

The above pre-distorter model was implemented in ADS using three branches, each branch containing two dual-port SDDs representing equations (7.2.46), (7.2.47), and (7.2.48) respectively. Figure 7.2 on the following page shows the proposed pre-distorter implementation in ADS.

The setup shown in Figure 7.3 on page 126 is used to predict the ability of the proposed pre-distorter to reduce the harmonic distortions of the laser, the implemented pre-distorter was cascaded to the laser model and compared to the same laser model without a pre-distorter. To examine the improvement of the second and the third harmonic distortions due to the existence of the pre-distorter, the frequency of a single tone input was swept up to 4 GHz, the second and the third harmonic distortions with and without using the pre-distorter were simulated for 0.10 and 0.25 modulation index.

Figure 7.4 on page 127 shows the simulated second harmonic distortion with and without using the pre-distorter for 0.10 and 0.25 modulation index. The results showed that an improvement up to 30 dB (for 0.25 modulation index) and 45 dB (for 0.10 modulation index) over bandwidth around 3 GHz, between 1 GHz and 4 GHz, can be achieved using the proposed pre-distorter.

Figure 7.5 on page 127 shows the simulated third harmonic distortion with and without using the pre-distorter for for 0.10 and 0.25 modulation index. The results showed that an improvement up to 40 dB (for 0.25 modulation index) and 55 dB (for 0.10 modulation index) over bandwidth around 3 GHz, from 1 GHz to 4 GHz, can be achieved using the proposed pre-distorter.

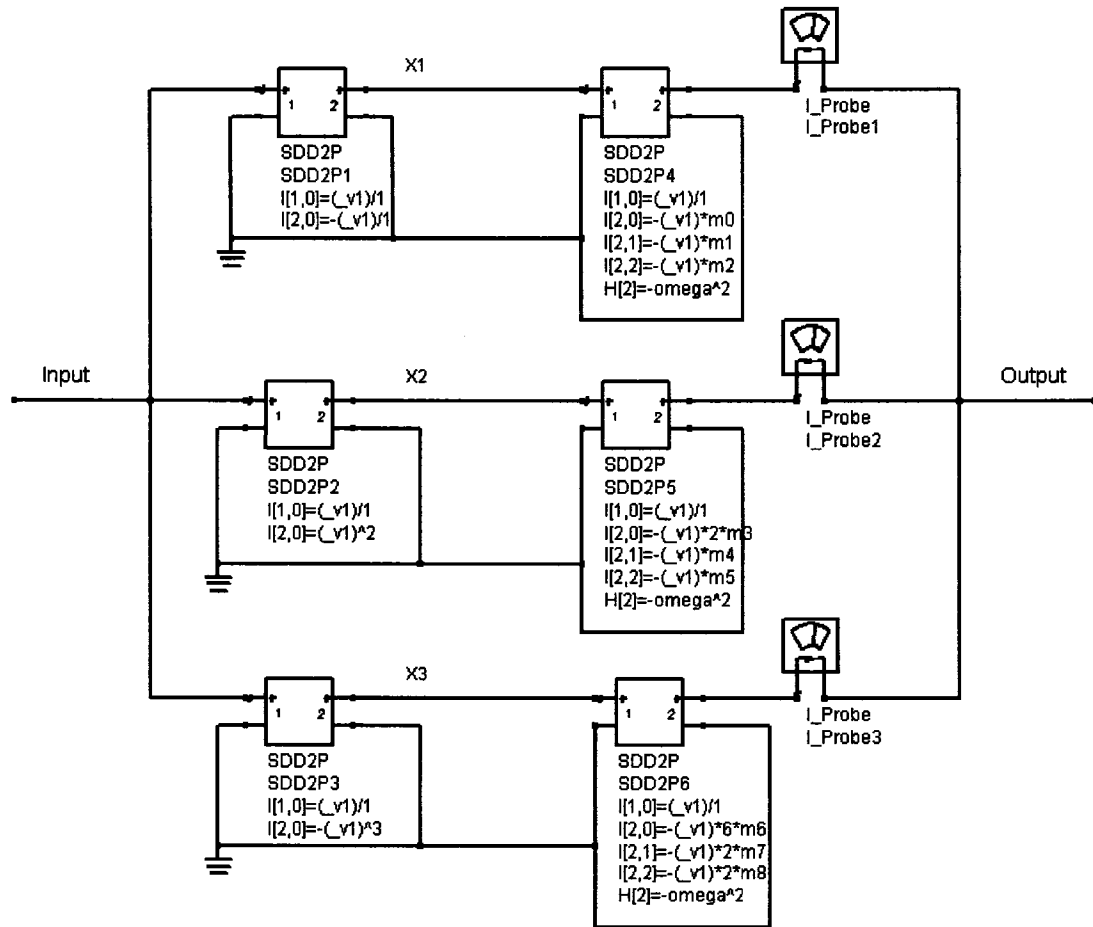


Figure 7.2: ADS implementation of the laser inverse model.

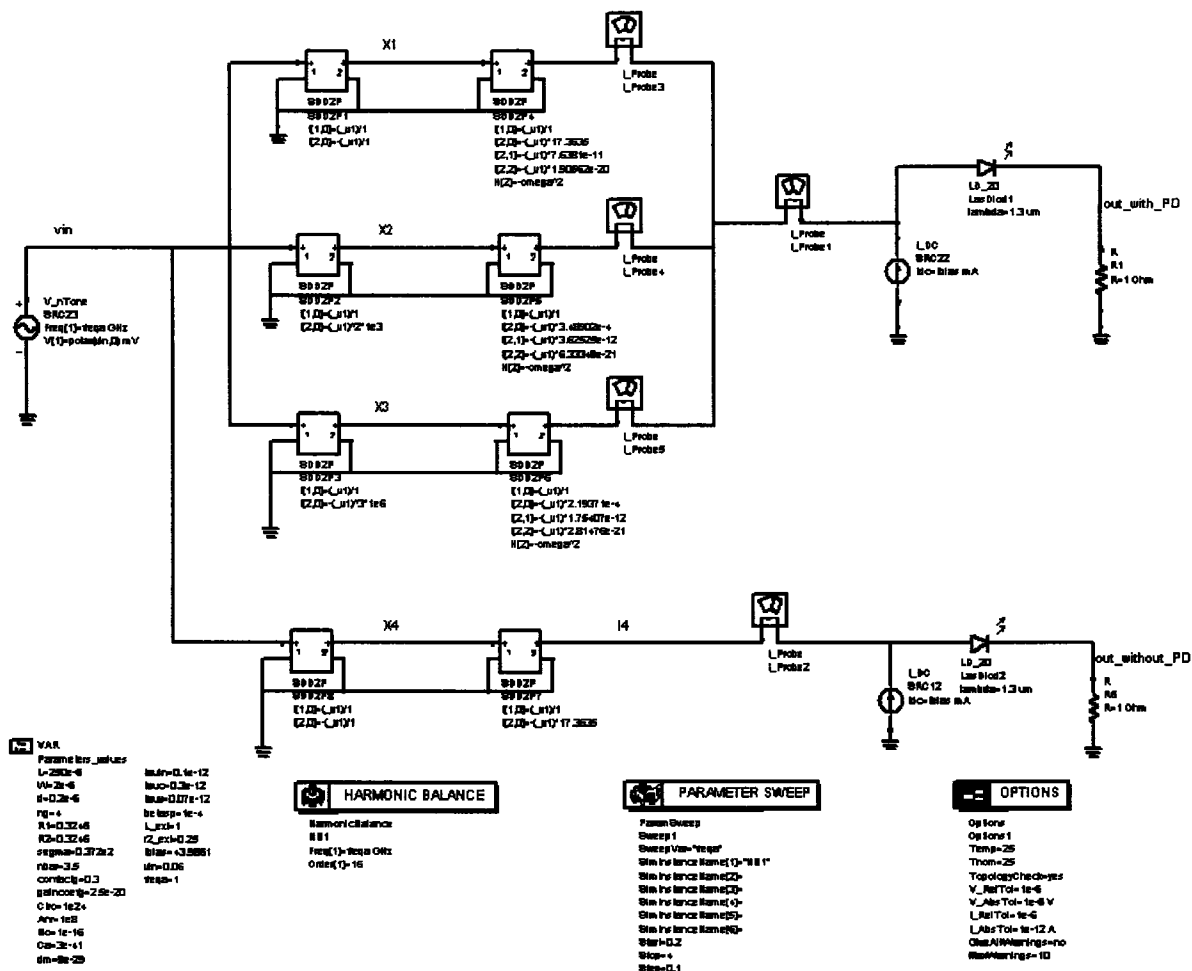


Figure 7.3: ADS setup of the laser inverse model cascaded to the laser model.

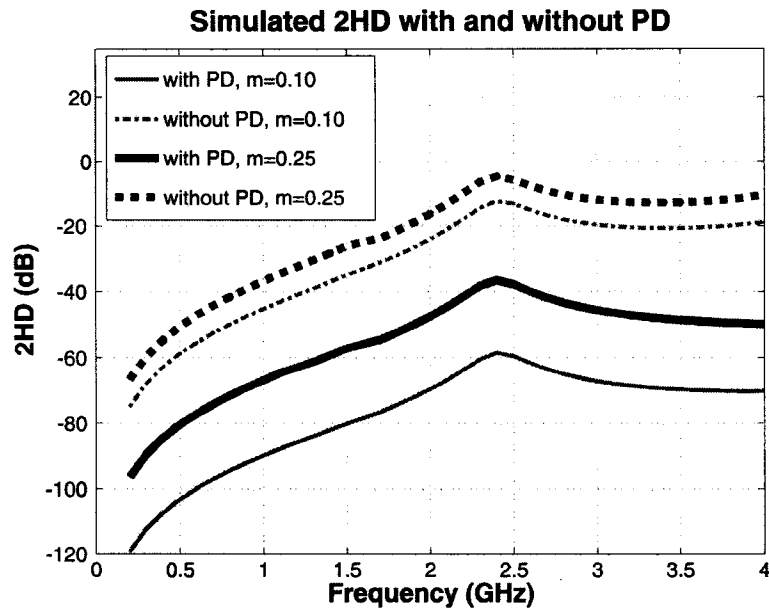


Figure 7.4: Simulated second order harmonic with and without PD for 0.10 modulation index and 0.25 modulation index.

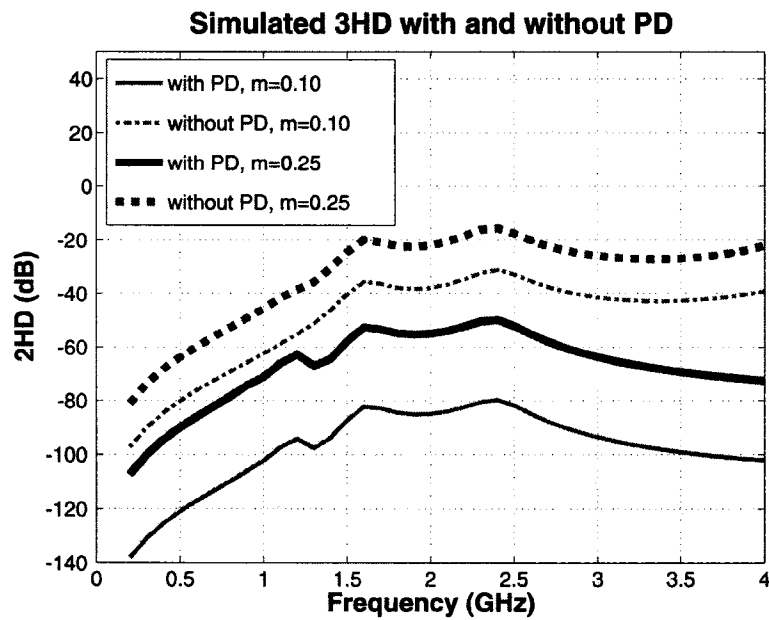


Figure 7.5: Simulated third order harmonic with and without PD for 0.10 modulation index and 0.25 modulation index.

To simulate the second and third intermodulation distortions (2IMD and 3IMD), the cascaded laser model and the pre-distorter were directly modulated with two tones that are 10 MHz apart and monitoring the generated sum and difference frequencies. These included, the second intermodulation distortion ($f_1 + f_2$), the third intermodulation distortions ($2f_1 + f_2$, $2f_1 - f_2$, $2f_2 + f_1$, and $2f_2 - f_1$).

Figures 7.6 - 7.10 on page 132 show how the proposed pre-distorter decreases the aforementioned intermodulation distortion components.

Figure 7.6 illustrates the simulation results of the second order intermodulation distortion of type ($f_1 + f_2$) for modulation index of 0.10. Results show that the pre-distorter has reduced the second order intermodulation distortion by an average of 50 dB over a bandwidth of 2 GHz, from 2 GHz to 4 GHz. A peak was observed around a frequency of 2.4 GHz which may attributed to one of the intermodulation frequencies of f_1 and f_2 .

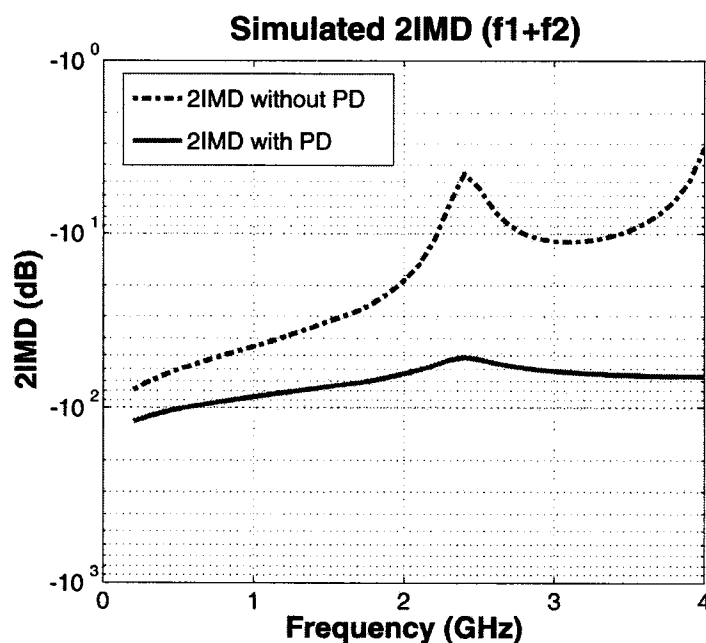


Figure 7.6: Simulated second intermodulation distortion ($f_1 + f_2$) with and without PD for 0.10 modulation index.

Figure 7.7 on the following page shows the simulation results of the third order intermodulation distortion ($2f_1 + f_2$) for modulation index of 0.10. The pre-distorter has

reduced the third order intermodulation distortion by an average of 40 dB over bandwidth of 2.5 GHz, between 1.5 GHz and 4 GHz. Two peaks were observed around frequencies of 1.6 GHz and 2.4 GHz, these may also attributed to some of f_1 and f_2 intermodulation frequencies.

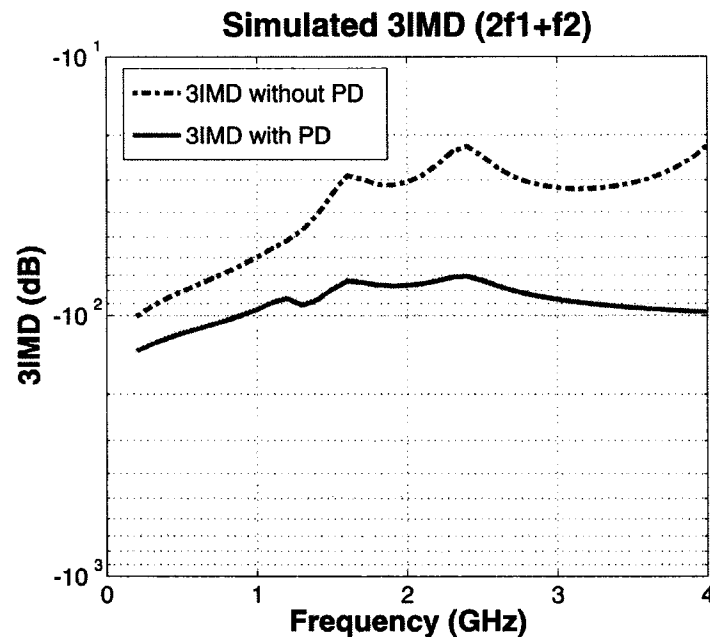


Figure 7.7: Simulated third intermodulation distortion ($2f_1 + f_2$) with and without PD for 0.10 modulation index.

Figure 7.8 on the next page shows the simulation results of the third order intermodulation distortion ($2f_1 - f_2$) for modulation index of 0.10. An average enhancement of 35 dB for the 3IMD of type ($2f_1 - f_2$) has been achieved over bandwidth of 2 GHz, between 2 GHz and 4 GHz.

Figure 7.9 on page 131 illustrates the simulation results of the third order intermodulation distortion ($2f_2 + f_1$) for modulation index of 0.10. Using the proposed pre-distorter improved the 3IMD of type ($2f_2 + f_1$) by an average value of 40 dB over 2.5 GHz bandwidth, from 1.5 GHz to 4 GHz. The two peaks that perviously observed with ($2f_1 + f_2$) intermodulation distortion type are also observed with ($2f_1 + f_2$) type.

Figure 7.10 on page 132 shows the simulation results of the third order intermodulation

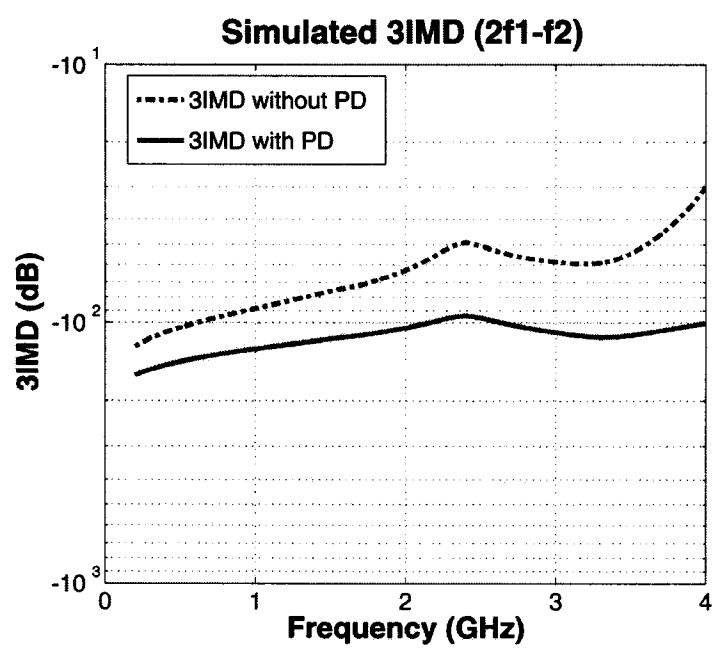


Figure 7.8: Simulated third intermodulation distortion ($2f_1 - f_2$) with and without PD for 0.10 modulation index.

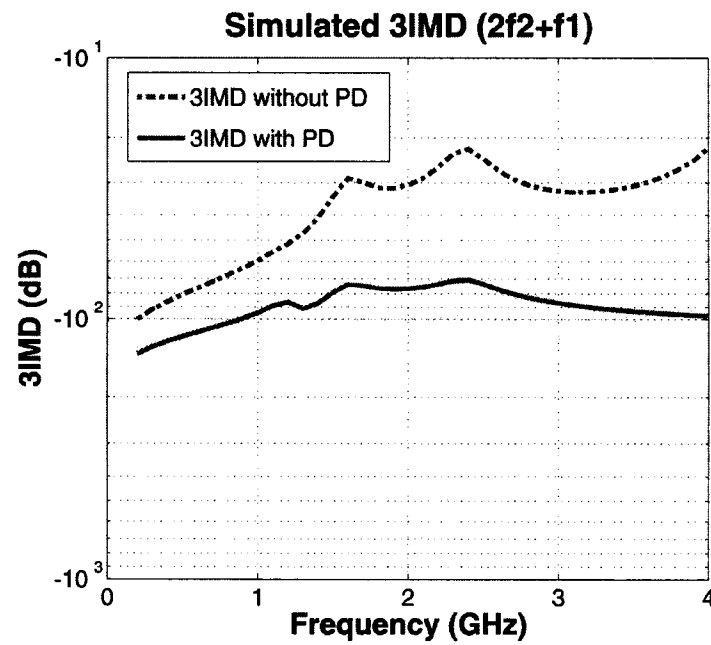


Figure 7.9: Simulated third intermodulation distortion ($2f_2 + f_1$) with and without PD for 0.10 modulation index.

distortion ($2f_2 - f_1$) for modulation index of 0.10. As can be seen from the results, the pre-distorter has reduced the 3IMD of type ($2f_2 - f_1$) by an average of 35 dB over bandwidth of 2 GHz, from 2 GHz to 4 GHz.

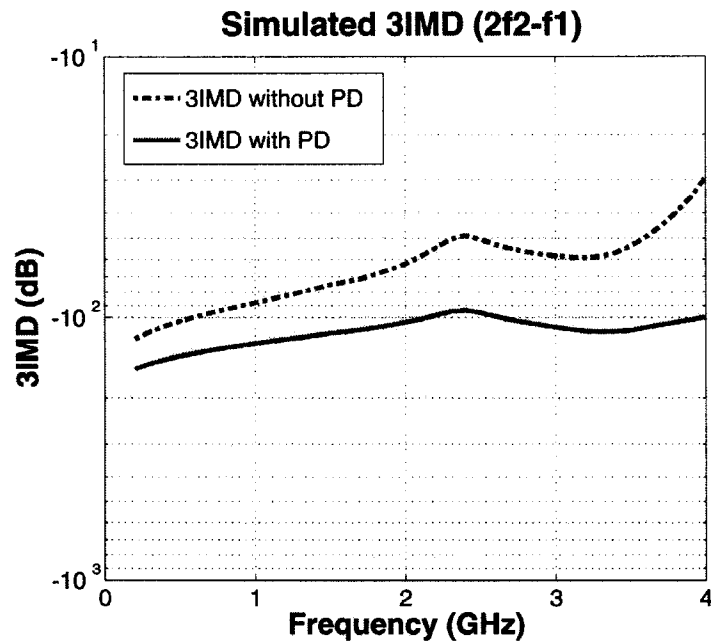


Figure 7.10: Simulated third intermodulation distortion ($2f_2 - f_1$) with and without PD for 0.10 modulation index.

The above results are summarized in Table 7.1.

7.4 Typical CATV system

To characterize CATV system linearity, N signals of equal power level are applied to the system spaced 6 MHz apart [47]. In order to meet CSO and CTB requirements for CATV systems, the laser's second order harmonic distortion and third order intermodulation distortion of types ($2f_1 \pm f_2$ and $2f_2 \pm f_1$) must be in the vicinity of -75 dBc and -100 dBc respectively, for a modulation index of 0.04 [4].

Figure 7.11 on page 134 shows the simulated second harmonic distortion with and without using the pre-distorter for 0.04 modulation index. The results showed that an average improvement of 45 dB over bandwidth around 3.5 GHz, between 0.5 GHz and 4 GHz, can

Distortion Type	Average Improvement [dB]	Modulation Index
$2^{nd}HD$	45	0.10
$2^{nd}HD$	30	0.25
$3^{rd}HD$	55	0.10
$3^{rd}HD$	40	0.25
$2^{nd}IMD$ type $f_1 + f_2$	50	0.10
$3^{rd}IMD$ type $2f_1 + f_2$	40	0.10
$3^{rd}IMD$ type $2f_1 - f_2$	35	0.10
$3^{rd}IMD$ type $2f_2 + f_1$	40	0.10
$3^{rd}IMD$ type $2f_2 - f_1$	35	0.10

Table 7.1: Various distortion components improvement due to using the proposed pre-distorter.

be achieved using the proposed pre-distorter. Figure 7.12 on page 135 shows the simulated third harmonic distortion with and without using the pre-distorter for 0.04 modulation index. The results showed that an average improvement of 50 dB over bandwidth around 3.5 GHz, between 0.5 GHz and 4 GHz, can be achieved using the proposed pre-distorter. The second and third order harmonic distortions levels were decreased to values that are lower than -75 dB and -100 dB respectively.

The cascaded laser model and the pre-distorter were directly modulated with two tones that are 6 MHz apart. Various types of third order intermodulation distortions ($2f_1 \pm f_2$ and $2f_2 \pm f_1$) were simulated.

Figures 7.13 - 7.16 on page 137 show the simulation results of various third order intermodulation distortions for modulation index of 0.04. The pre-distorter has decreased all types of third order intermodulation distortions to values that are lower than -100 dB.

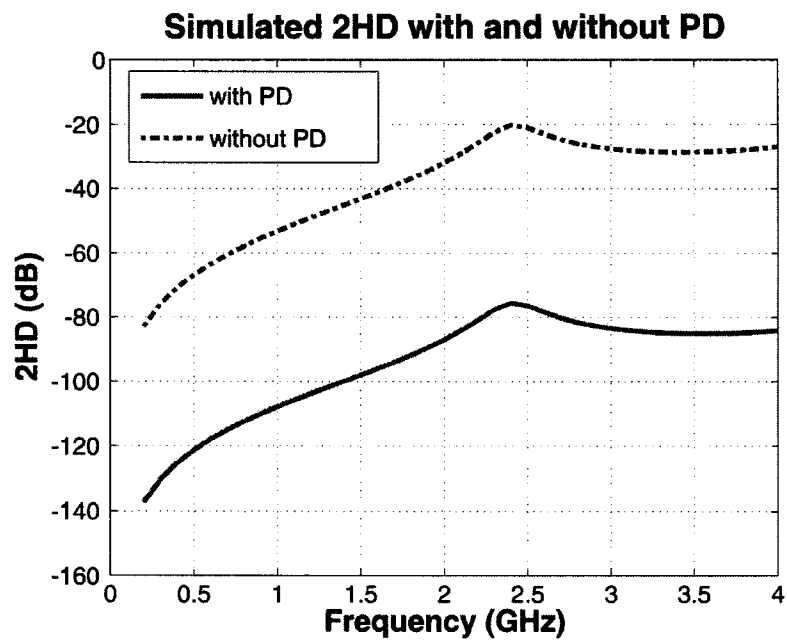


Figure 7.11: Simulated second order harmonic with and without PD for 0.04 modulation index.

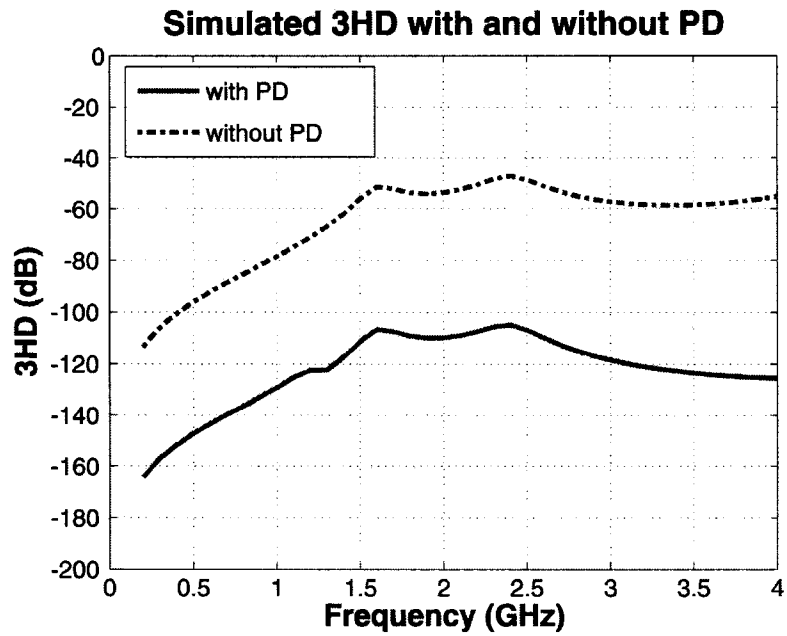


Figure 7.12: Simulated third order harmonic with and without PD for 0.04 modulation index.

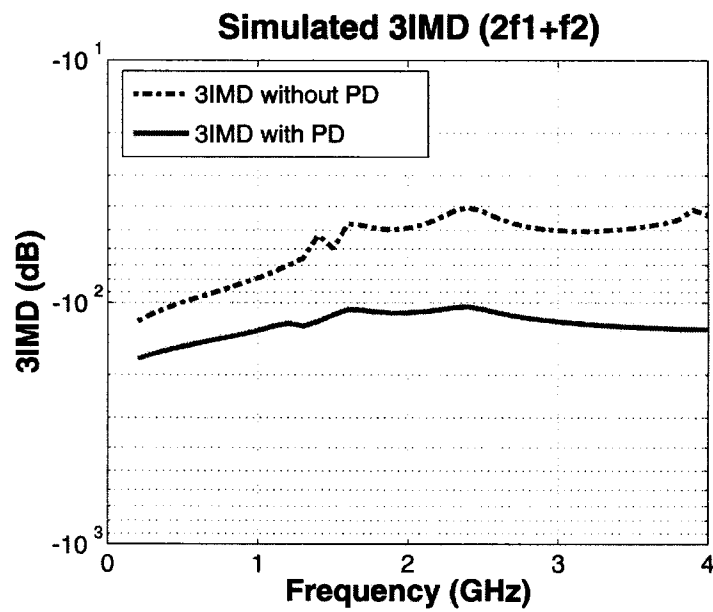


Figure 7.13: Simulated third intermodulation distortion ($2f_1 + f_2$) with and without PD for 0.04 modulation index.

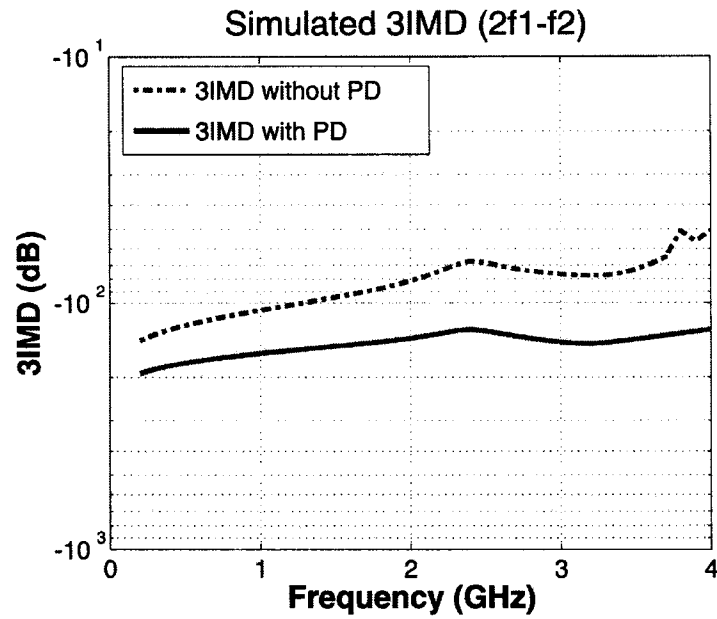


Figure 7.14: Simulated third intermodulation distortion ($2f_1 - f_2$) with and without PD for 0.04 modulation index.

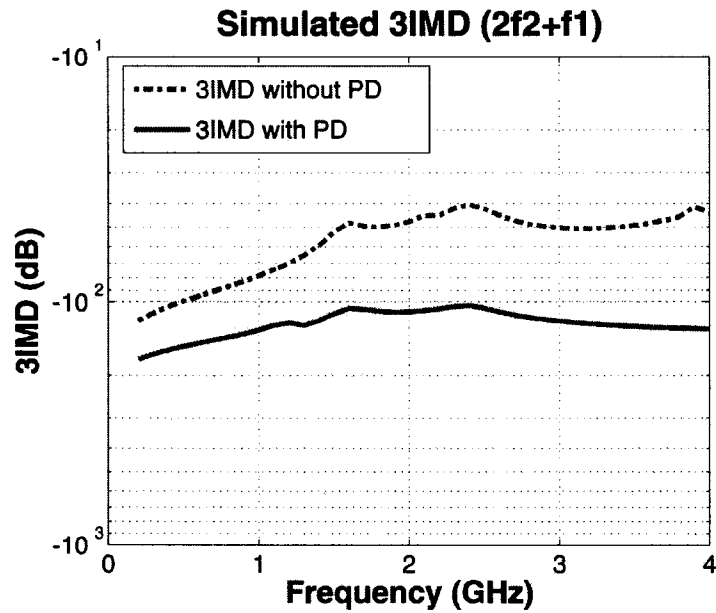


Figure 7.15: Simulated third intermodulation distortion ($2f_2 + f_1$) with and without PD for 0.04 modulation index.

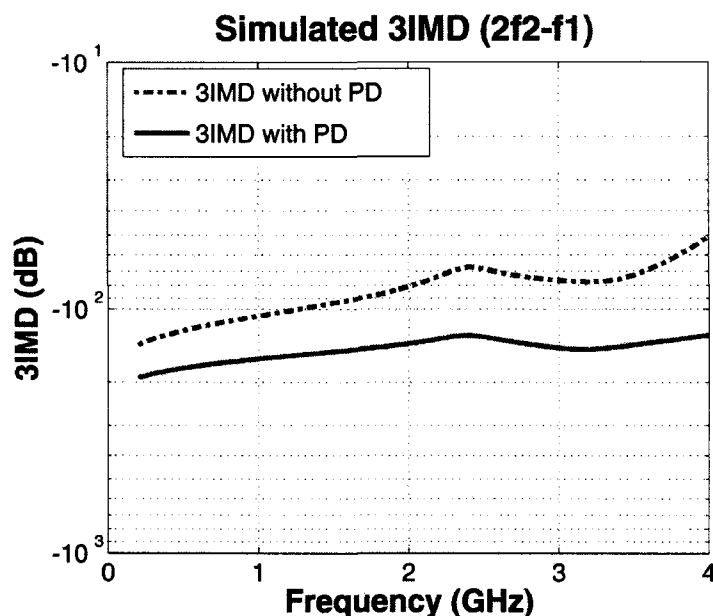


Figure 7.16: Simulated third intermodulation distortion ($2f_2 - f_1$) with and without PD for 0.04 modulation index.

7.5 Summary

In this chapter we developed a laser pre-distorter based on the inverse laser model including the feedback effect. Volterra series technique was used to extract the pre-distorter coefficients. A pre-distorter model was implemented in ADS and cascaded to the laser model. Various laser distortion components were simulated both with and without the pre-distorter. Simulation results showed that, at a modulation index of 0.1, average improvements of 45 dB, 55 dB, and 40 dB were achieved for second order, third order harmonic distortion, and various intermodulation distortions respectively when using the proposed pre-distorter. At modulation index of 0.04, the pre-distorter has decreased the second order harmonic distortion and various types of third order intermodulation distortions to values that are lower than -75 dB and -100 dB respectively.

The above results show that the proposed pre-distorter significantly improved the DFB laser linearity and make it suitable for the analog CATV applications.

Chapter 8

Conclusions and Future Work

8.1 Conclusions

The single mode semiconductor laser rate equations were augmented to include effects of optical back-reflections. These augmented rate equations were incorporated in the implementation of a semiconductor laser model using Agilent Advanced Design System (ADS) [53]. The ADS model was used in simulations to determine the effect of reflected optical power on the laser's DC characteristics, noise, and linearity. The DFB laser diode's threshold level, relaxation oscillation, relative intensity noise, and distortion under optical back-reflections were simulated using various ADS setups. Simulation results were presented along with relevant measurements. Simulation results and experimental measurements were found to be in good agreement.

The operation of an unisolated DFB laser diode in different optical feedback regimes was experimentally investigated. This was achieved using induced tunable back-reflections. The setup involved a fiber optic reflector, a variable attenuator, a polarization controller, and a 3-dB fiber optic beam splitter. Results show that it is desirable to operate a DFB laser diode with optical feedback without the need for incorporating a costly built-in optical isolator. This is achieved by operating the DFB laser in feedback Regime V, at which the DFB laser diode operates on a single longitudinal mode with low RIN and narrow linewidth for all phases of feedback. Moreover, the DFB laser diode will be insensitive to any further external optical back-reflection. This could not only reduce the cost, but may also simplify the construction of the multi function integrated device.

The experimental results were used to determine the conditions needed to force the

DFB laser diode to operate in feedback Regime V. In other words, we determined how much optical back-reflection is needed to drive the DFB laser diode to operate in feedback Regime V. Based on these findings, a feedback topology that uses a Fiber Bragg Grating (FBG) was proposed. This topology removes the need for a reflector, variable attenuator, or fiber optic beam splitter. The FBG was designed using the OptiGrating software. It was then implemented such that the desired back-reflection level is induced when the FBG is attached to the unisolated DFB laser.

The performance of the DFB laser diode attached to the FBG was analyzed using an Agilent 71400 lightwave signal analyzer. Results were compared to that of the isolated DFB laser diode. Two telecommunications wavelengths, 1310 nm and 1550 nm, were examined. DFB lasers showed stable spectra, low RIN, and narrow linewidth output when attached to the appropriate FBG. For 1550 nm, the unisolated DFB laser coupled to the FBG achieved a RIN level of -117.31 dB/Hz. On the contrary, the isolated DFB laser achieved only -114.51 dB/Hz at a 1 GHz frequency offset. For 1310 nm, the unisolated DFB coupled to the FBG achieved a RIN level of -158.5 dB/Hz. This was comparable to -157.9 dB/Hz of the isolated DFB laser operating at a 1 GHz frequency offset for the same optical average power (5.1 dBm) [54]. Attaching a FBG to a DFB laser increased the second and third order harmonic distortions by an average of 3 dB compared to the isolated DFB laser, for both wavelengths.

A pre-distorter model that includes optical back-reflection effects was derived from the laser inverse model using the Volterra series technique. The extracted pre-distorter coefficients were implemented in ADS and cascaded to the laser model to compensate for the laser distortions. Various distortion components were simulated for laser model both with and without the pre-distorter. Simulation results showed that at a 0.10 modulation index, average improvements of 45 dB in second order harmonic distortion, 55 dB in third order harmonic distortion, and 40 dB in various intermodulation distortions can be achieved using the proposed pre-distortion technique. Also at modulation index of 0.04, the pre-distorter has reduced the second order harmonic distortion and two-tone third order intermodulation distortion levels to values that are lower than -75 dB and -100 dB respectively, this makes the laser suitable for CATV applications. Although the optical

back-reflected power is considered one of the major sources for laser noise and nonlinearity, state-of-the-art laser pre-distorters do not account for this effect. Our proposed pre-distorter considerably advances the state-of-the-art by providing a model that is a few steps closer to a comprehensive compensation for the overall laser distortion sources.

8.2 Future Work

Future improvements of this work include the following.

- **Improved laser model.** Incorporating other noise and distortion sources such as laser packaging effect will improve the laser model. The laser package is the interface between the laser module and the rest of the optical system components. It provides mechanical protection and an electrical interface for the laser chip. The laser package also provides the means of removing heat and controlling the laser's temperature. The package parasitics increases distortion and limits the laser bandwidth. Inclusion of packaging parasitic effect in the laser model is highly recommended in order to simulate even more realistic laser performance.
- **Better pre-distorter model.** The laser pre-distorter model is extracted from the laser model. Hence, including more distortion sources in the laser model will lead to a better distortion compensation capability for the pre-distorter. In addition, increasing the order of the extracted Volterra transfer functions of the pre-distorter will improve the linearity performance.
- **Development of an adaptive configuration for the pre-distorter.** Adaptive pre-distorters frequently monitor the lasers output in order to update the pre-distorter coefficients and compensate for any of the lasers' time-varying nonlinearities. As an extension for the pre-distorter model; adaptive algorithms can be used in the pre-distorter model to enable the prediction of the output power variations and hence allows adjusting the pre-distorter coefficients accordingly. Figure 8.1 on the next page shows a block diagram of the suggested adaptive pre-distorter. In this configuration second and third order harmonics of the input signal are generated by appropriate circuits. The feedback path contains a photodiode to monitor the distortion levels and hence update the pre-distorter coefficients to compensate for thermal effects,

aging, and any other changes.

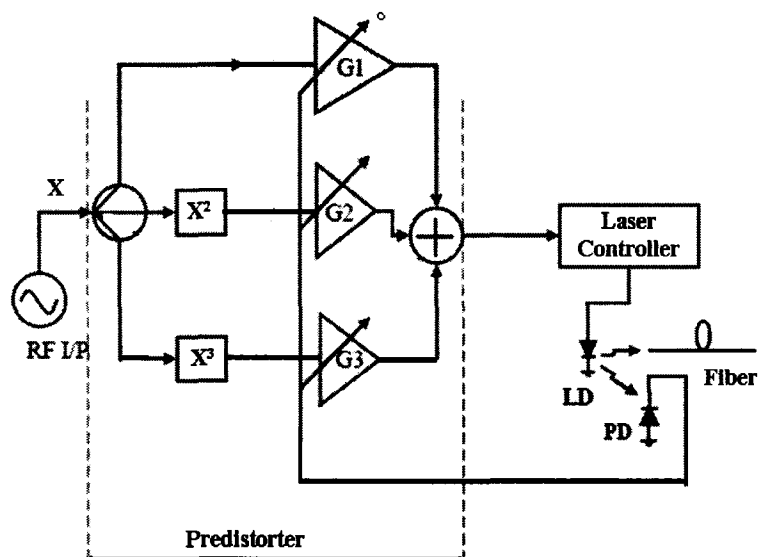


Figure 8.1: Block diagram of the suggested adaptive pre-distorter.

- FPGA (Field Programmable Gate Array) pre-distorter implementation.** The desired extension of the proposed pre-distorter model involves circuit level implementation. The initial step can be achieved by implementing the pre-distorter using an FPGA board. The pre-distorter coefficients can be computed, and the model can be described in blocks using suitable software. The laser model and the pre-distorter model have to be implemented using the blocks corresponding to the used FPGA board, the FPGA board can be tested using generated TV signals.
- High frequency and broadband circuit design.** As explained in Chapter 7, the pre-distorter contains three branches that need to be designed using three main circuits; the linear circuit to drive the laser, the squaring circuit to provide required second order distortion, and the cubing circuit to provide required third order distortion. The overall circuit of the designed pre-distorter has to be implemented first in software in order to examine the pre-distorter performance.

- **Hardware implementation and fabrication.** Pre-distorter hardware implementation is suggested when the designed pre-distorter circuit achieves the desired performance over the required frequency bandwidth, that is when it achieves the desired levels of different harmonic and intermodulation distortion components.
- **Pre-distorter testing.** Finally, the fabricated pre-distorter circuit can be tested by measuring the laser linearity improvements due to the use of the pre-distorter circuit. This can be achieved by measuring the laser linearity using a lightwave signal analyzer.

Appendix A

Measurements Equipments and Results

A.1 Different Equipments Used in The Measurements

A.1.1 DFB laser diodes, laser mount and laser controller

Two DFB laser diodes were used in the measurements: A Laser mate 1550 MQW-DFB pig-tailed laser diode and Laser mate 1310 MQW-DFB, both had a coaxial structure packaging without an isolator. The ILX lightwave LDC-3724B laser diode controller was used to provide the bias current and the temperature control to the lasers through the THORLABS TCLDM9 5.6mm/9mm Laser diode Mount.

A.1.2 Fiber optic beam splitter

The OZ FOBS, shown in Figure A.1, was used to divide and couple light in two directions (fibers). It is a two-by-two bi-directional coupler with a 50/50 splitting ratio. It has four ports: 1, 2, T, and R. The coupling efficiencies from ports 1 and 2 into port R are similar to those from port T into ports 1 and 2. All of its four ports are attached to a single mode fiber pigtail terminated with FC/APC connectors. The FOBS insertion loss is 0.7dB, the back-reflection level is -60dB, and its cross talk level is less than -40dB. In the experimental setup, the input from the DFB laser diode goes out through port T. Half of the light is

coupled into port 1 in order to monitor the source power using OSA, the other half goes through port 2 to the reflector. Port R couples as much of the back-reflected signal from port 2, while simultaneously port T collects the same amount.



Figure A.1: OZ Optics fiber optic beam splitter with a 50/50 splitting ratio.

A.1.3 Fiber optic reflector

Figure A.2 shows the OZ Optics Fiber optic reflector. It is a fiber pigtailed reflector terminated with a FC/APC connector that is used to reflect the light. It consists of a fiber optic collimator and a mirror. The output is first collimated, then strikes the mirror and finally reflected back into the collimator. It offers a total reflection for the incident optical power with an insertion loss less than 1.4 dB.

A.1.4 Variable attenuator

The OZ Optics variable attenuator shown in Figure A.3 consists of two baseplates. Each baseplate contains a fiber followed by a collimating lens. In order to control the level of attenuation, a screw is used to block the collimated beam between the two lenses. to control

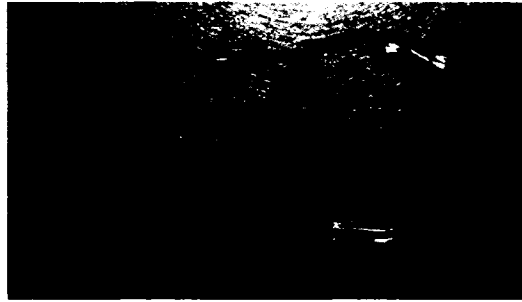


Figure A.2: OZ Optics fiber optic reflector with total reflection.

the attenuation level. The attenuator insertion loss is -0.75 dB, it offers an attenuation range from its insertion loss up to 80 dB.



Figure A.3: OZ Optics variable attenuator of attenuation range up to 80 dB.

A.1.5 Optical multimeter

The ILX Lightwave OMM-6810B Optical Power and Wavelength Meter together with the ILX Lightwave OMH-6745B Fiber Optic power/wavehead shown in Figure A.4 were used in the measurements. These instruments are capable of measuring the optical power and wavelength of semiconductor lasers.

A.1.6 Optical Spectrum Analyzer

Agilent 86140B Optical Spectrum Analyzer shown in Figure A.5 was used for the required spectral analysis.

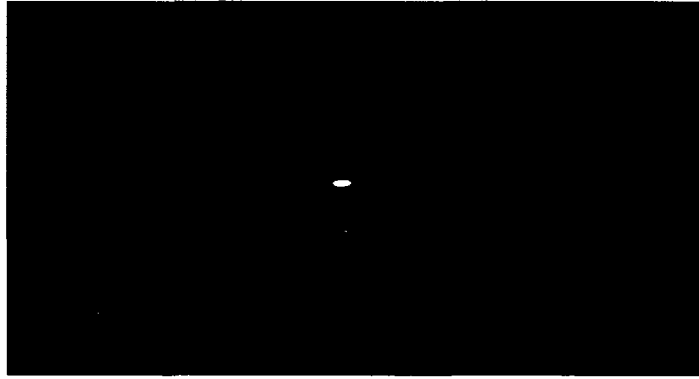


Figure A.4: ILX Lightwave OMM-6810B Optical Power and Wavelength Meter (top) and ILX lightwave LDC-3724B laser diode controller (Bottom).



Figure A.5: Agilent 86140B optical spectrum analyzer.

A.1.7 Polarization controller

OZ Optics Polarization controller shown in Figure A.6 is used to ensure that the reflected light back into the laser has the same polarization as the emitted light. It has two fiber pigtails at both sides terminated with FC/APC connector. Its insertion loss is less than 0.1 dB.



Figure A.6: OZ Optics polarization controller.

A.2 RIN Measurements Results

Figures A.7 - A.12 on page 150 show the measured average relative intensity noise of a 1310 nm DFB laser diode for bias current level of 15 mA and average external reflectivity ranging from -42 dB to -15 dB.

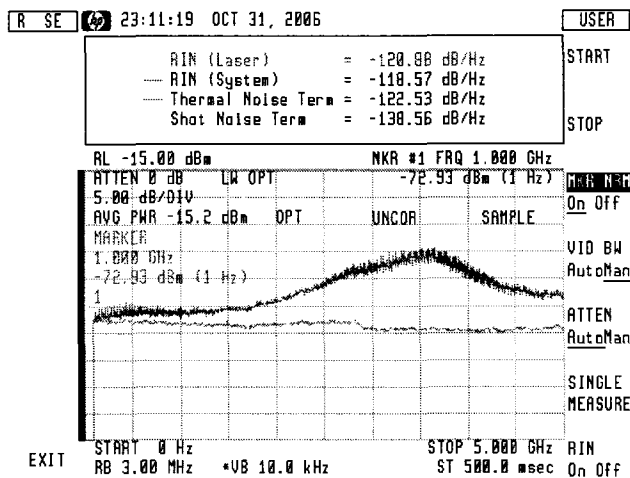


Figure A.7: Measured average relative intensity noise for bias current level of 15 mA and external reflectivity of -42 dB.

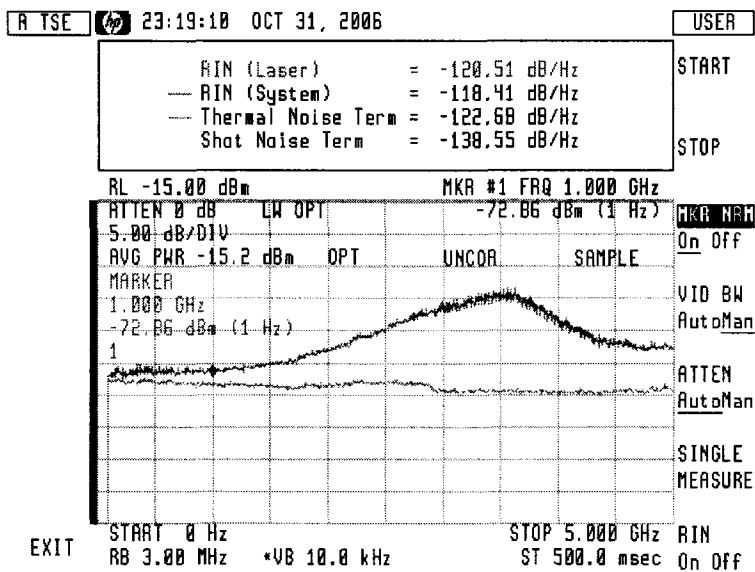


Figure A.8: Measured average relative intensity noise for bias current level of 15 mA and external reflectivity of -36 dB.

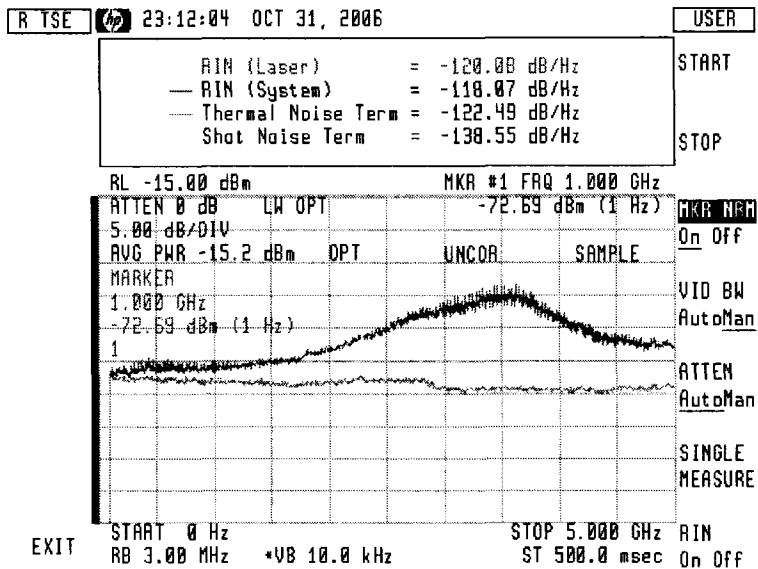


Figure A.9: Measured average relative intensity noise for bias current level of 15 mA and external reflectivity of -33 dB.

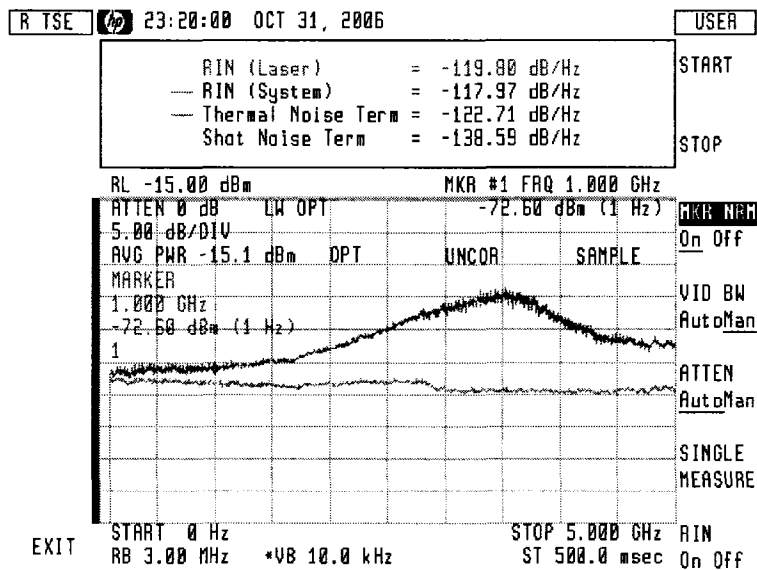


Figure A.10: Measured average relative intensity noise for bias current level of 15 mA and external reflectivity of -29 dB.

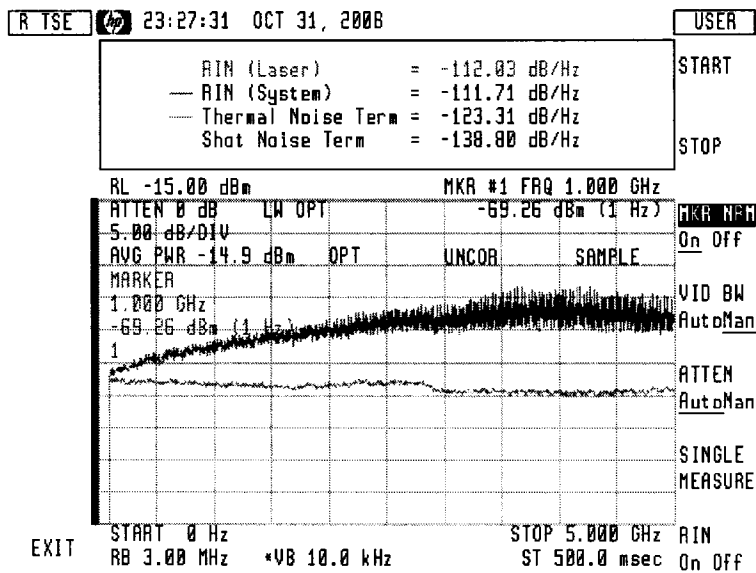


Figure A.11: Measured average relative intensity noise for bias current level of 15 mA and external reflectivity of -24 dB.

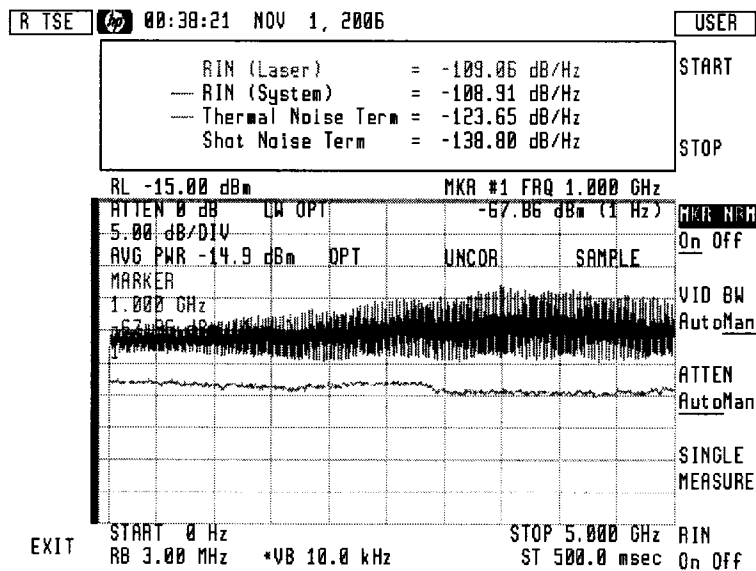


Figure A.12: Measured average relative intensity noise for bias current level of 15 mA and external reflectivity of -15 dB.

Appendix B

DFB Laser Diode with External FBG

B.1 FBG Design Steps

B.1.1 Step 1

The Optigrating software offers five available modules to work with (Single Fiber, Fiber Coupler, Single Waveguide, Waveguide Coupler, or Other Waveguide), for our application, we will choose Single Fiber.

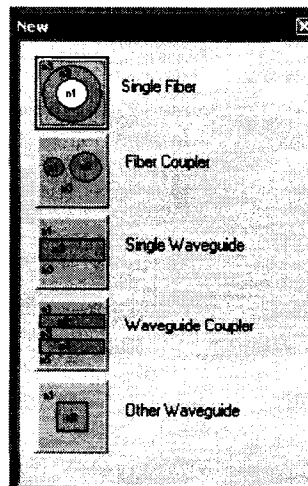


Figure B.1: FBG design step 1

B.1.2 Step 2

In this step we will be able to define the following characteristics for the fiber: Index Profile, Photosensitivity Profile, Number Of Points In Mesh, Central Wavelength, etc. We will choose the single fiber core and cladding dimensions to be $4.15 \mu\text{m}$ and $62.5 \mu\text{m}$ respectively and the central wavelength to be 1553 nm .

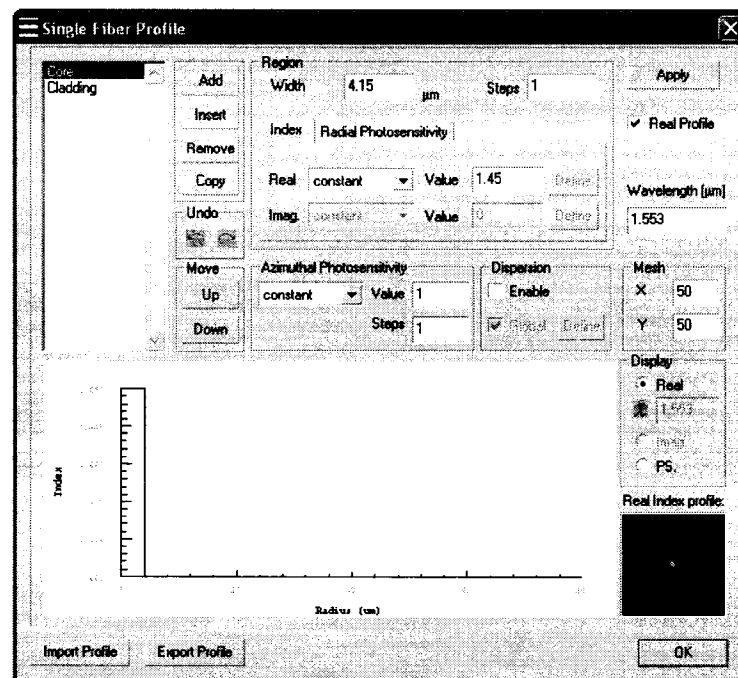


Figure B.2: FBG design step 2

B.1.3 Step 3

The fiber modes can be set in this step. OptiGrating gives us access to a list of the calculated modes of the fiber structure.

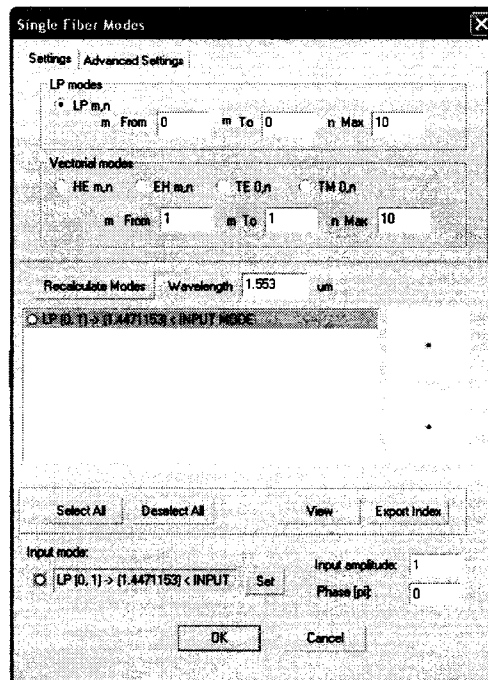


Figure B.3: FBG design step 3

B.1.4 Step 4

In this step, the parameters of the grating were defined. Based on the above calculations and the desired characteristics of the grating, the grating parameters are as follows: sine grating shape, uniform average index, no chirp, uniform apodization, $0.5365 \mu\text{m}$ grating period, 10 cm grating length, 3.075×10^{-5} index modulation which is equivalent to $\kappa L = 0.4812$.

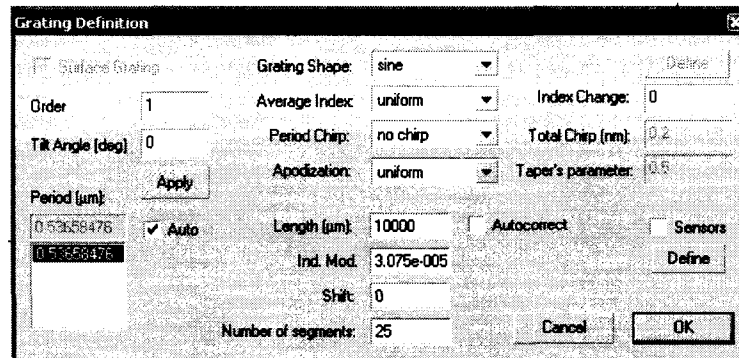


Figure B.4: FBG design step 4

B.1.5 Step 5

After defining all the necessary parameters for the FBG, we are now ready to work with the multiple view window and access different parameter buttons to examine our designed FBG. Figure B.5 shows the transmission (red curve) and the reflection (blue curve) characteristics of the designed FBG.

B.1.6 Step 6

The FBG FWHM 'full width at half maximum' bandwidth can be measured automatically using OptiGrating software. Figure B.6 shows the measurements of the designed FBG FWHM bandwidth, which was found to be 0.0792 nm .

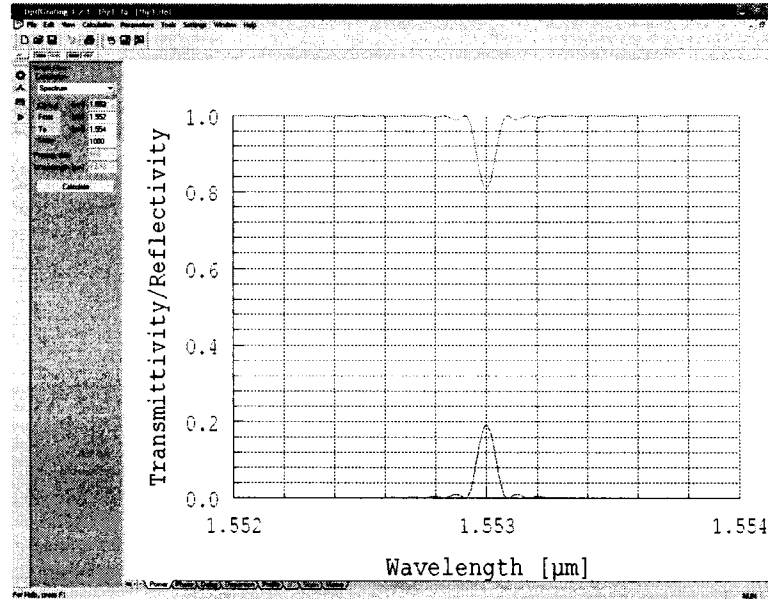


Figure B.5: FBG design step 5

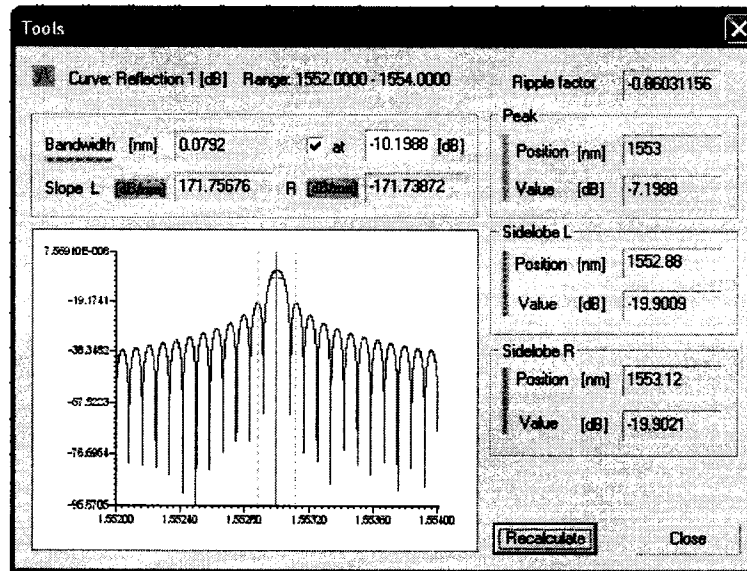


Figure B.6: FBG design step 6

B.2 FBG Transmission and Reflection Characteristics

Figures B.7 - B.12 on page 162 show different implemented FBGs with the indicated reflection and transmission characteristics.

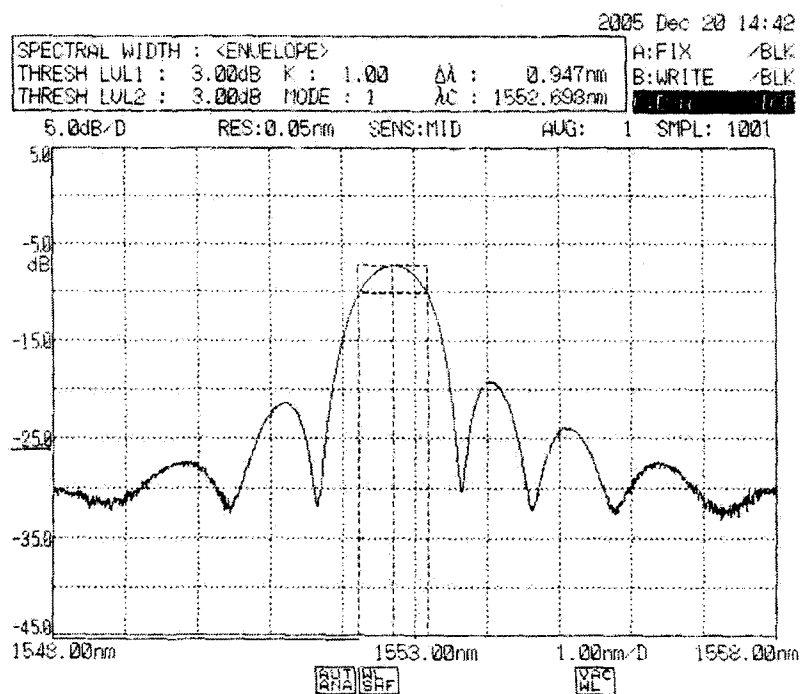
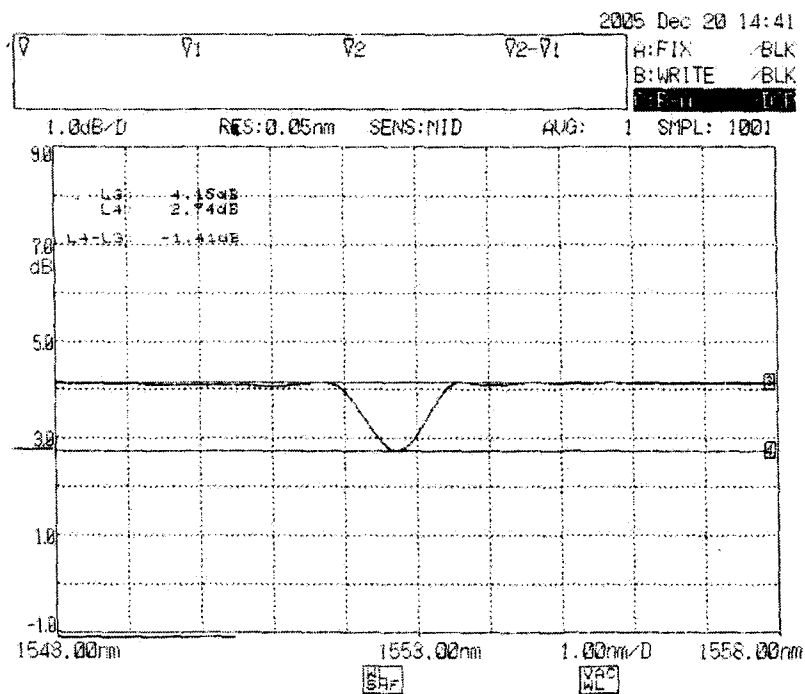


Figure B.7: The implemented FBG2 transmission (top) and reflection (bottom) characteristics.

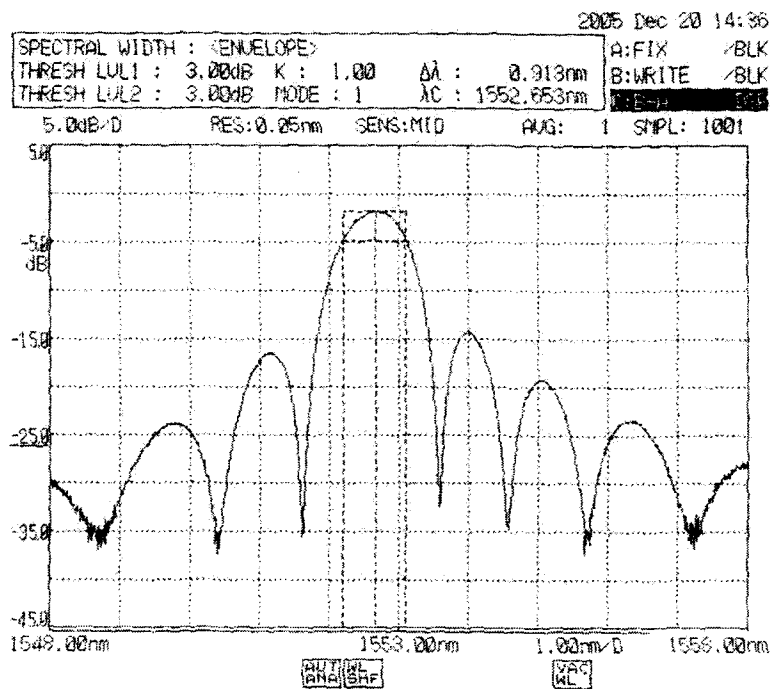
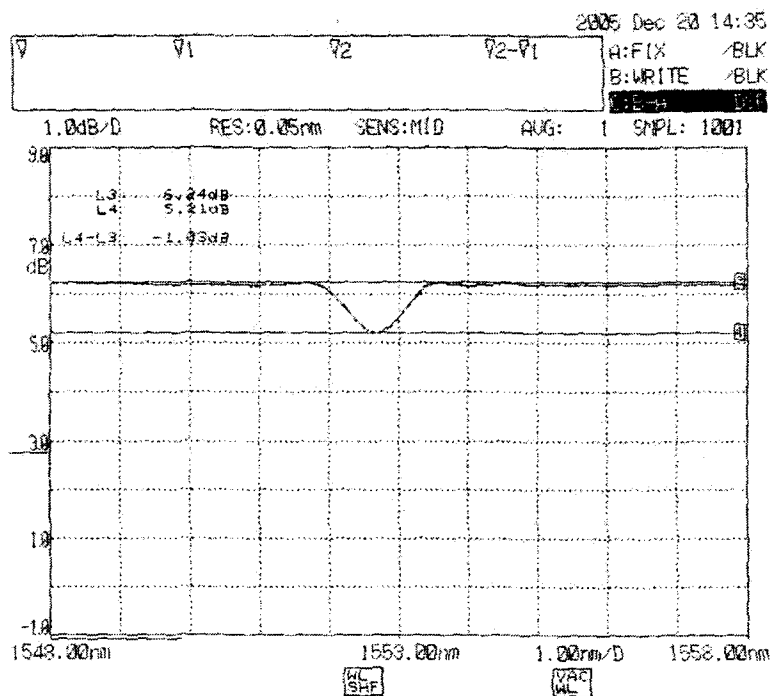


Figure B.8: The implemented FBG4 transmission (top) and reflection (bottom) characteristics.

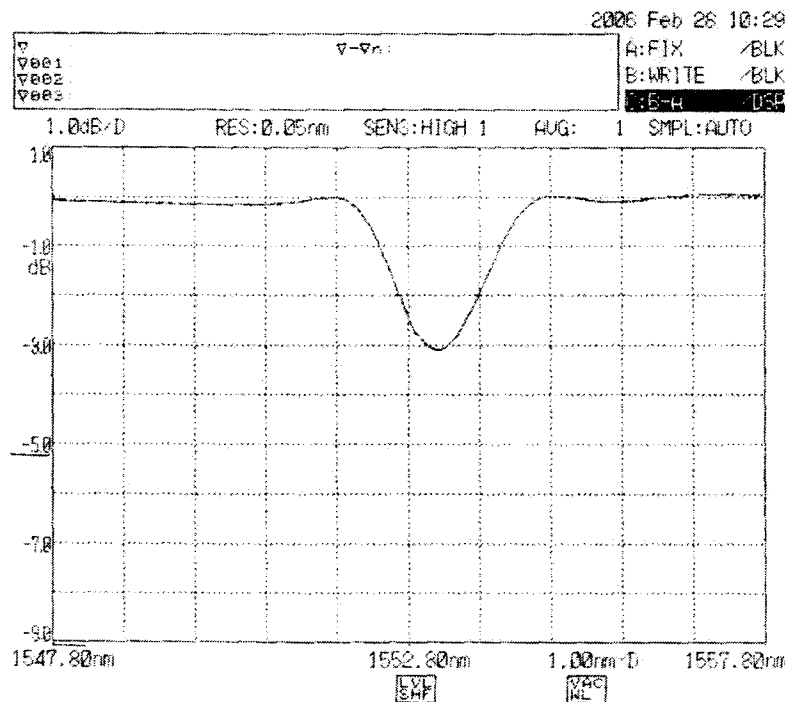
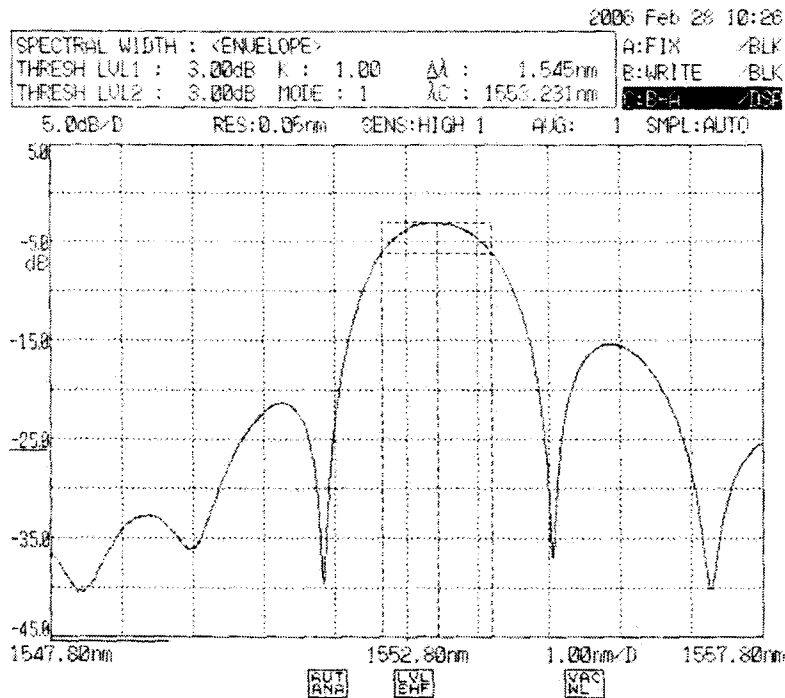


Figure B.9: The implemented FBG7 reflection (top) and transmission (bottom) characteristics.

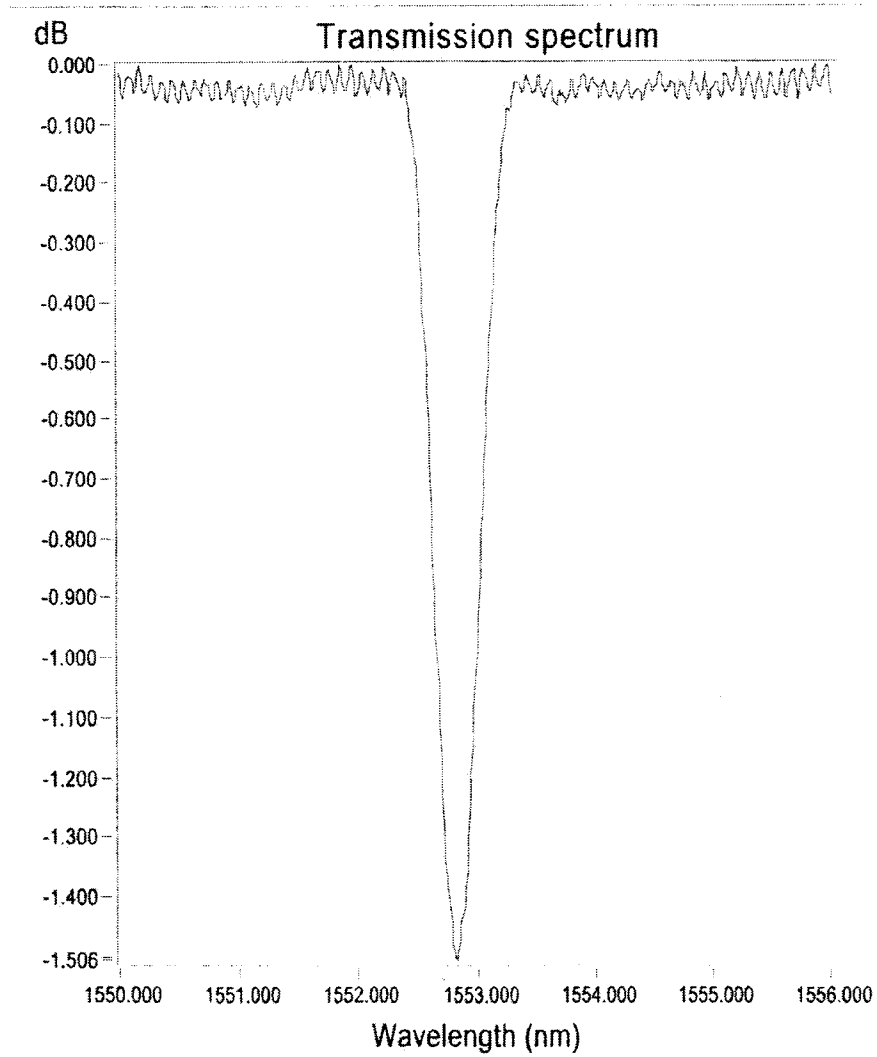


Figure B.11: The FBG11 transmission characteristics.

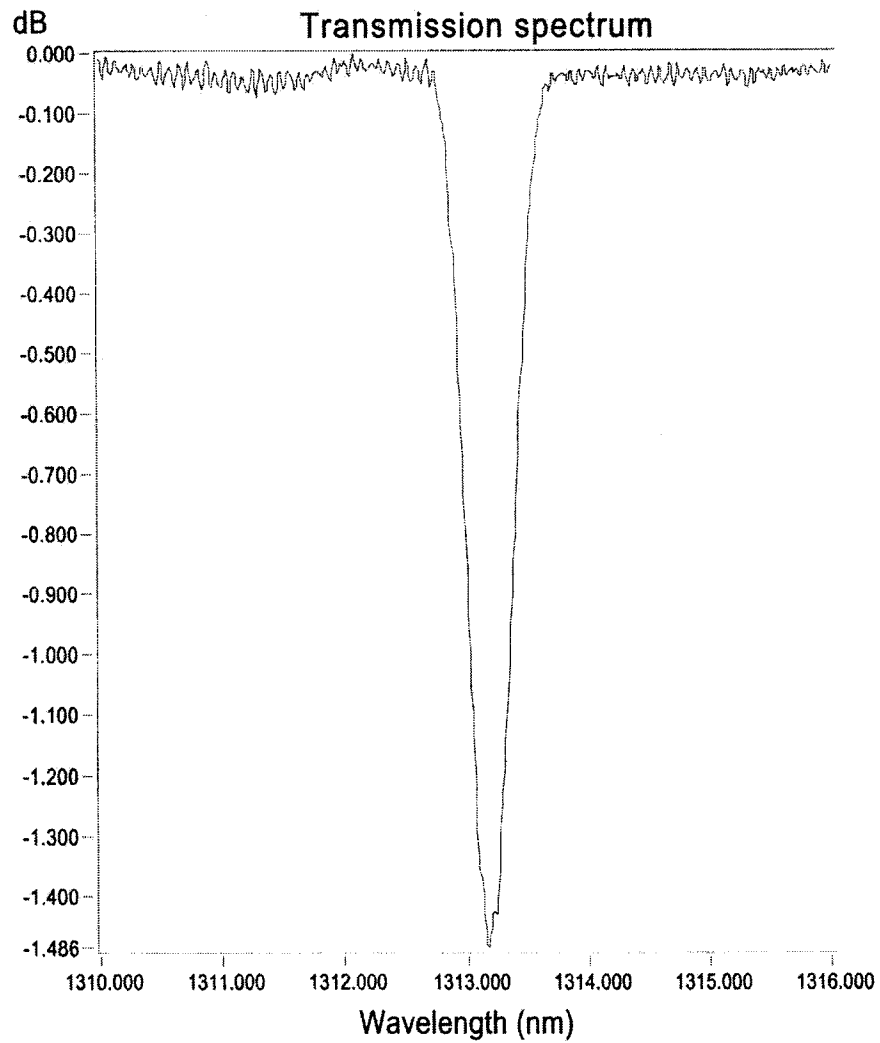


Figure B.12: FBG12 transmission spectrum at central wavelength of 1313.19 nm.

B.3 Spectrum Stability of DFB Laser with FBG

Figures B.13 - B.18 on page 166 show different spectra of DFB5 attached to various FBGs and biased at the indicated bias current.

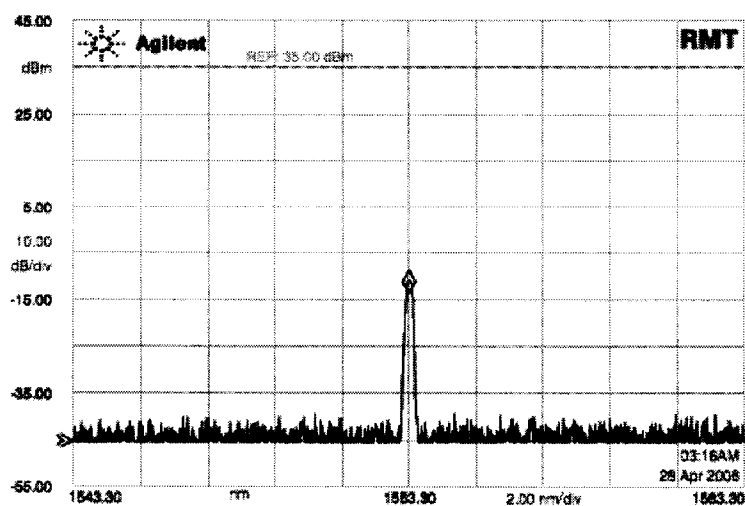


Figure B.13: Spectrum of DFB5 attached to FBG4 operating at bias level of 15 mA.

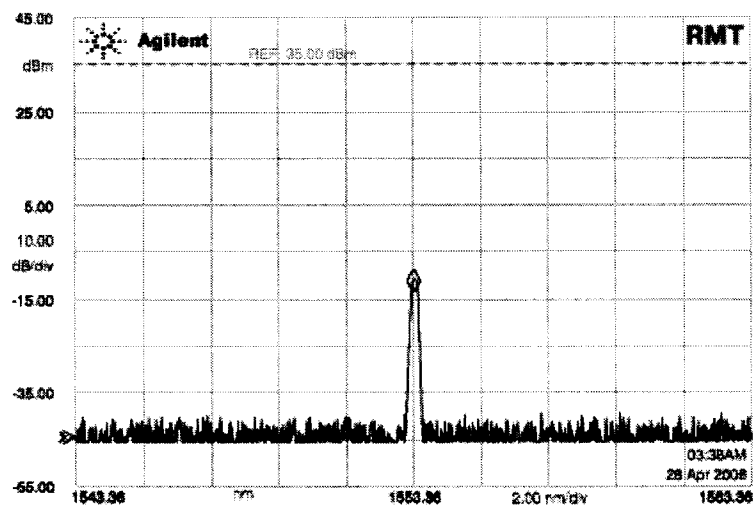


Figure B.14: Spectrum of DFB5 attached to FBG7 operating at bias level of 15 *mA*.

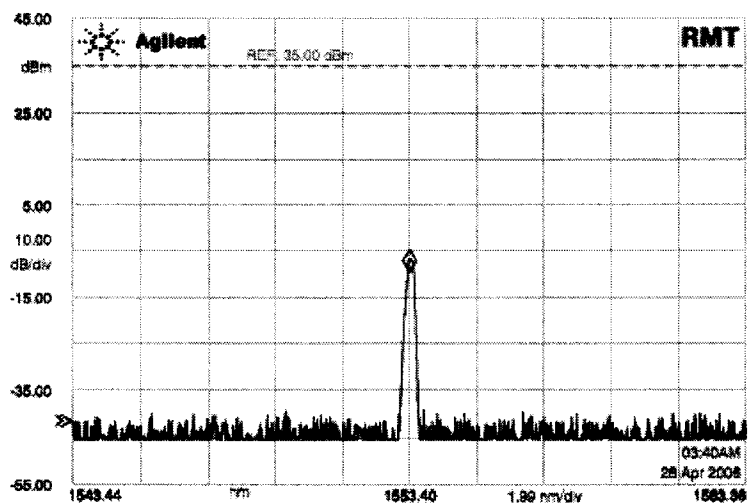


Figure B.15: Spectrum of DFB5 attached to FBG7 operating at bias level of 20 *mA*.

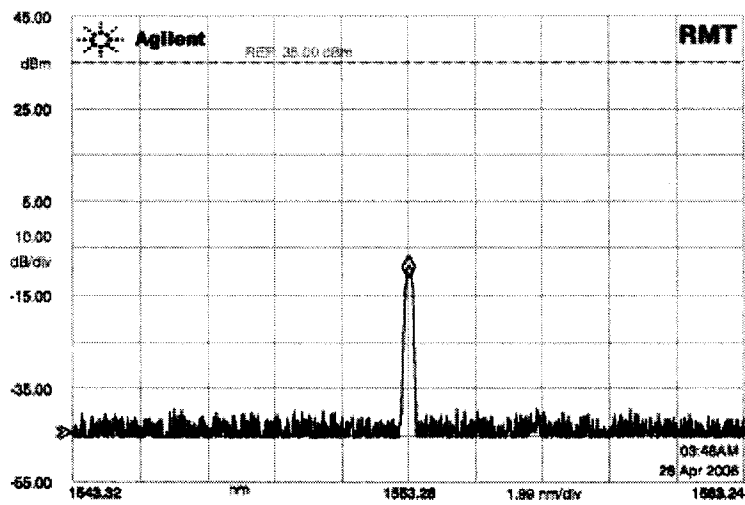


Figure B.16: Spectrum of DFB5 attached to FBG10 operating at bias level of 15 mA.

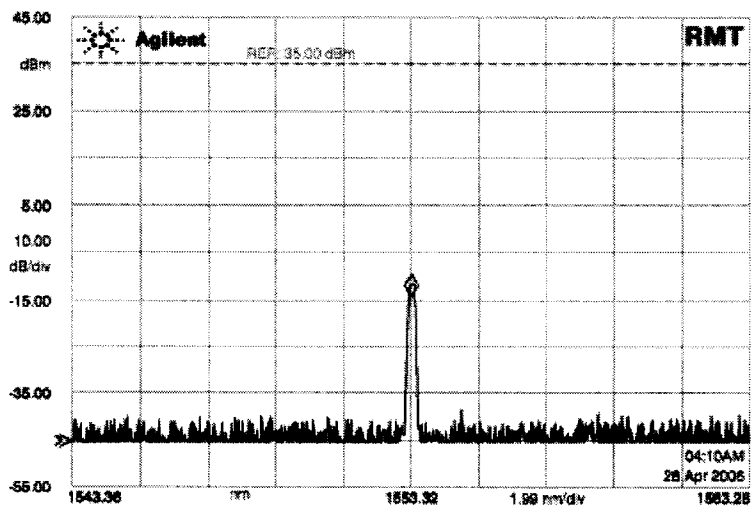


Figure B.17: Spectrum of DFB5 attached to FBG11 operating at bias level of 15 mA.

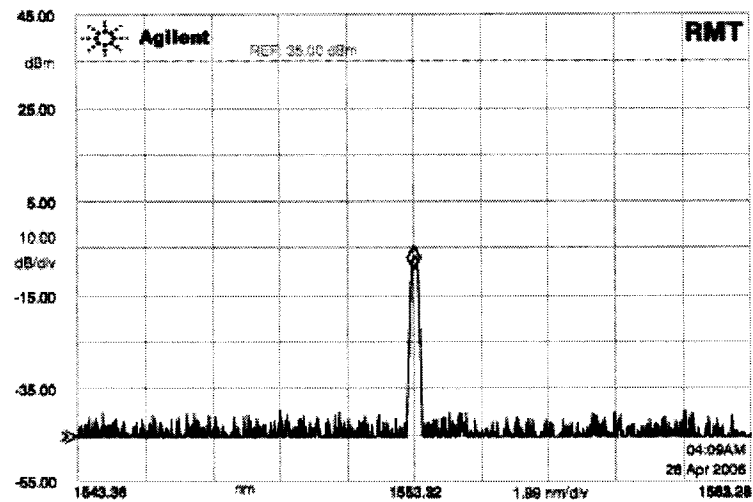


Figure B.18: Spectrum of DFB5 attached to FBG11 operating at bias level of 20 mA.

B.4 RIN Measurements of DFB Laser with FBG

Figures B.19 and B.20 on the next page show measured average RIN of DFB5 biased at 15 mA and attached to FBG1 and FBG5 respectively.

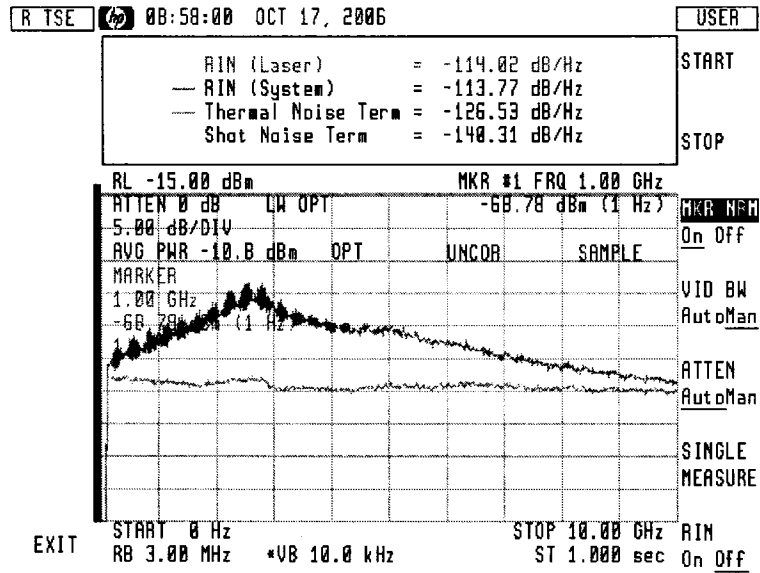


Figure B.19: Measured RIN of DFB5 attached to FBG1 operating at bias level of 15 mA.

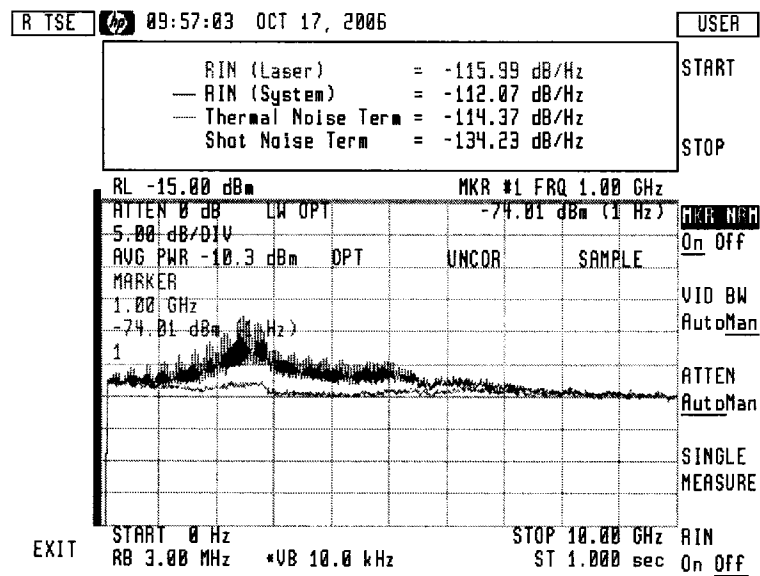


Figure B.20: Measured RIN of DFB5 attached to FBG2 operating at bias level of 15 mA.

B.5 Distortion Measurements of DFB Laser with FBG

Figures B.21 - B.28 on page 172 show measured second and third order harmonic distortions of DFB5 attached to various FBGs and operating at the indicated conditions.

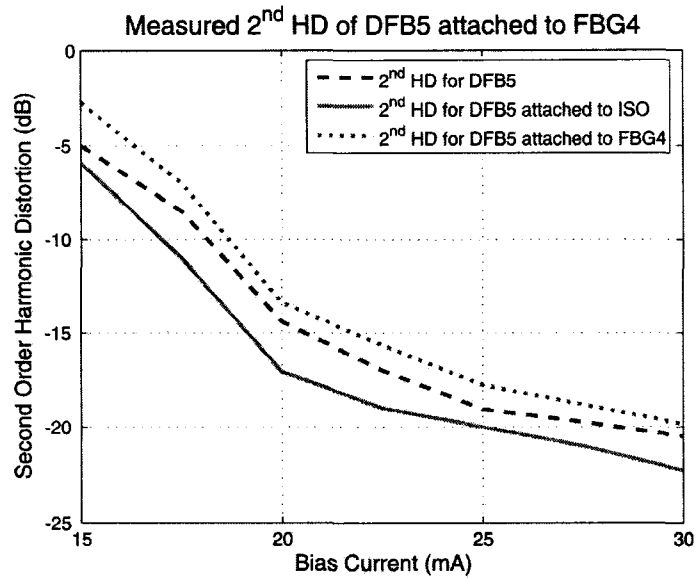


Figure B.21: Measured second order harmonic distortion normalized to the fundamental frequency of DFB5 attached to FBG4.

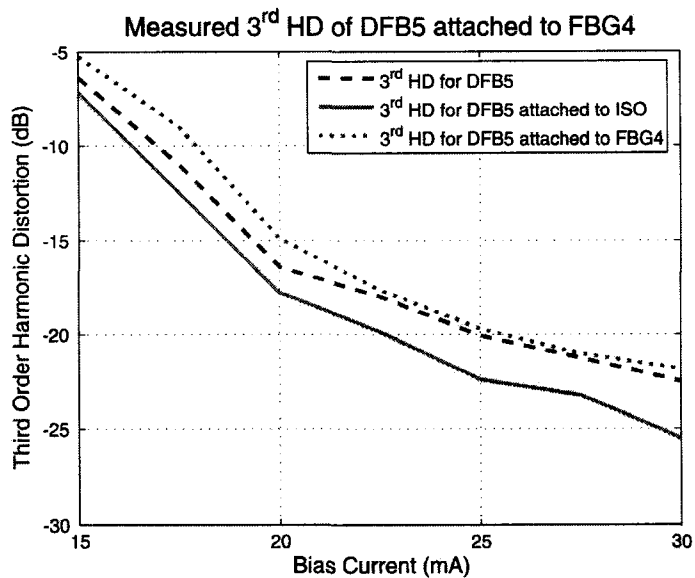


Figure B.22: Measured third order harmonic distortion normalized to the fundamental frequency of DFB5 attached to FBG4.

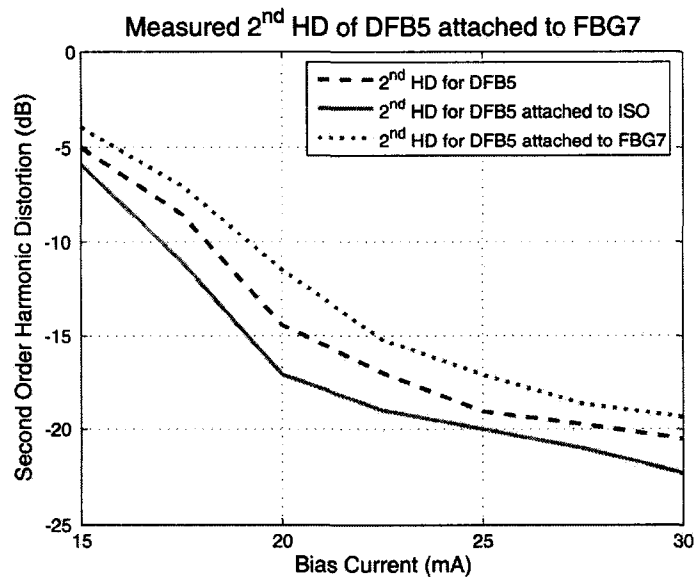


Figure B.23: Measured second order harmonic distortion normalized to the fundamental frequency of DFB5 attached to FBG7.

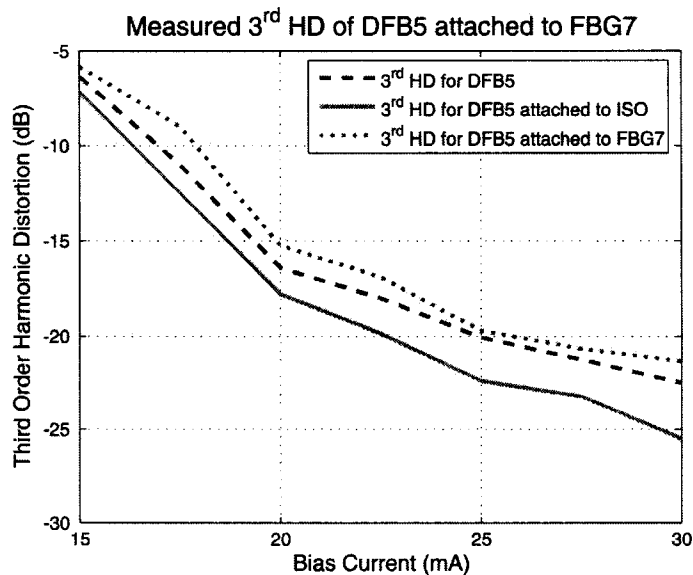


Figure B.24: Measured third order harmonic distortion normalized to the fundamental frequency of DFB5 attached to FBG7.

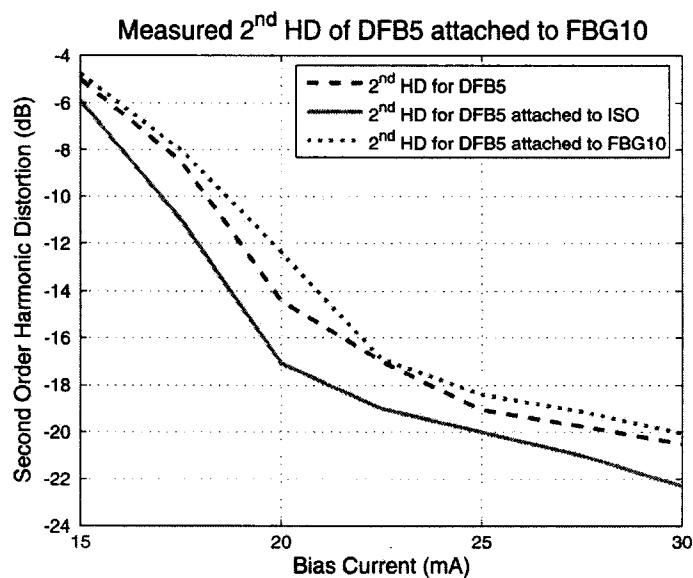


Figure B.25: Measured second order harmonic distortion normalized to the fundamental frequency of DFB5 attached to FBG10.

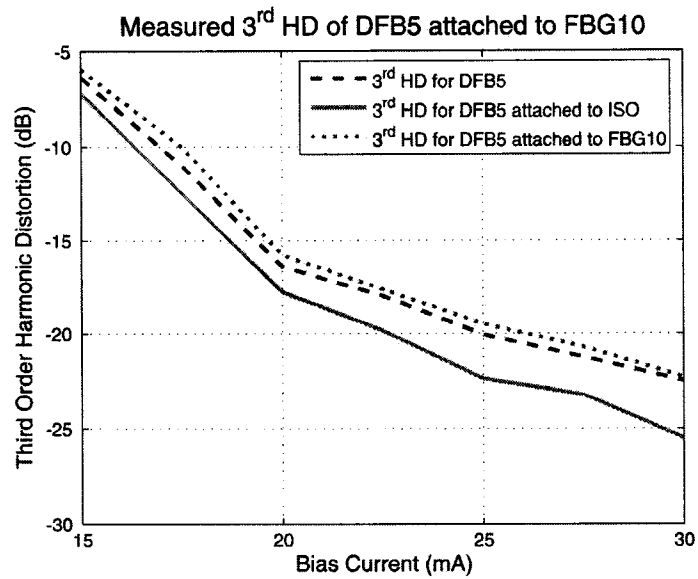


Figure B.26: Measured third order harmonic distortion normalized to the fundamental frequency of DFB5 attached to FBG10.

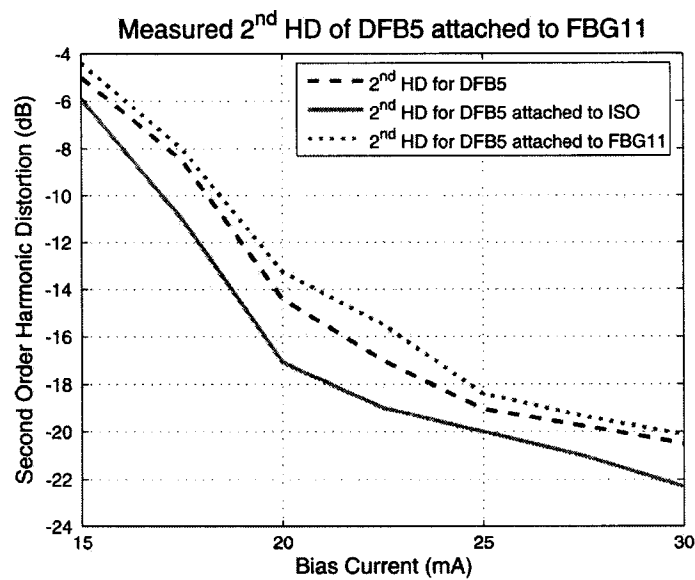


Figure B.27: Measured second order harmonic distortion normalized to the fundamental frequency of DFB5 attached to FBG11.

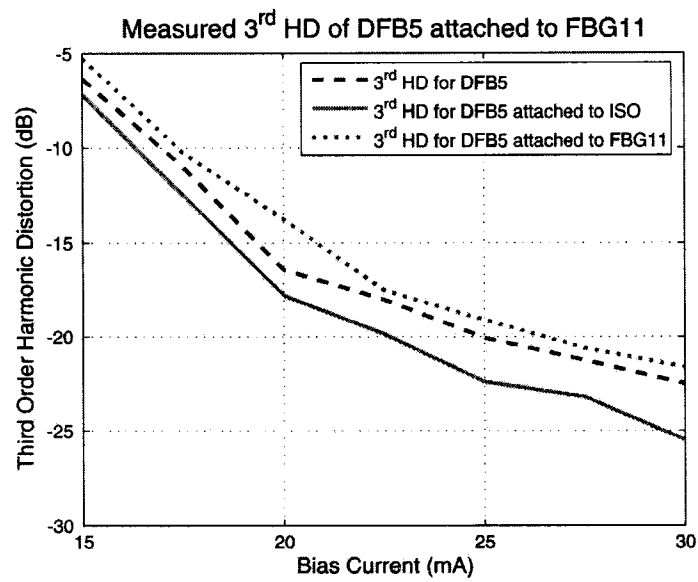


Figure B.28: Measured third order harmonic distortion normalized to the fundamental frequency of DFB5 attached to FBG11.

Bibliography

- [1] David R. Goff, *Fiber Optic Video Transmission*. Elsevier Science (USA), 2003.
- [2] B. Buxton, and R. Vahldieck, "Noise and intermodulation distortion reduction in an optical feed-forward transmitter," *Microwave Symposium Digest, IEEE MTT-S International*, vol. 2, pp. 1105 – 1108, 23-27 May 1994.
- [3] F. Willens, and W. Muys, and J. Leong, "Requirements for components used in a 1550 nm analogue CATV system for the local loop: A view from RACE 2062 "COMFORT"," *Communications, 1993. ICC 93. Geneva. Technical Program, Conference Record, IEEE International Conference on*, vol. 3, pp. 1933 – 1936, 23-26 May 1993.
- [4] T. E. Darcie, and G. E. Bodeep, "Lightwave subcarrier CATV transmission systems," *Microwave Theory and Techniques, IEEE Transactions on*, vol. 38, pp. 524 – 533, May 1990.
- [5] J. van der Ziel, and R. Mikulyak, "Single-mode operation of 1.3 μm InGaAsP/InP buried crescent lasers using a short external optical cavity," *IEEE JQE*, vol. 20, no. 3, pp. 223 – 229, 1984.
- [6] L. Coldren, and T. Koch, "External-cavity laser design," *Journal of Lightwave Technology*, vol. LT-2, pp. 1045 – 1051, December 1984.
- [7] R. S. Vodhanel, and J. S. Ko, "Reflection-induced frequency shifts in single-mode laser diodes coupled to optical fibers," *Electron. Lett.*, vol. 20, pp. 973 – 974, 8th Nov. 1984.
- [8] R. Wyatt, "Spectral linewidth of external cavity semiconductor lasers with strong frequency-selective feedback," *Electron. Lett.*, vol. 21, pp. 658 – 659, 18th July 1985.
- [9] R. S. Vodhanel, and J. S. Ko, "Oscillation frequency tuning characteristics of fiber-extended-cavity distributed-feedback lasers," *Appl. Phys. Lett.*, vol. 50, pp. 380 – 382, 16th Feb. 1987.
- [10] K. Petermann, *Laser diode modulation and noise*. Kluwer Academic Publishers, 1991.
- [11] R. Tkach, and Chraplyvy, "Regimes of feedback effects in 1.5- μm distributed feedback lasers," *Journal of Lightwave Technology*, vol. 4, pp. 1655 – 1661, Nov 1986.
- [12] Y. Hong, S. Bandyopadhyay, S. Sivaprakasam, and et al, "Noise characteristics of a single-mode laser diode subject to strong optical feedback," *Journal of Lightwave Technology*, vol. 20, pp. 1847– 1850, OCTOBER 2002.
- [13] Gerd Keiser, *Optical fiber Communications*. McGraw-Hill, 2000.
- [14] P. S. Andre et al, "Extraction of Laser Rate Equation Parameters," *SPIE proc.*, vol. 3572, pp. 141–146, August 1999.
- [15] D. E. Dodds, and M. J. Sieben, "Fabry-Perot Laser Diode Modeling," *IEEE Phot. Tech. Lett.*, vol. 7, pp. 254–256, March 1995.
- [16] R. Sabella, "Performance Analysis of Wireless Broadband Systems Employing Optical Fiber Links," *IEEE Trans. Comm.*, vol. 47, pp. 715–721, May 1999.

- [17] M. Ahmed, M. Yamada, and M. Saito, "Numerical Modeling of Intensity and Phase Noise in Semiconductor Lasers," *IEEE JQE*, vol. 37, pp. 1600–1610, Dec. 2001.
- [18] P. V. M. et al, "Rate-Equation-Based Laser Model with a Single Solution Regime," *JLT*, vol. 15, pp. 717–730, April 1997.
- [19] S. Ghoniemy, *RF/Fiber Optical Interface for Microcellular Wireless Transceivers*. PhD thesis, Department of Systems and Computer Engineering, Carleton University Ottawa, Ontario, Canada, 2003.
- [20] S. Ghoniemy, L. MacEachern, and S. Mahmoud, "Comprehensive Modeling of Semiconductor Lasers Including the Effect of Gain Saturation," *IPR'02*, July 2002.
- [21] S. Ghoniemy, L. MacEachern, and S. Mahmoud, "Enhanced Large Signal Laser Modeling Including Thermal Effects for Analog Communications," *IEEE LFNM'02*, June 2002.
- [22] S. Ghoniemy, L. MacEachern, and S. Mahmoud, "Robust Semiconductor Laser Modeling for Analog Optical Link Simulations," *IEEE NUSOD-02*, 2002.
- [23] S. Ghoniemy, L. MacEachern, and S. Mahmoud, "Extended Robust Semiconductor Laser Modeling for Analog Optical Link Simulations," *IEEE JSTQE*, vol. 9, June 2003.
- [24] Koji Kikushima, Osamu Hirota, Masaaki shindo, and et al, "Properties of Harmonic Distortion of Laser Diodes with Reflected Waves," *Journal of Optical Communications*, vol. 3, no. 4, pp. 129–132, 1982.
- [25] Andreas Czyliwik, "Nonlinear System Modeling of semiconductor Laser Based on Volterra Series," *Journal of Optical Communications*, vol. 7, no. 3, pp. 104–114, 1986.
- [26] Jochen Helms, "Intermodulation and harmonic distortions of laser diodes with optical feedback," *Journal of Lightwave Technology*, vol. 9, pp. 1567 – 1575, Nov 1991.
- [27] J. S. Cohen, R. R. Drenten, and B. H. Verbeeck, "The effect of optical feedback on the relaxation oscillation in semiconductor lasers," *IEEE Journal of Quantum Electronics*, vol. 24, pp. 1989 – 1995, Oct 1988.
- [28] G. Agrawal, "Line narrowing in a single-mode injection laser due to external optical feedback," *IEEE Journal of Quantum Electronics*, vol. 20, pp. 468 – 471, May 1984.
- [29] G. P. Agrawal, N. A. Olsson, and N. K. Dutta, "Effect of fiber-far-end reflections on intensity and phase noise in InGaAsP semiconductor lasers," *Applied Physics Letters*, vol. 45, pp. 597–599, September 1984.
- [30] N. Schunk, and K. Petermann, "Measured feedback-induced intensity noise for 1.3 μm DFB laser diodes," *Electronics Letters*, vol. 25, pp. 63 – 64, Jan 1989.
- [31] N. Schunk, and K. Petermann, "Numerical analysis of the feedback regimes for a single-mode semiconductor laser with external feedback," *IEEE Journal of Quantum Electronics*, vol. 24, pp. 1242 – 1247, July 1988.
- [32] R. Lang, and K. Kobayashi, "External optical feedback effects on semiconductor injection laser properties," *IEEE Journal of Quantum Electronics*, vol. 16, pp. 347 – 355, Mar 1980.
- [33] O. Hirota, and Y. Suematsu, "Quantum intensity noise of directly modulated laser diode influenced by reflected waves," *Institute of Electronics and Communication Engineers of Japan*, vol. E65, pp. 94–101, Feb 1982.
- [34] K. Peterman, and G. Arnold, "Noise and Distortion Characteristics of Semiconductor Lasers in Optical Fiber Communication Systems," *IEEE Transactions on Microwave Theory and Techniques*, vol. 82, pp. 389 – 401, Apr 1982.

- [35] K. Petermann , “Optical feedback phenomena in semiconductor lasers,” *14th IEEE International Semiconductor Laser Conference*, pp. 8 – 11, Sept 1994.
- [36] F. Favre, “Theoretical analysis of external optical feedback on DFB semiconductor lasers,” *IEEE Journal of Quantum Electronics*, vol. 23, pp. 81 – 88, Jan 1987.
- [37] W. I. Way, and M. M. Choy , “Optical feedback on linearity performance of 1.3- μ m DFB and multimode lasers under microwave intensity modulation,” *Journal of Lightwave technology*, vol. 6, pp. 100–108, Jan 1988.
- [38] J. Helms, and K. Petermann, “A simple analytic expression for the stable operation range of laser diodes with optical feedback,” *IEEE Journal of Quantum Electronics*, vol. 26, pp. 833 – 836, May 1990.
- [39] K. Petermann , “External optical feedback phenomena in semiconductor lasers,” *IEEE Journal of Selected Topics in Quantum Electronics*, vol. 1, pp. 480 – 489, June 1995.
- [40] Pan Ming-Wei, Shi Bei-Pei, and R. Gray George, “Semiconductor laser dynamics subject to strong optical feedback,” *Optics Letters*, vol. 22, pp. 166–168, February 1997.
- [41] R. J. Jones, P. S. Spencer, J. Lawrence, and D. M. Kane, “Influence of external cavity length on the coherence collapse regime in laser diodes subject to optical feedback,” *IEE Proceedings-Optoelectronics*, vol. 148, pp. 7 – 12, Feb 2001.
- [42] Ju Rui, S. Paul, S. Spencer, and K. Alan Shore, “The relative intensity noise of a semiconductor laser subject to strong coherent optical feedback ,” *J. Opt. B: Quantum Semiclass. Opt.*, vol. 6, p. S775S779, Aug 2004.
- [43] W. Bludau, and R. Rossberg, “Characterization of laser-to-fiber coupling techniques by their optical feedback,” *Appl. Opt.*, vol. 21, pp. 1933–1939, 1st June 1982.
- [44] R. S. Vodhanel, and J. S. Ko, “Reflection induced frequency shifts in single-mode laser diodes coupled to optical fibers,” *Electron. Lett.*, vol. 20, pp. 973–974, 8th Nov. 1984.
- [45] P. Spano, S. Piazzola, and M. Tamburrini, “Theory of noise in semiconductor lasers in the presence of optical feedback,” *IEEE J. Quant. Electron.*, vol. QE-20, pp. 350–357, Apr. 1984.
- [46] N. Schunk, and K. Petermann, “Minimum bit rate of DPSK transmission for semiconductor laser with a long external cavity and strong linewidth reduction,” *Journal of Lightwave Technology*, vol. 5, pp. 1309–1314, Sep 1987.
- [47] John Rogers, and Calvin Plett, *Radio Frequency Integrated Circuit Design*. Artech House, Incorporated, 2003.
- [48] B. Thedrez, O. Gauthier-Lafaye, F. Grillot, and et al, “1.3 μ m tapered DFB lasers for isolator-free 2.5 Gbits all-optical networks,” *Optical Fiber Communication Conference and Exhibit 2001*, vol. 3, pp. WC4–1– WC4–3, 2001.
- [49] R. T. Sahara, R. A. Salvatore, A. Hohl-Abichedid, and Lu Hanh, “Isolator-free transmission at 2.5 Gbits/s over 100 km of single-mode fiber by a 1.55- μ m, AlGaInAs strained-multi-quantum-well, directly modulated distributed-feedback laser diode,” *IEEE Journal of Quantum Electronics*, vol. 38, pp. 620–625, June 2002.
- [50] W. S. Ring, I. S. Smith, A. J. Taylor, and et al , “Unisolated 2.5 Gbit/s uncooled gain-coupled 1300 nm DFB lasers for low cost applications,” *Electronic Components and Technology Conference 1998*, pp. 192–197, 1998.
- [51] K. Terada, S. Sasaki, K. Tanaka, and et al , “Isolator-free DFB-LD module with TEC control using silicon waferboard,” *Electrical Performance of Electronic Packaging, 1996., IEEE 5th Topical Meeting 28-30 Oct.*, pp. 71–73, 1996.

- [52] M. Choy, W. Yeo, T. Eustis, and et al, "High temperature and isolator-free 1310 nm photonic integrated surface emitter operating at 2.5 Gb/s over 25 km transmission," *Optical Fiber Communication Conference and Exhibit, 2002. OFC 2002 17-22 Mar 2002*, pp. 719 – 721, Mar 2002.
- [53] A. Mokhtar, L. MacEachern, and S. Mahmoud, "Semiconductor Laser Diode Model Implementation Including Optical Back-Rrlection," *Electrical and Computer Engineering, 2006. Canadian Conference on*, pp. 2146 – 2149, May 2006.
- [54] A. Mokhtar, L. MacEachern, and S. Mahmoud, "Isolator-free DFB laser diode operating in feedback regime V," *Proc. SPIE, Active and Passive Optical Components for Communications VI*, vol. 6389, pp. 63891F-1 – 63891F-9, Oct. 2 2006.
- [55] K. O. Hill, and G. Meltz , "Fiber Bragg grating technology fundamentals and overview," *Journal of Lightwave Technology*, vol. 15, pp. 1263 – 1276, Aug 1997.
- [56] T. Erdogan, "Fiber grating spectra," *Journal of Lightwave Technology*, vol. 15, pp. 1277 – 1294, Aug 1997.
- [57] Andreas Othonos, and Kyriacos Kalli, *Fiber Bragg gratings: fundamentals and applications in telecommunications and sensing*. Artech House, 1999.
- [58] B. F. Ventrudo, G. A. Rogers, G. S. Lick, and et al, "Wavelength and intensity stabilisation of 980 nm diode lasers coupled to fibre Bragg gratings," *Electronics Letters*, vol. 30, pp. 2147-2149, December 1994.
- [59] T. Iwai, K. Sato, and K. I. Suto, " Signal Distortion and Noise in AM-SCM Transmission System Employing the Feedforward Linearization MQW-EW External Modulator," *JLT*, vol. 13, pp. 1606 – 1612, Aug. 1995.
- [60] B. Buxton, and R. Vahldieck, "Noise and Intermodulation Distortion Reduction in an optical Feedforward Transmitter," *IEEE MTT-S Digest*, pp. 1105 – 1108, 1994.
- [61] D. Hassin, and R. Vahldieck, "Feedforward Linearization of Analog Modulated Laser Diodes: Theoretical Analysis and Experimental Verification," *IEEE Trans MW Theo. and Tech.*, vol. 41, pp. 2376 – 2382, Dec. 1993.
- [62] L. S. Fock, and R. S. Tucker, "Reduction of Distortion in Analog Modulated Semiconductor Lasers by FeedForward Compensation," *Elect. Lett.*, vol. 27, pp. 669 – 671, Apr. 1991.
- [63] D. Hassin, and R. Vahldieck, "Improved Feedforward Linearization of Laser Diodes - Simulation and Experimental Results," *IEEE MTT-S Digest*, pp. 727 – 730, 1993.
- [64] K. Tsukamoto, S. Fujii, P. Sanjo, S. Komaki, "Fiber-optic Microcellular Communication System using Frequency Modulated LD and Optical Discriminator and its Nonlinear Distortion Suppression," *IEEE PIMRC'97*, no. 3, pp. 984 – 988, 1997.
- [65] J. Tsimbinos, and K. V. Lever, "Nonlinear Compensation using Orthogonal Inverses: Broadband Inputs and Robustness Issues," *TENCON '96*, vol. 2, pp. 816 – 821, 1996.
- [66] J. Tsimbinos, and K. V. Lever, "The Computational Complexity of Nonlinear Compensators Based on the Volterra Inverse," *8th IEEE Sig. Process. Conf.*, pp. 387 – 390, 1997.
- [67] H. Gysel, and M. Ramachandran , "Electrical Predistortion to Compensate for Combined Effect of Laser Chirp and Fiber Dispersion," *Elect. Lett.*, vol. 27, pp. 421 – 423, Feb. 1991.
- [68] B. Wilson, and I. Darwazeh, "Analogue Optical Fiber Communications," *IEE*, 1995. London.
- [69] L. Roselli, and et al , "Predistortion Circuit Design for II and III Order Simultaneous Linearization in Multiservice Telecommunications Apparatuses," *IEEE MTT-S Digest*, pp. 1711 – 1714, 2002.

- [70] Y. Chiu, and et al, "Broadband Electronic Linearizer for Externally Modulated Analog Fiber-Optic Links," *IEEE Phot. Tech. Lett.*, vol. 11, pp. 48 – 50, Jan. 1999.
- [71] X. J. Meng, A. Yacoubian, and J. H. Bechtel, "Electro-optical Predistortion Technique for Linearization of Mach-Zehnder Modulators,"
- [72] G. C. Wilson, "Optimized Predistortion of Over Modulated Mach-Zehnder Modulators with Multi-carrier Input," *IEEE Phot. Tech. Lett.*, vol. 9, pp. 1535 – 1537, Nov. 1997.
- [73] X. N. Fernando, and A. B. Sesay, "Higher Order Adaptive Filter Based Predistortion for Nonlinear Distortion Compensation of Radio over Fiber Links," *IEEE Transactions on Electron Devices*, vol. 1, pp. 367 – 371, 2000.
- [74] M. Faulkner, and M. Johansson, "Adaptive Linearization using Predistortion-Experimental Results," *IEEE Trans. on Veh. Tech.*, vol. 43, pp. 323 – 332, May 1994.
- [75] X. N. Fernando, and A. B. Sesay, "Look-Up Table Based Adaptive Predistortion for Dynamic Range Enhancement in a Radio over Fiber Links," *IEEE Conf. on Comm., Comp. and SP*, pp. 26 – 29, 1999.
- [76] G. Steiner, S. Hunziker, and W. Baechtold, "Reduction of 3rd Order Intermodulation of a Semiconductor Laser by an Adaptive Low-Cost Predistortion Circuit at 1.8 GHz," *IEEE LEOS Meet. RF Phot. for CATV and HFC Sys.*, July 1999.
- [77] X. J. Meng, D. T. K. Tong, T. Chau, and M. C. Wu, "Demonstration of an Analog Fiber-Optic Link Employing a Directly Modulated Semiconductor Laser with External Light Injection," *IEEE Phot. Tech. Lett.*, vol. 10, pp. 1620 – 1622, Nov. 1989.
- [78] D. J. M. Sabido, and et al., "Improving the Dynamic Range of a Coherent AM Analog Optical Link using Cascaded Linearized Modulator," *IEEE Phot. Tech. Lett.*, vol. 7, pp. 813 – 815, July 1995.
- [79] E. D. Bedrosian, and S. O. Rice, "The output properties of volterra system (nonlinear systems with memory) driven by harmonic and gaussian inputs," *Proc. IEEE*, vol. 59, pp. 1688–1707, December 1971.
- [80] J. J. Bussgang, and L. Ehrman, and J. W. Graham, "Analysis of nonlinear systems with multiple inputs," *Proc. IEEE*, vol. 62, pp. 1088–1119, August 1974.
- [81] M. Schetzen, *The Volterra and Wiener Theories of Nonlinear Systems*. New York: John Wiley Sons, 1980.